Title
Structural Integration of Silicon Solar Cells and Lithium-ion Batteries Using Printed Electronics

Author
Kang, Jin Sung

Publication Date
2012

UNIVERSITY OF CALIFORNIA

Los Angeles

Structural Integration of Silicon Solar Cells and Lithium-ion Batteries Using Printed Electronics

A dissertation submitted in partial satisfaction of the
requirements for the degree Doctor of Philosophy
in Mechanical Engineering

by

Jin Sung Kang

2012

ABSTRACT OF THE DISSERTATION

Structural Integration of Silicon Solar Cells and Lithium-ion Batteries Using Printed Electronics

by

Jin Sung Kang
Doctor of Philosophy in Mechanical Engineering
University of California, Los Angeles, 2012
Professor H. Thomas Hahn, Chair

Inkjet printing of electrode using copper nanoparticle ink is presented. Electrode was printed on a flexible glass epoxy composite substrate using drop on demand piezoelectric dispenser and was sintered at 200°C in N_2 gas condition. The printed electrodes were made with various widths and thicknesses. Surface morphology of electrode was analyzed using scanning electron microscope (SEM) and atomic force microscope (AFM). Reliable dimensions for printed electronics were found from this study.

Single-crystalline silicon solar cells were tested under four-point bending to find the feasibility of directly integrating them onto a carbon fiber/epoxy composite laminate. These solar cells were not able to withstand 0.2% strain. On the other hand, thin-film amorphous silicon solar cells were subjected to flexural fatigue loadings. The current density-voltage curves were analyzed at different cycles, and there was no noticeable degradation on its performance up to 100 cycles.

A multifunctional composite laminate which can harvest and store solar energy was fabricated using printed electrodes. The integrated printed circuit board (PCB) was co-cured with a carbon/epoxy composite laminate by the vacuum bag molding process in an autoclave; an amorphous silicon solar cell and a thin-film solid state lithium-ion (Li-ion) battery were adhesively joined and electrically connected to a thin flexible PCB; and then the passive components such as resistors and diodes were electrically connected to the printed circuit board by silver pasting.

Since a thin-film solid state Li-ion battery was not able to withstand tensile strain above 0.4%, thin Li-ion polymer batteries were tested under various mechanical loadings and environmental conditions to find the feasibility of using the polymer batteries for our multifunctional purpose. It was found that the Li-ion polymer batteries were stable under pressure and tensile loading without any noticeable degradation on its charge and discharge performances. Also, the active materials did not decompose at 80°C, and the battery was performing well under low temperature of -27°C. Lastly, the batteries were embedded inside a carbon fiber/epoxy composite laminate to characterize their performance under fatigue loading.

Finally, an intense pulsed light (IPL) was used to sinter printed silver nanoink patterns. X-ray diffraction (XRD) was used to find grain size of printed silver nanoink patterns. From these analyses it was confirmed that IPL is able to adequately sinter silver nanoink patterns for printed electronics without degradation of the substrates in less than 30 ms.

The dissertation of Jin Sung Kang is approved.

Gregory P Carman

Pei-Yu Chiou

Qibing Pei

H Thomas Hahn, Committee Chair

University of California, Los Angeles

2012

To God almighty, the creator of the Heavens and the Earth, and the Savior -
who leads me, and gives me strength.

To my parents, my family, my friends and you -
who make my life meaningful.

TABLE OF CONTENTS

LIST OF FIGURES

LIST OF TABLES

ACKNOWLEGEMENTS

First of all, I would like to thank God for providing me with wonderful opportunities and leading me through my studies. I would like to thank Professor H. Thomas Hahn for his guidance, support and advice. This thesis would not have been possible without the contribution and effort of him. I also appreciate Professor Gregory P. Carman, Professor Pei-Yu Chiou, and Professor Qibing Pei for serving as my committee members and for their professional suggestion to my study. I will never forget the valuable discussion and help from my mentor and partner, Professor Hak Sung Kim and Dr. Jong Eun Ryu. I also want to thank Professor Kosuke Takahashi, Mr. Stephan Prince, Mr. Joseph Riendeau, Dr. Dong-Myung Yoon, Mr. Eli Novin, Ms. Nataly Qian Chen and all of group members and friends. Most of all, I am also forever grateful to my family and my friends for their support.

The present study is based on work supported by the Air Force Office of Scientific Research through a MURI grant FA9550-06-1-0326 to the University of Washington. Appreciation is extended to Dr. B. Les Lee for encouragement in this work. This research was supported partly by the WCU (World Class University) program through the National Research Foundation funded by the Ministry of Education, Science and Technology of Korea (R31-2008-10083-0).

VITA

October 28, 1986	Born, Seoul, Korea
2008	B. S., Mechanical Engineering Department of Mechanical and Aerospace Engineering University of California, Los Angeles (UCLA)
2010	M. S., Mechanical Engineering Department of Mechanical and Aerospace Engineering University of California, Los Angeles (UCLA)
2010	Visiting Student Researcher Optoelectronic Materials Center Korea Institute of Science And Technology (KIST) Seoul, Korea
2008-2012	Teaching Assistant, Teaching Associate, Graduate Student Researcher Department of Mechanical and Aerospace Engineering University of California, Los Angeles (UCLA)

PUBLICATIONS AND PRESENTAIONS

Jin S Kang, Hak S Kim, Jongeun Ryu, H Thomas Hahn, “Sintering of Inkjet Printed Silver Nanoparticles at Room Temperature Using Intense Pulsed Light, ” J. Electronic Materials, vol. 40, number 11, 2011, 2268-2277.

Jin S Kang, Hak S Kim, Jong Ryu, H Thomas Hahn, Seonhee Jang, and Jae W. Joung, “Inkjet Printed Electronics using Copper Nanoparticle Ink,” J. Materials Science: Materials in Electronics, vol. 21, number 11, 2010, 1213-1220.

Hak Sung Kim, Yong-Min Lee, Sanjay R. Dhage, **Jin S Kang**, H. Thomas Hahn, “Nano composite for power laminate,” 17th International Conference on Composite Materials, Edinburgh, United of Kingdom, July, 2009.

Hak S Kim, **Jin S Kang**, J S Park, and H Thomas Hahn, Hyun C. Jung and Jae W. Joung, “Inkjet printed electronic technique for multifunctional composite structure,” Composites Science and Technology, vol. 69, 2009, 1256-1264.

CHAPTER ONE

Introduction

1.1. Background

Multifunctional composite structure is the structure which can not only endure mechanical stresses but perform various functions such as energy harvest, energy storage, sensing, and actuating[1]. The greatest advantage in having multifunctional composite structure is reducing weight by combining various functions. General types of multifunctional structures are structural power materials, autonomous sensing and actuating materials, electromagnetic multifunctional materials and survivable, damage-tolerant materials[2]. Multifunctional composite structure can be applied onto building windows to harvest solar energy during the day, and cars to harvest thermal energy from engine. One of the most promising areas of using multifunctional composite structure is Unmanned Aerial Vehicles (UAVs), and the structural power materials system is the most interesting type because many UAVs are used for surveillance and disaster relief, which require long flight endurance time[3,4].

An important UAV performance metric is flight endurance time, t_E, which depends on the available energy of battery or fuel cell, weights, and aerodynamic parameters [5,6]:

$$t_E = \left(\frac{E_B \eta_B}{\left(W_S + W_B + W_{PR} + W_{PL}\right)^{3/2}} \right) \times \left[\frac{\rho S C_L^3}{2 C_D^2} \right]^{1/2} \eta_P \qquad \text{Eq. 1-1}$$

where E_B is stored energy of battery, η_B is the efficiency of a battery, η_P is motor or propeller efficiency, W_S is structure weight, W_B is battery weight, W_{PR} is propulsion weight, and W_{PL} is payload weight[5,6]. For aerodynamic part of Eq. 1-1, C_L is lift coefficient, C_D is drag coefficient, *S* is wing platform area, and ρ is air density. This equation shows that one can prolong the flight endurance time by improving the battery to have more energy or by decreasing weight of different parts of UAVs. The resulting change in the flight endurance time is given by:

$$\frac{\Delta t_E}{t_E} = \frac{\Delta\left(E_B\eta_B\right)}{E_B\eta_B} - \frac{3}{2}\frac{\left(\Delta W_S + \Delta W_B\right)}{W_{total}} \qquad \text{Eq.1-2}$$

According to Eq. 1-2 [5,6], reducing weight of subsystems of UAVs is 50% more effective than improving battery efficiency and useable energy of battery. The fuel or battery system and structure of UAVs each takes about 20 to 40% of the total weight[6]. Therefore, there is much room for improving flight endurance time by combining structural components with energy harvest and/or storage capabilities. One good example use of a multifunctional material system is Wasp. Using multidisciplinary design optimization and analysis[7], the endurance time of a multifunctional Wasp can be made 25.9% greater than that of an unifunctional Wasp.

Not only the energy storage but also the energy harvest is essential in prolonging the flight endurance time. There are many different types of energies that can be harvested while a UAV is in flight, such as heat[8-10], vibration[11-15], and solar energies[16,17]. Government agencies such as NASA and DARPA are funding UAV projects that are aiming at very high flight altitude of 60000 to 90000 feet and flight time of over one month. Current UAVs that are available as initial prototypes are SoLong by AC Propulsion, Helios by AeroVironment, and Zephyr by Qinetiq; they have flown 48, 24, and 54 hours, respectively[18-20].

In order to effectively integrate solar cells and batteries with structural components, the development of methods of making thin and cost effective conductive paths is very important. In recent years, printed electronics technology has attracted lots of attentions in its applications such as flexible radio frequency identification (RFID) tags[21], wearable electronics[22], organic light emitting diodes, and organic solar cells. Conventionally, mask-based photolithography method is used to make a desired conductive pattern. However, the subsequent processes of photolithography require etching and metal deposition such as solvent lift-off and electroplating process that generate large amount of toxic chemical waste. Therefore, many researchers started to pay more attention on the direct inkjet printing method because it does not require the additional etching and metal deposition processes; it has only one-step printing procedure of making a desired conductive pattern on various substrates. In addition to the simple process, and cost and material reduction, the flexibility of changing patterns and the capability of printing on a large area are the most distinguishable advantages of printing method over the photolithography.

1.2. Statement of Purpose

The main objective of the research is to develop multifunctional composite which can harvest and store energy while being used as a structural component of an UAV. There are many sources of energy such as heat, vibration, and solar energy. For this study, solar cells will be used to harvest energy for the system and lithium-ion batteries will be used to store the harvested energy. Following topics were studied to manufacture and characterize multifunctional structures with energy harvest and storage capability:

(1) Develop printed electronics techniques to integrate thin-film solar cells and batteries
(2) Characterize solar cells and batteries for multifunctional performance
(3) Develop structural integration methods for thin-film solar cells and batteries
(4) Develop methods to sinter printed electronics without damaging substrates

1.3. References

[1] H.S. Kim, J.S. Kang, J.S. Park, H.T. Hahn, H.C. Jung, and J.W. Joung, “Inkjet printed electronics for multifunctional composite structure,” Composites Science and Technology, vol. 69, 2009, pp. 1256–1264.

[2] Christodoulou L, Venables J. Multifunctional material systems: The first generation. J Miner Met Mater Soc 2003;55; 39-45.

[3] Rodriguez P, Geckle W, Barton J, Samsundar J, Gao T, Brown M, Martin S. An emergency response UAV surveillance system. AMIA Annu Sym Proc 2006; 1078.

[4] Loyall J, Ye J, Neema S, Mahadevan N. Model-based design of end-to-end quality of service in a multi-UAV surveillance and target tracking application. 2nd RTAS Workshop on Model-Driven Embedded Syst 2004.

[5] J.P. Thomas and M.A. Qidwai, “The design and application of multifunctional structure-battery materials systems,” JOM Journal of the Minerals, Metals and Materials Society, vol. 57, 2005, pp. 18–24.

[6] J.P. Thomas, M.A. Qidwai, P. Matic, R.K. Everett, A.S. Gozdz, M.T. Keennon, and J. Grasmeyer, “Multifunctional structure-plus-power concepts,” AIAA Paper, vol. 1239, 2002.

[7] J.P. Thomas, M.T. Keennon, A. DuPasquier, M.A. Qidwai, P. Matic, and N.R.L.W.D.M.M. BRANCH, “Multifunctional structure-battery materials for enhanced performance in small unmanned air vehicles,” 2003.

[8] M. Taya, Design of active composites, DTIC Document, 2009.

[9] O. Namli and M. Taya, “Design of Piezo-SMA Composite for Thermal Energy Harvester Under Fluctuating Temperature,” Journal of Applied Mechanics, vol. 1, 2010, p. 74.

[10] O.C. Namli, J.K. Lee, and M. Taya, “Modeling of piezo-SMA composites for thermal energy harvester,” Proceedings of SPIE, 2007, p. 65261L.

[11] Anton S R and Sodano H A 2007 A review of power harvesting using piezoelectric materials (2003-2006) Smart Mater. Struct. **16** R1-21.

[12] Cook-Chennault K A, Thambi N and Sastry A M 2008 Powering MEMS portable devices-a review of non-regenerative and regenerative power supply systems with special emphasis on piezoelectric energy harvesting systems Smart Mater. Struct. **17** 043001

[13] Erturk A and Inman D J 2008 A distributed parameter electromechanical model for cantilevered piezoelectric energy harvesters J. Vib. Acoust. **130** 041002

[14] Elvin N G and Elvin A A 2009 A general equivalent circuit model for piezoelectric generators J. Intell. Mater. Syst. Struct. **20** 3-9.

[15] Kong N, Ha D S, Erturk A and Inman D J 2009 Resistive impedance matching circuit for piezoelectric energy harvesting J. Intell. Mater. Syst. Struct.

[16] Maung J K, Hahn H T and Ju Y S 2010 Multifunctional integration of thin-film silicon solar cells on carbon-fiber-reinforced epoxy composites Sol. Energy **84** 450-8

[17] Sugar JG, Scaffaro R, Guo Z, Maung JK, Ju YS, Hahn HT. Photovoltaic Performance of Amorphous Silicon Flexible Solar Modules under Mechanical Loading. Proc 6th International Workshop on Structural Health Monitoring 2007.

[18] A. Rapinett, “Zephyr: A High Altitude Long Endurance Unmanned Air Vehicle,” University of Surrey, 2009.

[19] L.P. Dube, W.A. McElroy, and D.W. Pepper, “Use of COMSOL In Aerodynamic Optimization of the UNLV Solar-Powered Unmanned Aerial Vehicle.”

[20] E. Bennett, “NASA's Helios prototype-soaring to a new record.,” SAMPE journal, vol. 38, 2002, pp. 41–47.

[21] S.K. Volkman, Y. Pei, D. Redinger, S. Yin, and V. Subramanian, “Ink-jetted silver/copper conductors for printed RFID applications,” Materials Research Society Symposium Proceedings, 2004, pp. 151–156.

[22] S.M. Bidoki, D. McGorman, D.M. Lewis, M. Clark, G. Horler, and R.E. Miles, “Inkjet printing of conductive patterns on textile fabrics,” AATCC review, vol. 5, 2005, p. 11.

CHAPTER TWO

Inkjet Printed Electronics Using Copper Nanoparticle Ink

2.1. Introduction

To take advantage of inkjet printing, the development of a conductive nanoink has become the most important issue. There are two general approaches in making a conductive ink[1]. The first method is to use solutions of metallic organic precursors, which can be reduced at a low temperature. The second method, which is widely used in inkjet printing technology, is to use suspended metallic nanoparticles because they have low melting point than their bulk forms do[2].

Initially, suspension of gold and silver nanoparticles drew attention for a conductive inks because of their high conductivity and thermal stability. Bieri et al. developed a conductive ink by suspending gold nanoparticles in toluene, but it had a high electrical resistivity of 140 nΩm, six times that of bulk gold, and it had the problem of volatile organic compounds emission in industrial applications[3]. In the work of Lee et al., a conductive ink using silver nanoparticles was developed by dissociating silver nitrate in hydrocarbon using butylamine[4]. However, both gold and silver are significantly more expensive than copper. Therefore, a conductive ink using copper nanoparticles drew more attention in recent years.

Several methods to fabricate a conductive ink using copper nanoparticles were developed such as thermal decomposition, nonionic micro emulsions, ultraviolet irradiation, and reduction of copper salts[5,6]. Yet, these processes were not economically efficient because of low throughput of less than 6.35 g of copper per 1 L of solution (0.1 M). To resolve this problem, Lee et al.[7] introduced a chemically controlled process for copper nanoparticles; this novel process has a high throughput of 0.2 M. In this study, we used the chemically controlled process to prepare the copper nanoink.

In addition to the high throughput processing, the characterization of reliability and property of the printed pattern is an essential step to the successful application of copper nanoink. As the nanoparticles in the ink are mixed with polymer binders and solvents, there are inevitable free spaces between the nanoparticles after the nanoink is dried. Moreover, the sintering process can induce cracks in the printed pattern because of the volume decrease by necking and fusion[6]. Therefore, it is essential to minimize those adverse effects in order to improve the reliability and quality of the printed electronics.

In this study, we investigated the sintering phenomena of the copper nanoparticles and the effect of printed electrode's thickness on the quality and reliability of the conductive patterns printed on a glass fiber/epoxy laminate. The surfaces of the electrodes were analyzed with SEM, profilometer, and AFM. X-ray tomography was used to investigate the cracks inside of the printed patterns.

2.2. Experimental Details

2.2.1. Specimen Preparation

The conductive copper nanoink for this study was prepared by Inkjet Business Group in Samsung Electro-Mechanics. To prepare the nanoink, copper nanoparticles of average diameter of 5 nm were coated with an organic capping molecule, poly(N-vinylpyrrolidone) (PVP), and then dispersed in ethylene glycol at 40 % by weight. The organic capping molecules were used to help disperse and prevent aggregation of the copper nanoparticles at room temperature.

The principle of a drop-on-demand (DOD) piezoelectric inkjet nozzle is shown in Fig. 2.1a. In the nozzle, a voltage-controlled piezoelectric actuator presses the orifice membrane and controls the droplet volume to 40 pL. Figure 2.1b shows an SEM image of an inkjet nozzle. The inkjet printer head (Fig. 2.1c) consisting of 512 nozzles was manufactured by Samsung Electro-Mechanics. The inkjet printer head is mounted on a computer–controlled three-axis gantry system with the movement accuracy of ±1 um, Fig. 2.2.

Copper nanoink was printed by the gantry system at a resolution of 800 dpi (dots per inch) on a woven glass fabric/BT (bismaleimide triazine) composite laminate, BT core, 100 µm thick. A designed circuit pattern was printed 5, 10, and 20 times to vary the thickness of the electrode. Figure 2.3 shows the printed electrode pattern where the two circular pads at the ends are used for measurement. BT core was kept at 85 ℃ to help solvent in the ink to be dried more quickly during the printing process.

The printed electrodes could be thermally sintered at a low temperature of 200℃. The nanoparticles can be sintered at the low temperature because they have a higher proportion of surface atoms than macro particles do, according to Schmidt et al.[8] The surface atoms are less constrained in their thermal motion because they have fewer atoms in the neighbor than the inside atoms do. Therefore, as the proportion of the surface atoms to the inside atoms increases, the sintering temperature decreases. Also, Kang et al.[9] extended the explanation for low sintering temperature; for copper nanoparticles, a mechanical energy required to cause a shear deformation is lower than for its bulk form. Optical microscope images of fully sintered printed electrodes on a BT core are shown in Figure 2.4.

2.2.2. Characterization

An optical microscope (Olympus BX 41, Olympus, Japan) was used to analyze the sintered printed electrodes. The surface profile of each electrode was measured using a profilometer (Dektak 8 Surface Profiler, Veeco, USA). An AFM (Dimension 3100, Veeco, USA) was used for the nanoscale surface characterization. A SEM (JSM-6700F, JEOL, Japan) was used to analyze surface cracks and the surface morphology of sintered copper nanoparticles. An X-ray micro-tomography system (SkyScan 1172, SkyScan, Belgium) was used for three-dimensional microscale internal characterization. A four-point probes method was used to measure the resistance of each printed electrode using a digital multimeter (Keithley 2100, Keithley Instruments, USA). In this mehod, a first pair of test leads sends test current, and a second pair of test leads measures the voltage drop across a printed electrode. This method minimizes the effects of lead resistance because the high input impedance nature of voltmeter eliminates the current though the second pair of test leads. The resulting electrical resistivity, ρ, was calculated using the following equation:

$$\rho = \frac{Rwt}{L} \qquad \text{Eq. 2-1}$$

where R is the electrical resistance, w is the width, t is the thickness, and L is the length of an printed electrode.

2.3. Results and Discussion

The melting temperature of metallic nanoparticles can be predicted by the following equation[10] :

$$T_m = T_0 \times \left(1 - \frac{2}{d_s L r} \left[\gamma_s - \gamma_l \left(\frac{d_s}{d_l} \right)^{2/3} \right] \right) \qquad \text{Eq. 2-2}$$

where *d* is the density, γ is the surface tension, T_0 is the melting temperature of bulk metal, L is the latent heat of fusion, and r is the radius of the nanoparticle. The subscripts s and l denote solid and liquid, respectively. The material constants of copper are shown in Table 2.1; the liquid state properties are taken from copper at the temperature of 1500 K. Eq. 2-2 predicts that the melting temperature of copper is significantly depressed much lower than 600°C when the particle radius is smaller than 10 nm. Also, because sintering temperature is defined as the temperature at which the grains of solid form from particles connected at their surfaces, it is 20 % lower than the melting temperature for the bulk, according to Mackenzie and Shuttleworth[11]. In this study, copper nanoparticles were fully sintered at 200°C in an inert atmosphere of nitrogen gas to prevent the oxidation.

Figure 2.5 shows the sintering result of the copper nanoparticle ink as a function of sintering time for the 5-times printed electrode. It was found that the copper nanoparticles could be sintered fully in 20 minutes. Figure 2.6 shows high-resolution SEM images of an inkjet printed electrode before and after 20-minute thermal sintering; dispersed copper nanoparticles are agglomerated and sintered after thermal sintering.

Profilometer results are shown in Table 2.2. Average thicknesses of 5-, 10-, and 20-times printed electrodes are 1731 nm, 3690 nm, and 11954 nm, respectively. Surface profiles of printed electrodes using a profilometer are shown in Figure 2.7. A profile roughness was calculated by taking an average of the vertical deviations of a top surface from its ideal form, a flat surface. The roughnesses are 1100 nm, 500 nm, and 3000 nm for 5-, 10-, and 20-times printed electrodes, respectively. Therefore, 10-times printed electrodes have a more uniform surface profile than the others.

Based on the thicknesses and widths measured by the profilometer, average resistivities of 5-, 10-, and 20-times printed electrodes were calculated to be 61.3, 36.7, and 98.9 nΩm, respectively. Resistivities of each printed electrodes are presented on Table 2.2 and Figure 2.8.

At 1000X magnification of sintered electrodes (Figure 2.9), many small cracks are found on the surface of the 5-times printed electrode while large cracks are found on the 20-times printed electrode. However, the 10-times printed electrode does not show any discernible cracks (Figure 2.9b). The mechanisms of these small surface cracks can be explained as follows. Smaller particles melts faster, and they randomly merge with particles on their left or right. The lengths of sintered copper particles were smaller than lengths of unsintered copper particles[12]. The gaps that were created from merging of particles serve as initial crack tips. Schematic of this sintering process with crack propagation is shown in Figure 2.10. Moreover, according to Scherer and Garino[13], when nanoparticles are sintered on a rigid substrate, shrinkage is inhibited on the plane of the substrate; therefore, tensile stress arises through the thickness of the layer, which may promote more the small crack generation during the sintering process.

As a proof of cracks on the top surfaces, three-dimensional surface profiles of sintered electrodes were taken on 1 μm by 1 μm square using AFM. In Figure 2.11, lines on AFM images of printed electrodes indicate the cracks on their top surfaces. All 5-, 10-, and 20-times printed electrodes have these cracks. As Figure 2.9b shows, 10-times printed electrode's cracks were not observable because 10-times printed electrode had enough number of printed layers to cover the cracks being generated during sintering process (Figure 2.12b). Unlike 10-times printed electrode, 5-times printed electrode does not have enough layers to cover cracks; therefore, cracks are shown at 1000X magnification (Figure 2.9).

Using 50000X magnification, agglomerations of copper nanoparticles are observed for 5-, 10-, and 20-times printed electrodes, shown in Figure 2.13a, 2.13b, and 2.13c, respectively. Voids in 5-times printed electrodes are bigger than 10-times printed electrodes. Similarly, voids in 10-times printed electrodes were bigger than voids in 20-times printed electrode, showing that copper nanoparticles were most densely sintered for 20-times printed electrodes.

Although the 20-times printed electrode is most densely agglomerated, and has more number of layers than the 10-times printed one, severe microscopic cracks are observed at low SEM magnification (Figure 2.9) and X-ray tomography (Figure 2.14). Small cracks on the 5-times printed electrode are not observed on the X-ray tomography because of its low resolution. Figure 2.9c shows that small cracks in the 20-times printed electrode have grown into larger cracks. The existence of these large cracks can be explained by the following two reasons. First, according to Scherer and Garino[13], less porous film experience more stress from a rigid substrate. Since the 20-times printed electrode is the least porous, it experienced highest tensile biaxial stress from its rigid substrate, which causes crack propagation.

Secondly, according to Bordia and Jagota[14], a crack grows when the thickness of the film is greater than the critical thickness. The governing equation for crack growth in a sintered thin-film can be expressed as follows:

$$\frac{1}{k} > a\left(\frac{\pi}{1-v^2}\right) \qquad \text{Eq. 2-3}$$

where k is a friction parameter, a is a half of crack length, and v is Poisson's ratio, 0.355 for Cu. As shown in Figure 2.9a, the lengths of cracks on top surfaces are at least 3 μm. Using these parameters, the right side of Eq. 2-3 is calculated to be 5.4 μm. This means if $1/k$ is larger than 5.4 μm, a crack will grow. In other words, the friction parameter, k, should not be smaller than 0.185 μm^{-1}.

The friction parameter is depended on the film thickness. According to Jagota and Hui[15], the friction parameter can be expressed as below,

$$k = \frac{1}{t}\sqrt{\frac{3(1-v)}{2}} \qquad \text{Eq. 2-4}$$

where t is the film thickness. Using the friction parameter value obtained above, it can be determined that if the thickness of the film is greater than 5.3 μm, the friction parameter will be less than 0.185 μm^{-1}, and the crack will grow. Since the 20-times printed electrode has the film thickness greater than 5.3 μm, the cracks on the 20-times printed electrode propagated.

Lastly, the 10-times printed electrode has the best quality, the low resistivity of 36.7 nΩ·m. This resistivity is higher than that of bulk copper, 17.2 nΩm due to the porous structure of a sintered copper electrode. However, this resistivity of the printed electrode is suitable to be used as a conductive path for a solar cell and battery because the resistivity of our printed electrodes is lower than 87 nΩm, which is the adequate resistivity value for a conductive circuit[16].

2.4. Conclusions

Inkjet printed electrodes with various dimensions were characterized. Specific results are

(1) To reduce the amount of cracks, range of particle size should be reduced as much as possible because the cracks are initially formed by having different particle sizes.

(2) To have good quality of printed electrode, the number of printings should not be too large so that the final thickness is kept below the critical thickness.

(3) The resistivity of the optimal printed electrode using the copper nanoparticles was 36.7 nΩ·m, which is suitable for industrial applications such as RFID.

2.5. References

[1] D. Kim and J. Moon, “Highly Conductive Ink Jet Printed Films of Nanosilver Particles for Printable Electronics,” Electrochemical and Solid-State Letters, vol. 8, Nov. 2005, pp. J30-J33.

[2] G.L. Allen, R.A. Bayles, W.W. Gile, and W.A. Jesser, “Small particle melting of pure metals,” Thin solid films, vol. 144, 1986, pp. 297–308.

[3] N.R. Bieri, J. Chung, S.E. Haferl, D. Poulikakos, and C.P. Grigoropoulos, “Microstructuring by printing and laser curing of nanoparticle solutions,” Applied Physics Letters, vol. 82, 2003, p. 3529.

[4] K.J. Lee, B.H. Jun, T.H. Kim, and J. Joung, “Direct synthesis and inkjetting of silver nanocrystals toward printed electronics,” Nanotechnology, vol. 17, 2006, pp. 2424-2428.

[5] M. Aslam, G. Gopakumar, T.L. Shoba, I.S. Mulla, K. Vijayamohanan, S.K. Kulkarni, J. Urban, and W. Vogel, “Formation of Cu and Cu2O nanoparticles by variation of the surface

ligand: Preparation, structure, and insulating-to-metallic transition," Journal of colloid and interface science, vol. 255, 2002, pp. 79–90.

[6] L. Qi, J. Ma, and J. Shen, "Synthesis of copper nanoparticles in nonionic water-in-oil microemulsions," Journal of colloid and interface science, vol. 186, 1997, pp. 498–500.

[7] Y. Lee, J. Choi, K.J. Lee, N.E. Stott, and D. Kim, "Large-scale synthesis of copper nanoparticles by chemically controlled reduction for applications of inkjet-printed electronics," Nanotechnology, vol. 19, 2008, p. 415604.

[8] M. Schmidt, R. Kusche, B. Von Issendorff, and H. Haberland, "Irregular variations in the melting point of size-selected atomic clusters," Nature, vol. 393, 1998, pp. 238–240.

[9] J.W. Kang and H.J. Hwang, "Molecular dynamics simulations of ultra-thin Cu nanowires," Computational materials science, vol. 27, 2003, pp. 305–312.

[10] P. Buffat and J. Borel, "Size effect on the melting temperature of gold particles," Physical Review A, vol. 13, Jun. 1976, pp. 2287-2298.

[11] J.K. Mackenzie and R. Shuttleworth, "A Phenomenological Theory of Sintering," Proceedings of the Physical Society. Section B, vol. 62, 1949, pp. 833-852.

[12] H. Zhu, "Sintering processes of two nanoparticles: A study by molecular dynamics simulations," Philosophical Magazine Letters, vol. 73, 1996, pp. 27-33.

[13] G.W. Scherer and T. Garino, "Viscous Sintering on a Rigid Substrate," Journal of the American Ceramic Society, vol. 68, 1985, pp. 216-220.

[14] R.K. Bordia and A. Jagota, "Crack Growth and Damage in Constrained Sintering Films," Journal of the American Ceramic Society, vol. 76, 1993, pp. 2475-2485.

[15] A. Jagota and C.Y. Hui, "Mechanics of sintering thin films–I. Formulation and analytical results," Mechanics of Materials, vol. 9, 1990, pp. 107–119.

[16] V. Subramanian, P. Chang, D. Huang, J. Lee, S. Molesa, D. Redinger, S. Volkman, VLSI Design held jointly with 5th International Conference on Embedded Systems and Design., 19th International Conference on, 6 (2006)

Table 2.1: Physical constants of copper

	Solid	Liquid
Density, ρ (kg·m^{-3})	8960	7998
Surface tension, γ (J·m^{-2})	1.8	1.1
Latent heat of fusion, L (J·kg^{-1})	2.05×10^5	-

Table 2.2: Dimensions and Electrical Resistances of Printed Electrodes.

Number of Printing	Resistance (Ω)	Width (μm)	Average Thickness (nm)	Length (cm)	Resistivity (nΩ·m)
5	11.2882	409.68	1979	10	91.497
	6.4898	471.73	1480	10	45.306
	4.7632	569.04	1736	10	47.051
10	2.6414	368.01	3736	10	36.316
	2.4143	398.93	3773	10	36.339
	1.9327	564.38	3255	10	35.505
	1.5616	621.08	3996	10	38.757
20	1.4849	410.27	13295	10	80.993
	1.4231	494.33	10926	10	76.861
	1.3917	560.37	11053	10	86.199
	1.8719	645.10	12543	10	151.467

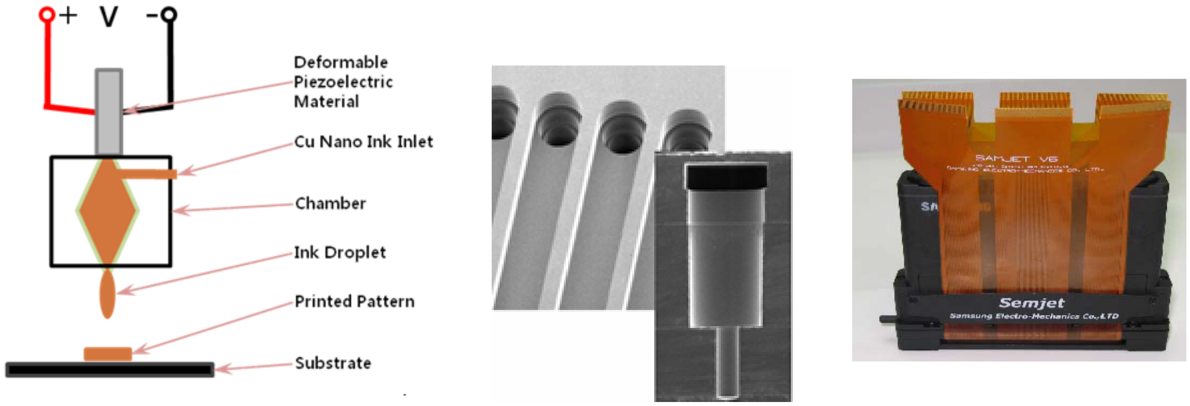

(a) (b) (c)

Figure 2.1: Drop-on demand piezoelectric ink-jet nozzle: (a) schematic diagram; (b) SEM photograph of the micro ink-jet nozzle; (c) ink-jet printer head

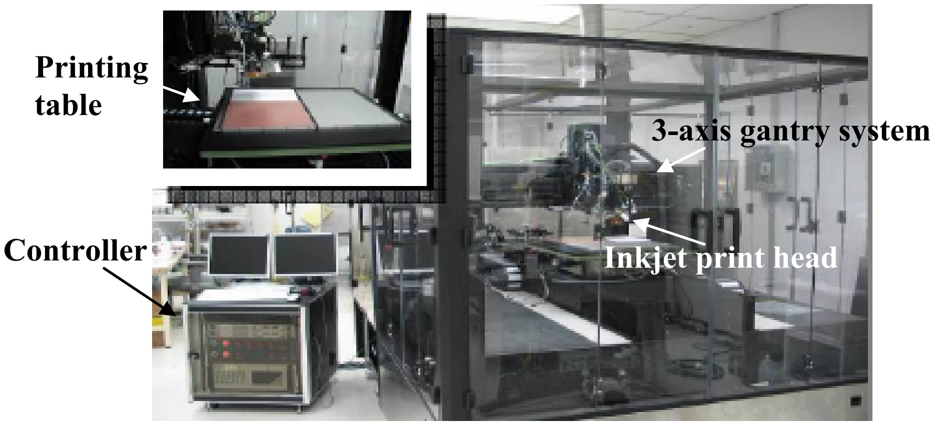

Figure 2.2: The computer-controlled three axis gantry system in Samsung electro-mechanic Inc. for ink-jet printing of Cu nanoink

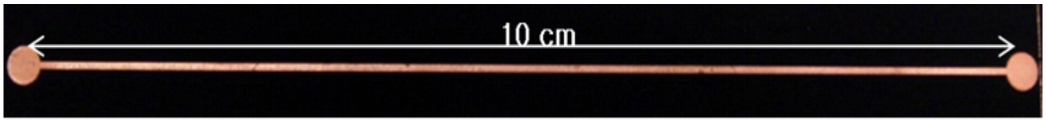

Figure 2.3: Printed electrode

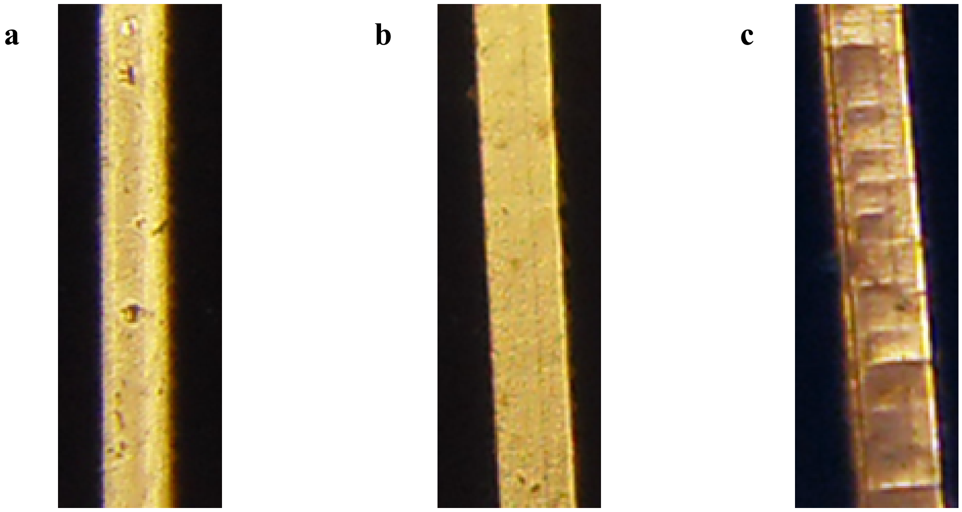

Figure 2.4: Optical microscope images of fully sintered printed electrodes: (a) 5-, (b) 10-, and (c) 20-times printed.

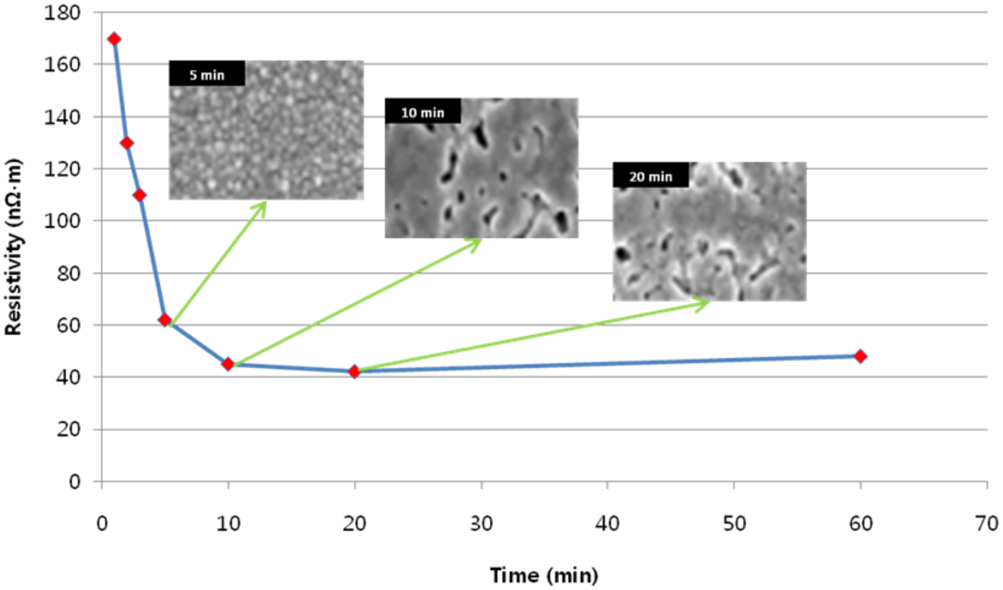

Figure 2.5: Sintering of the copper nanoparticles ink as function of sintering time.

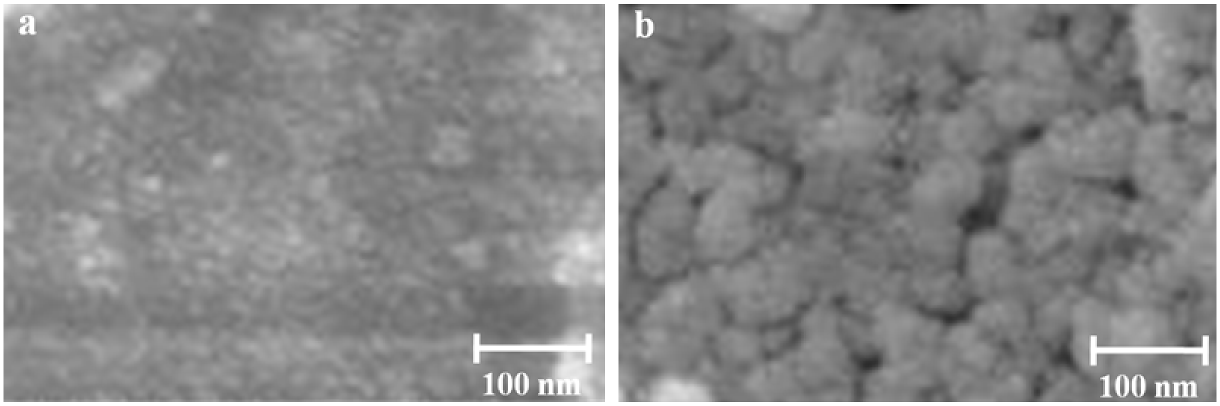

Figure 2.6: SEM images of inkjet printed electrode
(a) before, and (b) after thermal sintering.

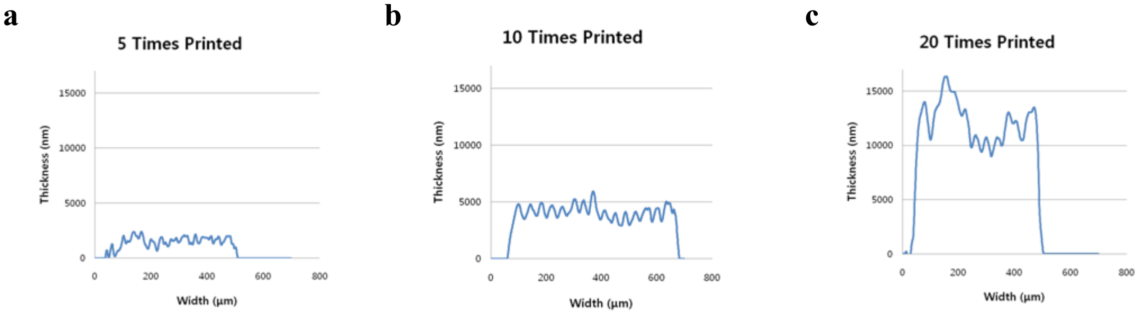

Figure 2.7: Surface profiles of printed electrode using profilometer:
(a) 5-, (b) 10-, and (c) 20-times printed.

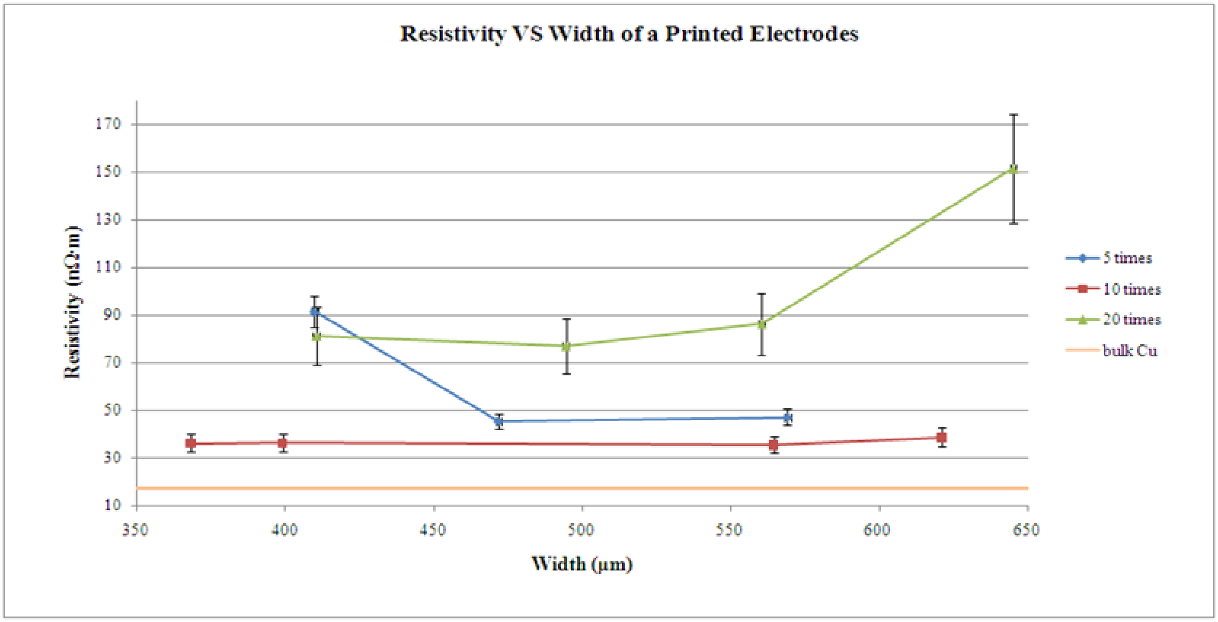

Figure 2.8: Resistivity of printed electrodes depended on their widths and number of printing compared to resistivity of bulk copper.

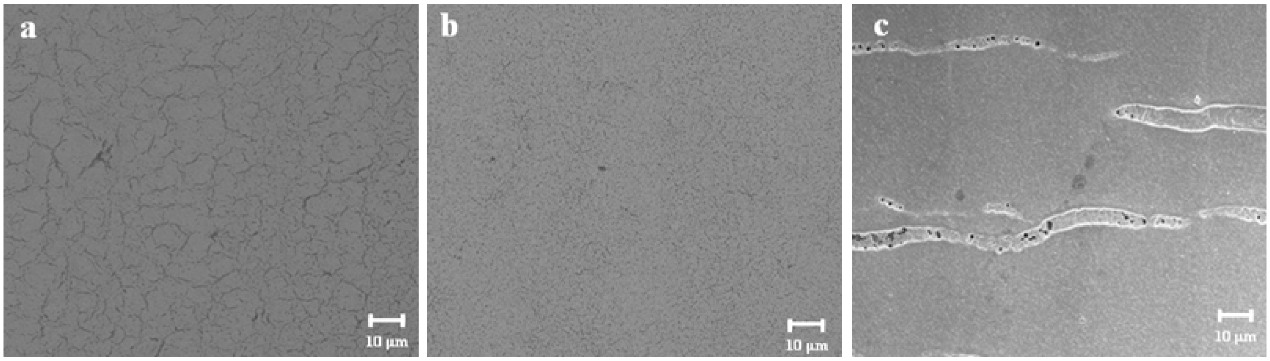

Figure 2.9: SEM images of printed electrodes at 1000 times magnification:
(a) 5-, (b) 10-, and (c) 20-times printed.

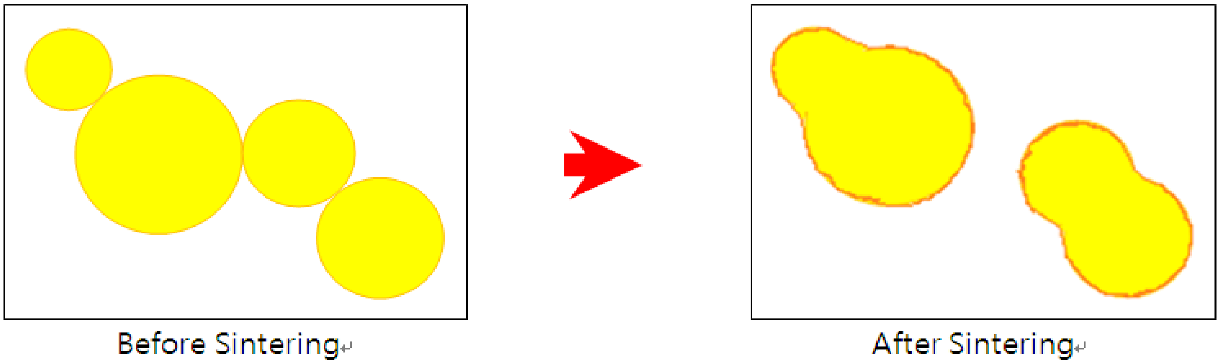

Figure 2.10: Schematic drawing of producing initial cracks.

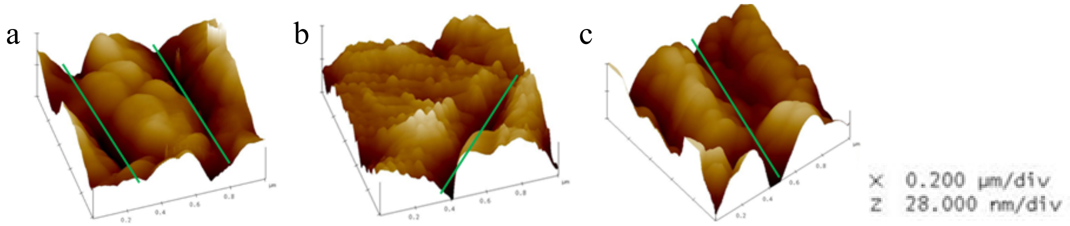

Figure 2.11: AFM images of printed electrodes with green lines passing through cracks on their top surfaces: (a) 5-, (b) 10-, and (c) 20-times printed.

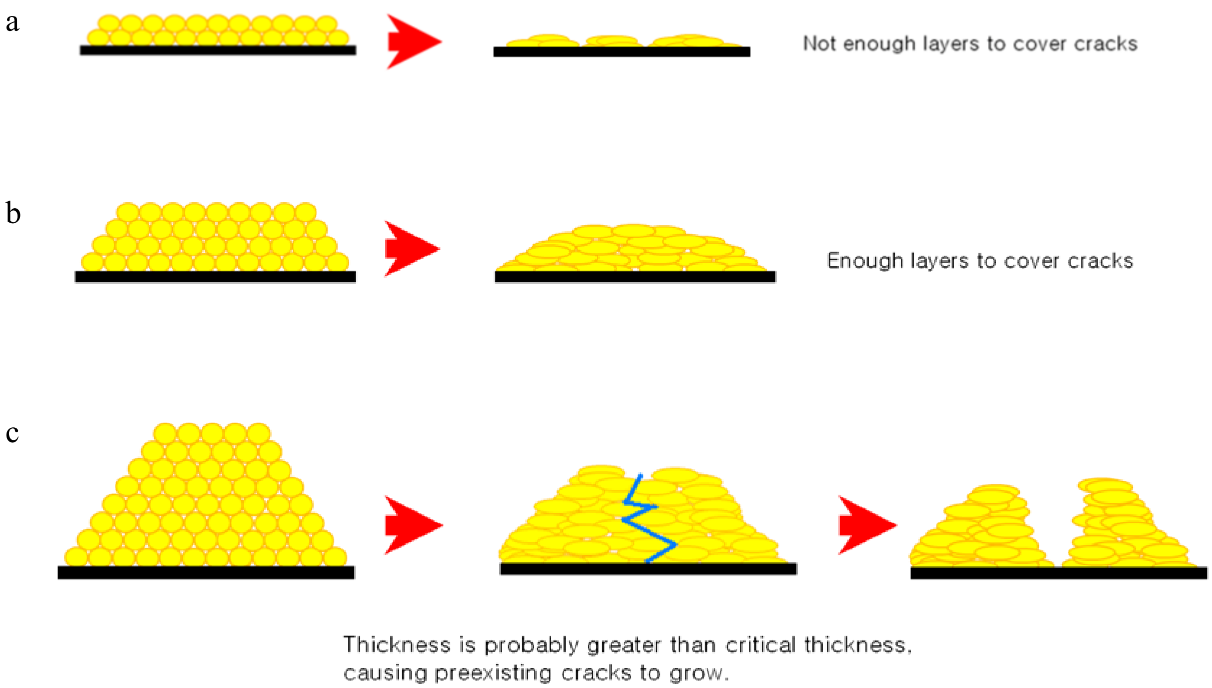

Figure 2.12: Schematic drawing of (a) producing cracks in 5-times printed electrode, (b) covering cracks in 10-times printed electrode, and (c) crack propagation in 20-times printed electrode.

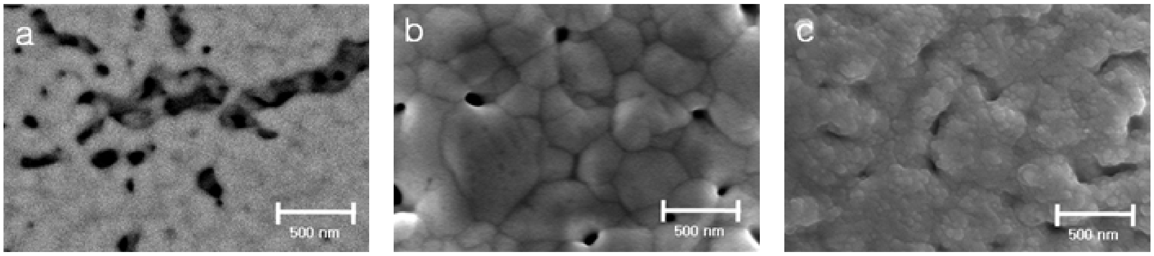

Figure 2.13: SEM images of printed electrodes at 50000 times magnification:
(a) 5-, (b) 10-, and (c) 20-times printed.

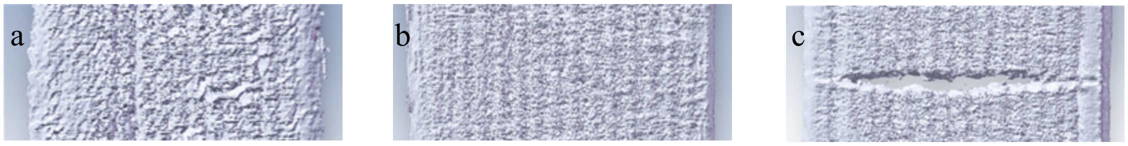

Figure 2.14: 3-dimensional top view of printed electrode using X-ray tomography:
(a) 5-, (b) 10-, and (c) 20-times printed.

CHAPTER THREE

Multifunctional Performance of Silicon Solar Cells

3.1. Introduction

Since the appropriate thickness of printed electrodes was found in the previous chapter, it is important to test different solar cells to find the one that can be integrated directly on a structural component using an inkjet printed circuit. According to Sugar et al.[1], the performance of amorphous silicon solar cells is stable up to a tensile strain of 1%, and these solar cells were still functional up to 2.4% tensile strain. Maung et al.[2] integrated a thin-film amorphous silicon solar cell onto a carbon/epoxy composite laminate by co-curing inside an autoclave, and studied its performance under fatigue loadings. There was no significant performance degradation when the solar cell was cycled between 0 and 0.3% strain.

The efficiency of amorphous silicon solar cell is about 12%. Different types of thin flexible solar cells such as Copper Indium Gallium Selenide (CIGS)[3] and organic polymer[4] solar cells are being developed to achieve higher efficiency with better mechanical durability. CIGS solar cell has about 20% efficiency[5]. However, CIGS solar cells degrade with humidity and generate toxic wastes during manufacturing[6-8]. Organic polymer solar cells are much more prone of large strains than amorphous silicon solar cells, but they are unstable and very sensitive to environmental conditions[9,10].

In the present research, single-crystalline silicon (c-Si) solar cells were studied under mechanical loading because they are known to have a high efficiency of 23%, which is higher than that of amorphous silicon solar cells. Also, the flexural fatigue of amorphous silicon (α-Si) solar cells was studied. The resulting information is critically needed in order to check the reliability of a solar cell when it is integrated on the wings of an unmanned aerial vehicles.

3.2. Experimental Details

3.2.1. Specimen Preparation

c-Si solar cells for this study were obtained from BP Solar (London, United Kingdom). Dimensions of these solar cells are $125.15 \times 125.15 \times 0.275 \pm 0.005$ mm. The average thickness of crystalline silicon is 0.200 ± 0.003 mm, and a blue anti-reflecting coating of silicon nitride is applied on the front. The average thickness of aluminum back contact is 0.075 mm, and 3 mm wide silver soldering pads are on the back of these solar cells. (Figure 3.1a)

The thin-film amorphous silicon (α-Si) solar cells were purchased from Jameco Electronics (California, United States), manufactured by PowerFilm Solar (Iowa, United States). Dimensions of these solar cells are $84 \times 37 \times 0.330 \pm 0.005$ mm. The manufacturer specification claims the thickness of amorphous silicon to be 400 nm. (Figure 3.1b)

3.2.2. Experimental Setup and Procedure

Wings of aircraft are typically subjected to about 0.2% of fatigue strain during flight. Therefore, before utilizing a solar cell as an energy harvesting source it is important to find a mechanical endurance limit. To mechanically test the c-Si solar cell, it was cut by a dicing saw (DAD-321, Disco, Japan) into 27 mm by 125.15 mm pieces. There were two types of c-Si solar cell samples. Type one samples were cut parallel to top contact electrodes, and type two samples were cut perpendicular to top contact electrodes. (Figure 3.2) Each sample was subjected to four-point bending following ASTM D7264 standards using a tabletop mechanical tester (Instron 4411, Instron, USA)[11]. The optical microscope (Olympus BX 41, Olympus, Japan) was used to analyze c-Si solar cells. For c-Si solar cells, load and displacement were recorded using a control board on a tabletop mechanical tester, then displacement data were converted into strain values using the following equation:

$$\varepsilon = \frac{4.36\delta t}{L^2} \qquad \text{Eq. 3-1}$$

where ε is strain, δ is displacement of a loading crosshead in mm, t is thickness of c-Si solar cell in mm, and L is support span in mm[11].

α-Si solar cells were subjected to flexural fatigue cycles instead of static bending. To make a sample for this testing, four layers of carbon fiber reinforced polymer (CFRP) prepregs (CYCOM 977-3, Cytec Industries, USA) were cured inside an autoclave (Thermal Equipment Corporation, United States) with a lay-up sequence of $[0, 90]_s$. A precision strain gage (EA-6-062AP-120, Micro-Measurements Division, United States) was attached on the middle of the bottom of the CFRP composite laminate, and the α-Si solar cell was attached using a two-part epoxy adhesive (Scotch-Weld DP-420, 3M, USA) on the top of the CFRP composite laminate.

The four-point bending fixture was modified so that flexural loading can be applied in full reversal: compressive load on the way down and tensile load on the way up of the crosshead. (Figure 3.3) A strain gage amplifier (Omega 941, Omega, USA), and a load cell amplifier (Omega 916, Omega, USA) were used to obtain strain and load data, respectively. Photovoltaic performances of α-Si solar cells were analyzed using a source meter (Keithley 2400, Keithley, USA). An overhead projector (Kodak Carousel 750, Kodak, USA) with a DEK 500W incandescent light bulb was used as a light source.

3.3. Results and Discussion

3.3.1. Single Crystalline Silicon Solar Cell

Following ASTM D7264 for a four-point bending test of the c-Si solar cells, the space between the outer supports was kept at 90 mm. For the type one samples, the average tensile strain was $0.15 \pm 0.01\%$. For the type two samples, the average tensile strain at failure was $0.10 \pm 0.01\%$. (Figure 3.4) The decrease in tensile strain is due to support from the aluminum back contact. For the type one samples, the aluminum back contact is covering the whole c-Si, providing an uniform support. However, for the type two samples, there is no aluminum back contact where there is 3 mm wide silver soldering pads. The absence of an aluminum back contact creates stress concentrations around the silver soldering pads. Figure 3.5 shows that the type two samples are broken where there is no aluminum back contact, and Figure 3.6 shows crack under near the bottom contact. Moreover, the tensile strain of 0.15% is not high enough to be used for the wing of an aircraft. These solar cells will thus not be able to endure the mechanical loads imposed on them.

3.3.2. Amorphous Silicon Solar Cell

For α-Si solar cells, their performances were characterized after two different flexural fatigue cycles. First set of five α-Si solar cells was subjected to a tensile strain of 0.12% and a compressive strain of -0.17%. Second set of five α-Si solar cells was subjected to a tensile strain of 0.32% and a compressive strain of -0.32%. The current-voltage (I-V) curves were obtained before testing, and after 1, 10, 30, 40, 50, 60, 70, 80, 90 and 100 cycles, respectively, using a source meter, and the current values were divided by the aperture area of 0.002108 m^2 to convert them into the current density. For both sets of solar cells, there was no noticeable change in their performance. The average short circuit current density was 2.15 ± 0.05 A/m^2, and the average open circuit voltage was 5.54 ± 0.08 V. Fill factors were calculated using the following equation:

$$FF = \frac{J_{\max} V_{\max}}{J_{sc} V_{oc}} \qquad \text{Eq. 3-2}$$

where J_{max} is the current density in A/m^2 and V_{max} is the voltage in V at the maximum power point. The maximum power point is where the product of current density, voltage, and aperture area is the maximum on the J-V curves. J_{sc} is the short circuit current in A/m^2, where J-V curve crosses the y-axis, and V_{oc} is the open circuit voltage in V, where J-V curve crosses the x-axis. (Figure 3.7) Fill factors do not decrease after flexural fatigue up to 100 cycles. Fill factor compares performance of solar cells to an ideal diode. Note that the average fill factor is 0.60 ± 0.02. Although longer fatigue testing is needed for better reliability, α-Si solar cells appear to be a good candidate to be used on an aircraft to harvest solar energy.

3.4. Conclusions

c-Si solar cells are too brittle to be directly integrated onto a CFRP composite laminate because failure occurs below 0.2% tensile strain. α-Si solar cells can endure fully reversed flexural fatigue at 0.32% strain at least up to 100 cycles. From these results, it can be inferred that α-Si solar cells can be integrated on a CFRP composite laminate to harvest solar energy.

3.5. References

[1] Sugar JG, Scaffaro R, Guo Z, Maung JK, Ju YS, Hahn HT, " Photovoltaic performance of amorphous silicon flexible solar modules under mechanical loading," In: Proceedings of the 6th international workshop on structural health monitoring, vol. 4698; 2002. pp. 180–91

[2] K. Jason Maung, H.T. Hahn, and Y.S. Ju, “Multifunctional integration of thin-film silicon solar cells on carbon-fiber-reinforced epoxy composites,” Solar Energy, vol. 84, 2010, pp. 450–458.

[3] C.A. Kaufmann, A. Neisser, R. Klenk, and R. Scheer, “Transfer of Cu (In, Ga) Se2 thin film solar cells to flexible substrates using an in situ process control,” Thin Solid Films, vol. 480, 2005, pp. 515–519.

[4] F.C. Krebs, M. Jorgensen, K. Norrman, O. Hagemann, J. Alstrup, T.D. Nielsen, J. Fyenbo, K. Larsen, and J. Kristensen, “A complete process for production of flexible large area polymer solar cells entirely using screen printing–First public demonstration,” Solar Energy Materials and Solar Cells, vol. 93, 2009, pp. 422–441.

[5] I. Repins, M.A. Contreras, B. Egaas, C. DeHart, J. Scharf, C.L. Perkins, B. To, and R. Noufi, “Short Communication: Accelerated Publication 19· 9% efficient ZnO/CdS/CuInGaSe2 solar cell with 81· 2% fill factor,” Progress in Photovoltaics: Research and Applications, vol. 16, 2008, pp. 235–239.

[6] D. Hariskos, M. Powalla, N. Chevaldonnet, D. Lincot, A. Schindler, and B. Dimmler, “Chemical bath deposition of CdS buffer layer: prospects of increasing materials yield and reducing waste,” Thin Solid Films, vol. 387, 2001, pp. 179–181.

[7] V.M. Fthenakis and W. Wang, “Extraction and separation of Cd and Te from cadmium telluride photovoltaic manufacturing scrap,” Progress in Photovoltaics: Research and Applications, vol. 14, 2006, pp. 363–371.

[8] K. Ramanathan, F.S. Hasoon, S.E. Asher, J. Dolan, and J.C. Keane, ZnO/Cu (InGa) Se2 solar cells prepared by vapor phase Zn doping, Google Patents, 2007.

[9] M. Glatthaar, M. Riede, N. Keegan, K. Sylvester-Hvid, B. Zimmermann, M. Niggemann, A. Hinsch, and A. Gombert, “Efficiency limiting factors of organic bulk heterojunction solar cells identified by electrical impedance spectroscopy,” Solar energy materials and solar cells, vol. 91, 2007, pp. 390–393.

[10] J. Nakamura, C. Yokoe, K. Murata, and K. Takahashi, “Efficient organic solar cells by penetration of conjugated polymers into perylene pigments,” Journal of applied physics, vol. 96, 2004, p. 6878.

[11] Standard test method for flexural properties of polymer matrix composite materials. ASTM 2007, D 7246M-2007

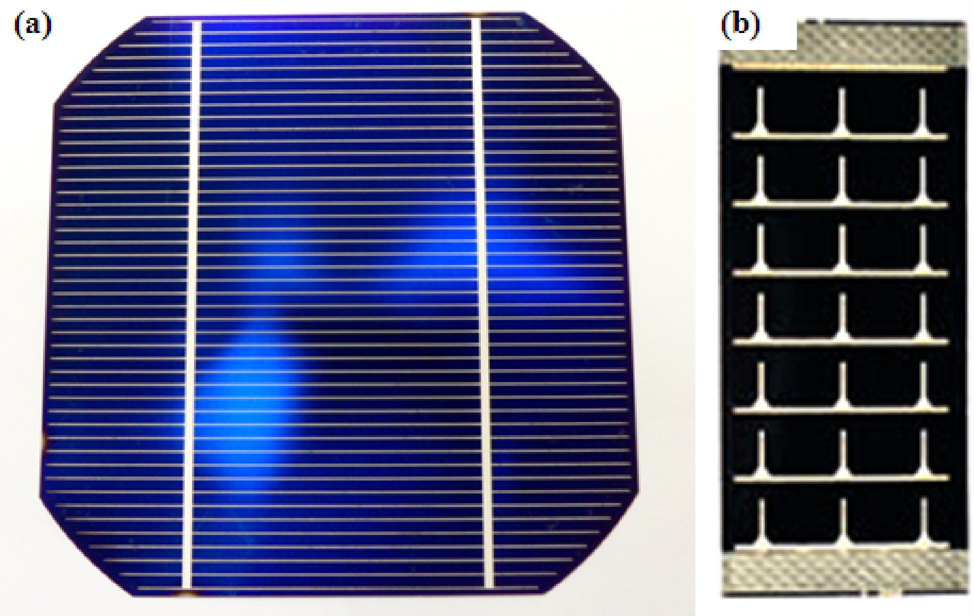

Figure 3.1: (a) c-Si solar cell from BP Solar and (b) α-Si solar cell from PowerFilm.

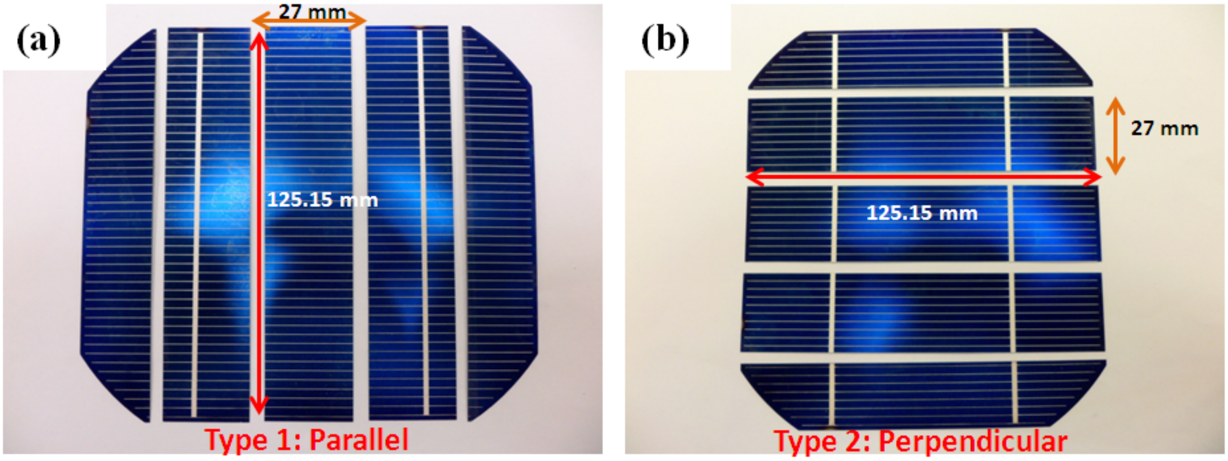

Figure 3.2: c-Si solar cells cut in (a) parallel and (b) perpendicular to top contact electrodes.

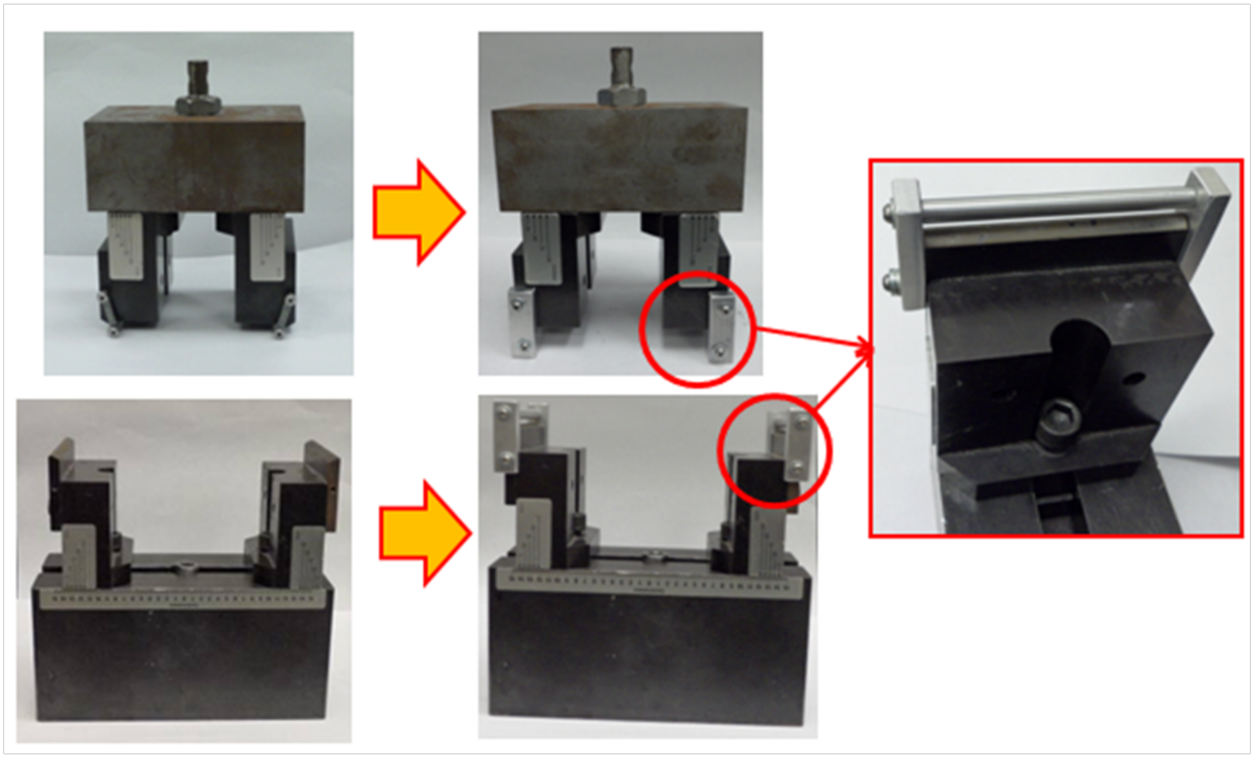

Figure 3.3: Four-point bending fixture modifications.

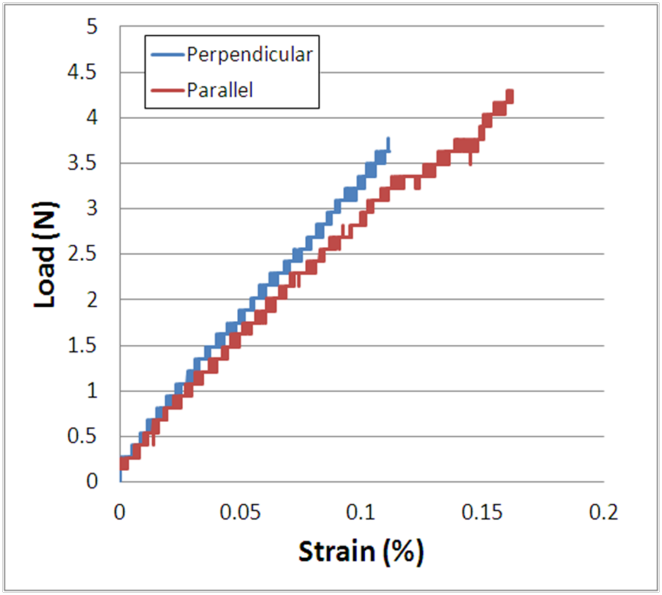

Figure 3.4: Load-strain curve of c-Si solar cells.

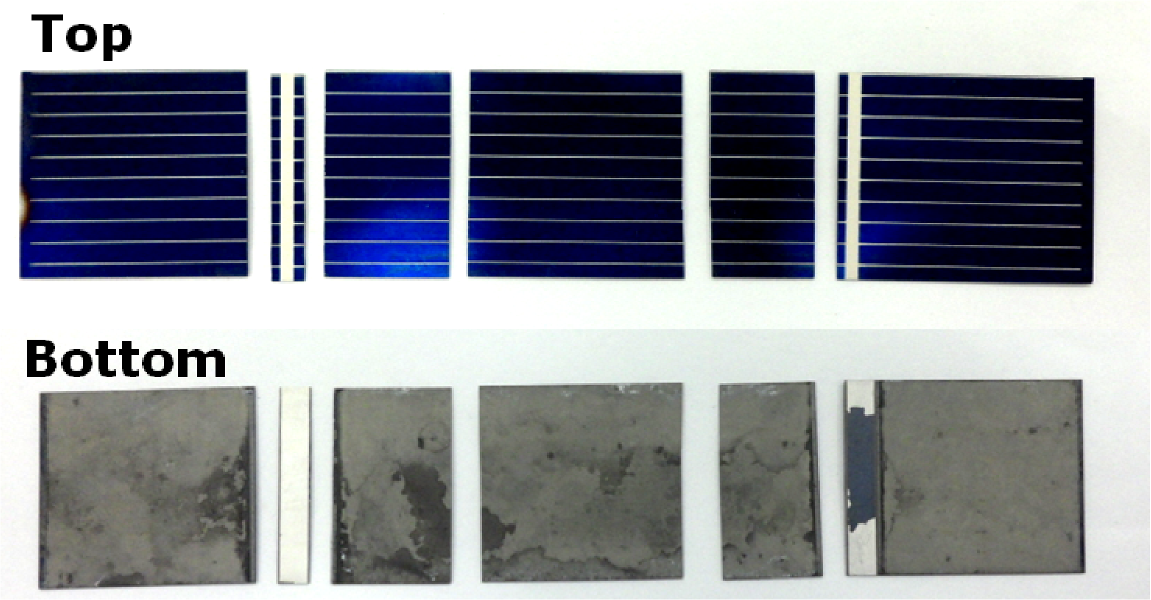

Figure 3.5: Type two c-Si solar cell samples are broken where there is no aluminum back contact.

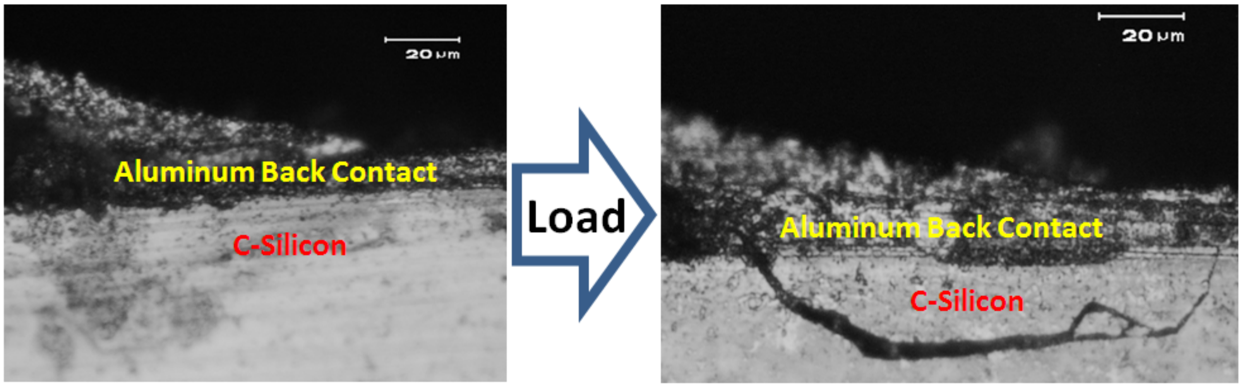

Figure 3.6: Crack near back contact of c-Si solar cells.

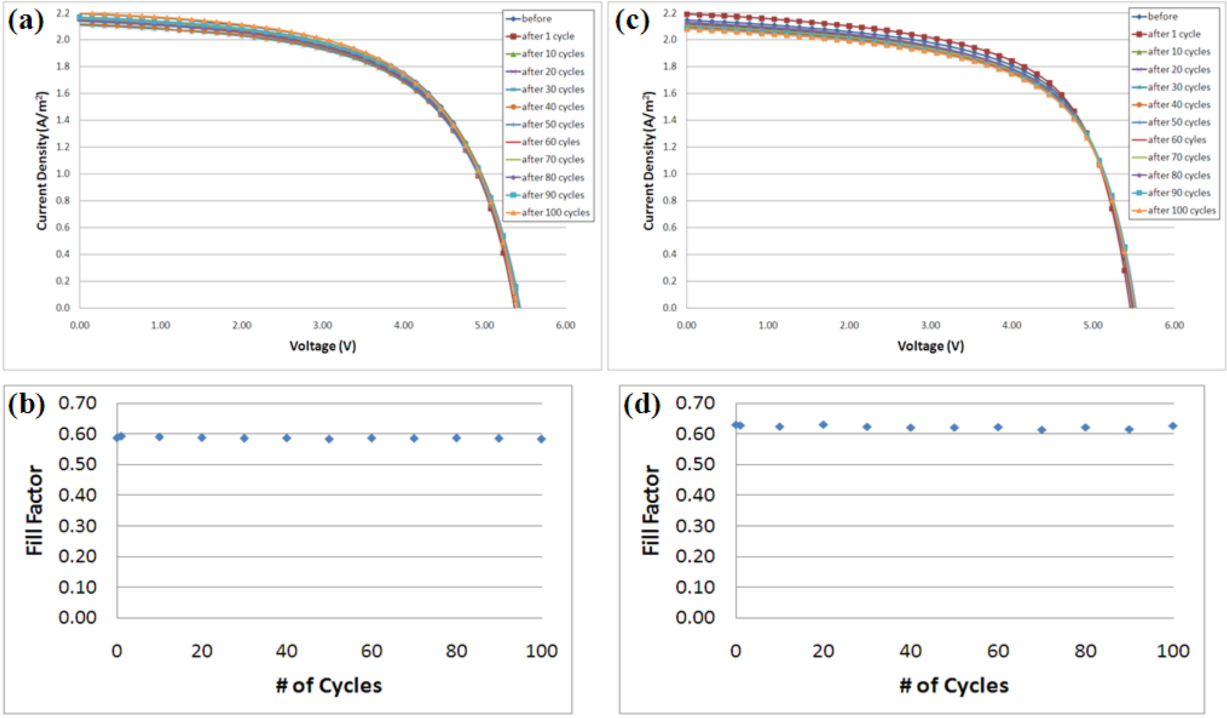

Figure 3.7: (a) J-V Curve and (b) Fill Factor for -0.17 and +0.12% strain fatigue cycle. (c) J-V Curve and (d) Fill Factor for -0.32 and +0.32% strain fatigue cycle.

CHAPTER FOUR

Multifunctional Composite Structure via Inkjet Printing

4.1. Introduction

Multifunctional composite structure is defined as the structure which can not only bear load but also perform other functions such as energy harvest and storage, sensing and actuating, and more. In order to perform multifunctional functions, a conducting circuit should be embedded within the load bearing structure. As for the patterning of conductive circuits, the conventional photolithographic method used for printed circuit boards (PCBs) is time consuming, expensive, and environmentally undesirable. As an alternative, Kim et al. and Park et al. used an ink containing nano-sized Ag or Cu particles in an inkjet printer to print conductive path on a polymer substrate[1,2]. Although the melting temperature of bulk copper is 1084°C, the authors have shown that when the particle size is in the few-nanometer range, the inkjet printed circuit sintered at a lower sintering temperature can have a high conductivity as a conventionally produced one.

Different from typical functional devices, multifunctional structures include load bearing function as well as other non-structural function. Because there is no information available, to the author's knowledge, on the structural integrity of the inkjet printed electrodes, this topic was studied in the present work.

Most energy harvest and storage systems are parasitic to load bearing structures, increasing the total weight and volume while decreasing the fuel efficiency as they require heavy transmission cables from a centralized power source. Therefore, hybrid composite structures have been developed by embedding thin-film batteries[3-5], thin-film solar cells[6,7], and thermoelectric devices[8,9] into composite laminates to have multifunctional capabilities.

In Chapter 3, a thin-film amorphous silicon solar cell was attached on a composite laminate and investigated the effect of a flexural fatigue loading on its performance. It was found that the solar cell maintains its virgin efficiency under flexural fatigue loadings. Pereira et al. investigated the performance of embedded thin-film batteries under mechanical loading[5]. Specifically, they characterized the charge and discharge characteristics under increasing levels of applied stress. Since there has been no attempt to integrate solar cells and batteries together into a load bearing structure, an energy harvest and storage composite was fabricated using an inkjet printed circuit.

In this study, the conducting circuits are placed on the laminate using an inkjet printing technique. The mechanical reliability of inkjet printed electrodes was tested under static and fatigue loadings to find if it was applicable to a multifunctional composite for an unmanned aerial vehicle. In order to show the feasibility of the inkjet printed electrode for multifunctional composite structure, an energy harvest and storage composite laminate was made using inkjet printed electrodes as interconnection between a thin-film solar cell and a thin-film battery. The thin-film solar cell, the thin-film battery and the additional passive components were co-cured with the composite laminate to form a power laminate. The performance of the power laminate is also studied under mechanical loading.

4.2. Mechanical Reliability of Inkjet Printed Electrodes

Using the printed system and copper nanoink described in the Chapter 2, the desired copper pattern was printed on a flexible BT core substrate. Because the cracks on the top surface grows when the thickness of a printed electrode is greater than 5.3 μm, the printing was repeated to make the desired electrode thickness of 1, 2, and 4 μm. The adhesion between the printed electrode and BT core was good, as shown in a simple scratch test using a diamond-tip pen, Fig. 4.1.

The BT core with the printed copper pattern was co-cured on a graphite/epoxy laminate (T700SC/RS-30G) with a lay-up sequence of $[0/90]_s$ in an autoclave following the manufacturer’s recommended cure cycle, Fig. 4.2. Figure 4.3a shows the composite specimen co-cured with the copper patterned BT core. The total thickness of the specimen is 0.67 mm which includes the 0.57-mm-thick graphite/epoxy composite.

Figures 4.3b and 4.3c show the specimen mounted on a universal tensile tester to study the effect of mechanical loading on the electrode resistance. The resistance was measured under various levels of load using a four-point probes method, Fig. 4.3d, described in Chapter 2. Figure 4.4a shows the effect of electrode thickness on the resistance under a static loading. The electrode with 4 μm thickness does not show any noticeable change up to the maximum strain applied while the two thinner electrodes (1 and 2 μm) show increased resistances. This is likely to be the results of stronger particle junctions in the electrode with 4 μm thickness. Figure 4.4b shows the resistance changes under cycling between 0 and 0.5% strain. At each cycle, a resistance measured at both 0 and 0.5% strain. Again, the electrode with 4 μm thickness does not show any change in resistance up to the maximum cycles studied. However, such is not the case with the other two thinner electrodes (1 and 2 μm); their resistances oscillate and increase as the electrodes were being loaded and unloaded. Therefore, the thickness of the electrode used in the power laminate was selected as 4 μm.

For the electrical connection test, 100 Ω resistor was connected between two short electrodes by soldering or silver pasting. Soldering ($Sn_{97}Cu_3$) was done at 260°C whereas the silver paste (Ted Pella) was cured at 60°C for 2 h, Figures 4.5a and 4.5b. Similarly to the electrode test, the resistance between two short electrodes, which were connected by a resistor, was measured under at various levels of load using the same four-point probes method, Figs. 4.3c and 4.3d. Figure 4.5c shows the resulting resistance changes of the resistors. One of the solder connections failed at 0.7% strain while the silver paste connections did not until 1.1% strain. Since the silver paste was found to be reliable under mechanical static loading, it was used for electrical connections in the power laminate.

4.3. Integrated Power Laminate

Figure 4.6a shows the circuit pattern for the integration of a solar cell and a battery on a BT core. The circuit patterns were made using the inkjet printing method on the BT core. The electrodes on the top and bottom surfaces were connected to each other through via holes, where the nanoink was smeared into and sintered. In order to insulate the electrodes from graphite fibers in the composite, polyimide ink was printed with a thickness of 25 μm and cured over the whole area of the laminate except where the solar cell and battery are to be located as shown in Fig. 4.6b. Table 4.1 shows the specifications of the amorphous silicon thin-film solar cell TX3-25 (Powerfilm Inc.). The solar cell is very thin (0.2 mm), so that it can be integrated into composite structures in various shapes without significantly increasing the total thickness. Table 4.2 shows the specification of the solid state thin-film lithium battery S8-ES (Front Edge Technology) which is remarkably thin and flexible. The top and bottom 50-μm thick mica substrates are held and sealed together around the edges with a 40-μm thick heat resistant epoxy layer, so that it can sustain the composite cure temperature of 120°C.

Figure 4.7 shows the fabrication process of the power laminate. The battery and the solar cell are attached to the BT core using an epoxy adhesive DP460 (3M) and their electrodes are connected to the printed electrodes using the sliver paste as shown in Fig. 4.7a. Each silver paste connection is sealed using the same adhesive DP460 (3M) for insulation from the conductive graphite fibers in the composite laminate. The final assembly consisting of the BT core and the composite laminate is cured in an autoclave. After the cure cycle, a diode is connected using the silver paste to prevent reverse currents flowing from the battery to the solar cell as shown in Fig. 4.7b.

Figure 4.8 shows the cross-sectional view of the power laminate. By integrating a solar cell and battery on a laminate, the total laminate thickness was increased by 0.42 mm. The multifunctional power laminate should have load bearing function as well as autonomic energy harvest/store function. Since the power laminate was fabricated on a host composite laminate, the developed multifunctional power laminate has almost the same strength and modulus with the bare composite laminate. Figure 4.9 shows the experimental set-up of the integrated power laminate to test the performance under mechanical loading. The light was shone on the solar cell using the overhead projector described in Chapter 3. The current-voltage (I-V) curve of solar cell was measured using a source meter, Keithley 2400, with a voltage sweep from 0 to 5 V at various levels of applied static strain. From the obtained I-V curve, the fill factor is calculated using Eq. 3-2; instead of J_{max} and J_{sc}, I_{max} and I_{sc} were used.

The I-V curves and fill factors of the solar cell in the power laminate at different strain levels are shown in Fig. 4.10. Both of them hardly changed up to 1% strain, which is similar to the result of Sugar et al.[5]. Figure 4.11 shows the battery's charge-discharge characteristics, and Fig. 4.12 shows the current and voltage measured during charging the battery by the solar cell at no strain and 0.4% strain. For the charge cycle, a constant voltage of 4.2 V was applied until the current drop to 0.1 mA. For the discharge cycle, the current was maintained at 1 mA until the voltage drops to 3 V. The charge and discharge capacities were then calculated by integrating the measured current over time to the cut-off point. It was found that there was no difference of charging characteristics between no strain and 0.4 % strain. Thus the energy harvested by the integrated solar cell could be stored to the embedded battery successfully through the inkjet printed electrical connection on the power laminate up to 0.4 % strain.

However, the battery performance is seen to degrade drastically at about 0.45% strain, similarly to the result of Pereira et al.[3]. The 0.45% strain for the battery failure under static loading is too low for composite structures because this battery will not be able to withstand a fatigue loading. The crack through the active materials of the thin-film solid state battery is shown in Fig. 13. Therefore, further research is required to develop batteries with high strain capability.

4.4. Conclusions

Mechanical reliability of the inkjet printed copper nanoink was tested and found to be suitable to be used in multifunctional composites. An energy harvest/storage laminate, called the power laminate, has been fabricated by using the inkjet printed circuit board as interconnection between a thin-film solar module and a thin-film battery onto a graphite/epoxy laminate. Specific conclusions from this work are as follows:

(1) All conducting circuits and connections can be made using the state-of-the-art printed electronic technique based on a copper nanoink, an inkjet printer and a thermal sintering process.

(2) The printed electrodes remained fully functional up to the maximum applied strain of 1% when they are 4 μm thick. Also, a silver paste can be used for connections.

(3) A power laminate has been fabricated by first mounting a thin-film solar module and a thin-film battery on a BT core and then co-curing the resulting assembly with a graphite/epoxy composite laminate.

(4) The energy harvest/storage characteristics of the developed multifunctional composite structure were measured under the mechanical static loading condition. From the experiment, it was found that the power laminate was reliable until 0.45% of the static strain. After 0.45% of the strain level, the battery was seen to be failed.

4.5. References

[1] D. Kim and J. Moon, “Highly conductive ink jet printed films of nanosilver particles for printable electronics,” Electrochemical and Solid-State Letters, vol. 8, 2005, p. J30.

[2] B.K. Park, D. Kim, S. Jeong, J. Moon, and J.S. Kim, “Direct writing of copper conductive patterns by ink-jet printing,” Thin Solid Films, vol. 515, 2007, pp. 7706–7711.

[3] Thomas J. P., Qidwai M. A., Matic P., Everett R. K., Gozdz A. S., Keenon M. T., and Grasmeyer J. M., “Multifunctional structure-plus-power concepts,” Proceedings of 43rd AIAA/ASME/ASCE/AHS/ASC structures, structural dynamics, and materials conference, 2002, AIAA2002-1239.

[4] J.P. Thomas and M.A. Qidwai, “Mechanical design and performance of composite multifunctional materials,” Acta materialia, vol. 52, 2004, pp. 2155–2164.

[5] T. Pereira, Z. Guo, S. Nieh, J. Arias, and H.T. Hahn, “Embedding thin-film lithium energy cells in structural composites,” Composites Science and Technology, vol. 68, 2008, pp. 1935–1941.

[6] O. Morton, “Solar energy: A new day dawning?: Silicon Valley sunrise,” Nature, vol. 443, 2006, pp. 19–22.

[7] Sugar, J. G., Scaffaro , R. Guo, Z. Maung, J. K., Ju, Y. S., and Hahn, H. T., "Photovoltaic Performance of Amorphous Silicon Flexible Solar Modules under Mechanical Loading," 2002, Proceedings of the 6th International Workshop on Structural Health Monitoring, 4698: 180-191,

[8] J. Weber, K. Potje-Kamloth, F. Haase, P. Detemple, F. Volklein, and T. Doll, “Coin-size coiled-up polymer foil thermoelectric power generator for wearable electronics,” Sensors and Actuators A: Physical, vol. 132, 2006, pp. 325–330.

[9] W. Qu, M. Plötner, and W.J. Fischer, “Microfabrication of thermoelectric generators on flexible foil substrates as a power source for autonomous microsystems,” Journal of Micromechanics and Microengineering, vol. 11, 2001, p. 146.

Table 4.1: Specification of the amorphous silicon thin-film solar cell.

Part number	TX3-25
Manufacturer	Powerfilm Inc.
Operating voltage (V)	3
Operating current (mA)	25
Typical Voc (V)	4.2
Typical Isc (mA)	35
Total size (mm)	114 x 25
Aperture size (mm)	100 x 25
Total thickness (mm)	0.2
Weight (g)	0.8
Price ($)	2.32

Table 4.2: Specification of the thin-film battery.

Company	Front Edge Technology
Part number	S8-ES
Operating voltage (V)	4
Capacity (mAh)	0.42
Total size (mm)	25.4 x 25.4
Total thickness (μm)	114
Weight (g)	0.2
Price ($)	250

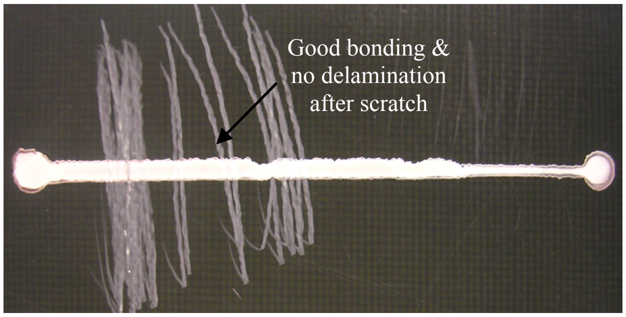

Figure 4.1: The printed copper electrode scratched experiment result.

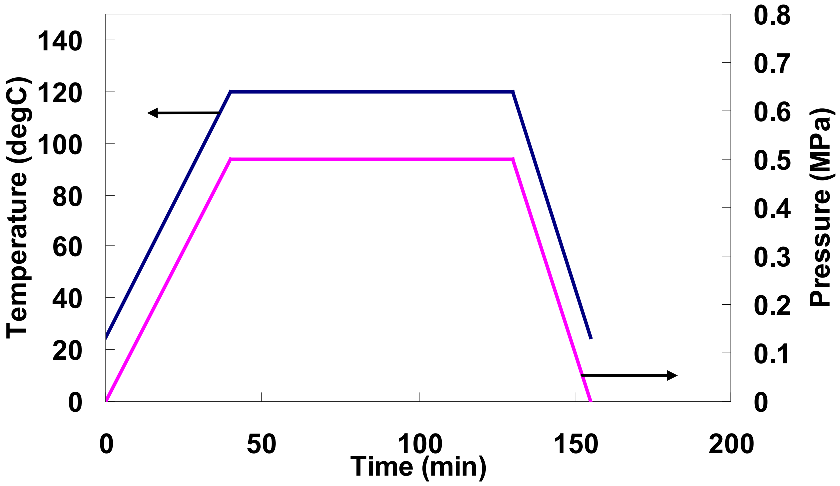

Figure 4.2: Recommended cure cycle for composite in autoclave.

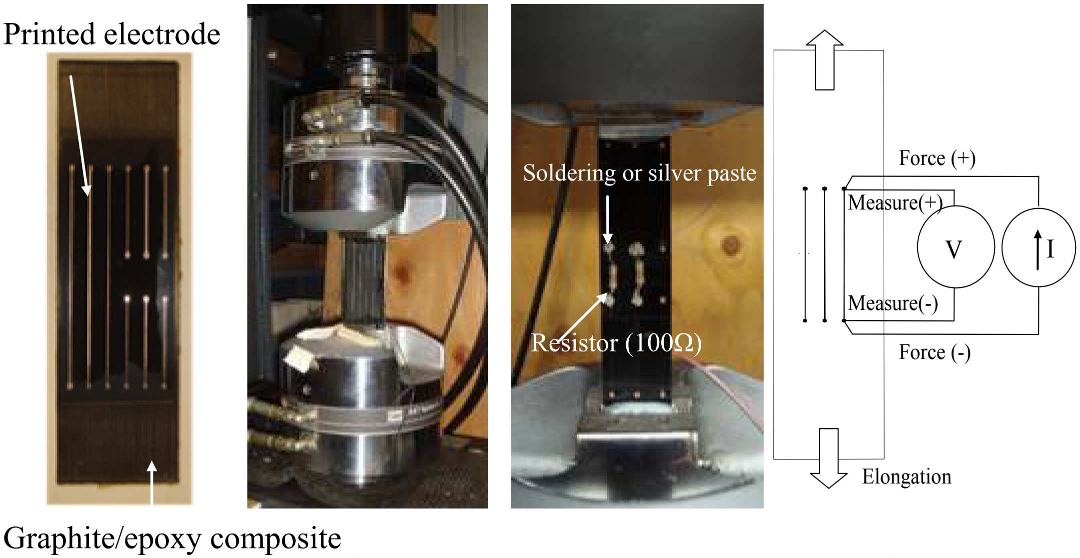

(a) (b) (c) (d)

Figure 4.3: Reliability test of the printed electronic laminate co-cured on the graphite/epoxy composite: (a) photograph of the co-cured specimen; (b) the electrode reliability specimen; (c) the electrical connection specimen; (d) a four-point probes resistance measurement.

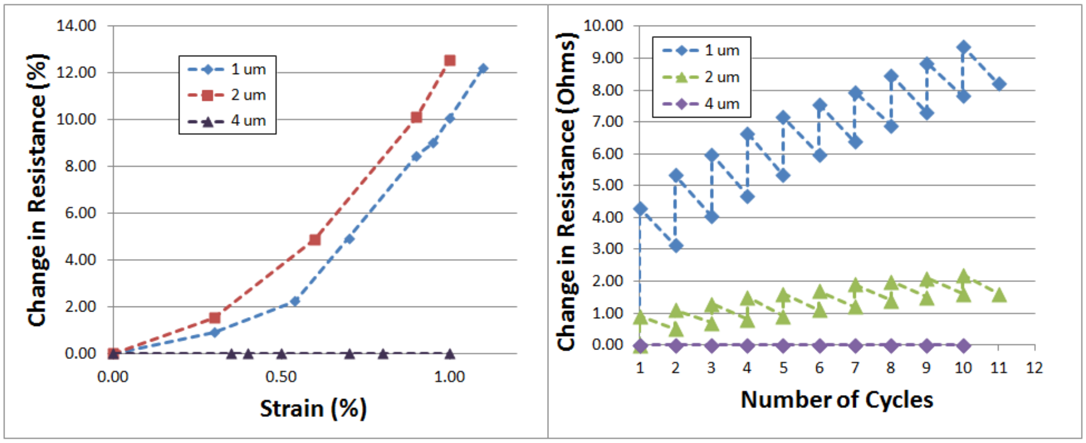

(a) (b)

Figure 4.4: Change in Resistance of the printed electrode with respect to the electrode thicknesses (a) under static loading and (b) under 0.5 % strain of fatigue.

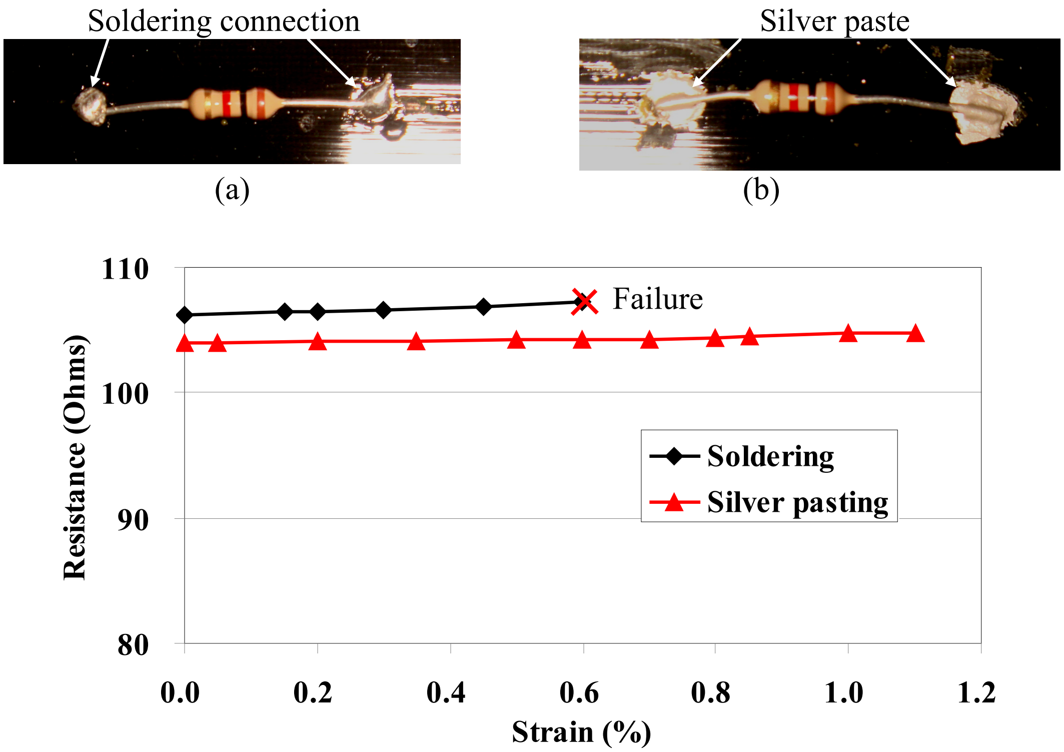

(a)

(b)

(c)

Figure 4.5: Electrical connections: (a) soldering connection; (b) silver pasting connection. (c) Resistance change of the electrical connections under static loading.

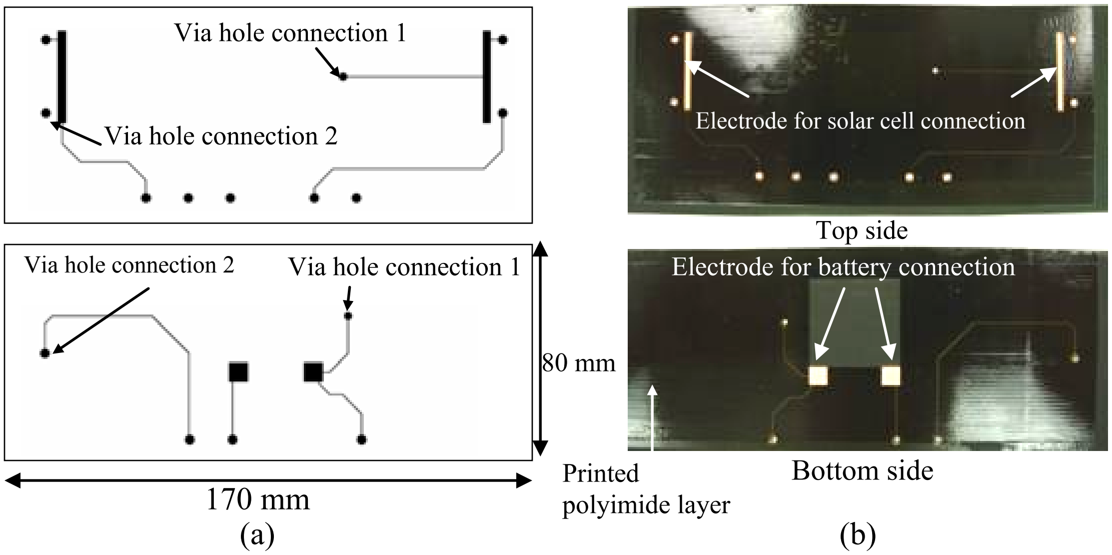

Figure 4.6: The printed electrode for integration: (a) drawing and (b) printed electronic circuit for integration.

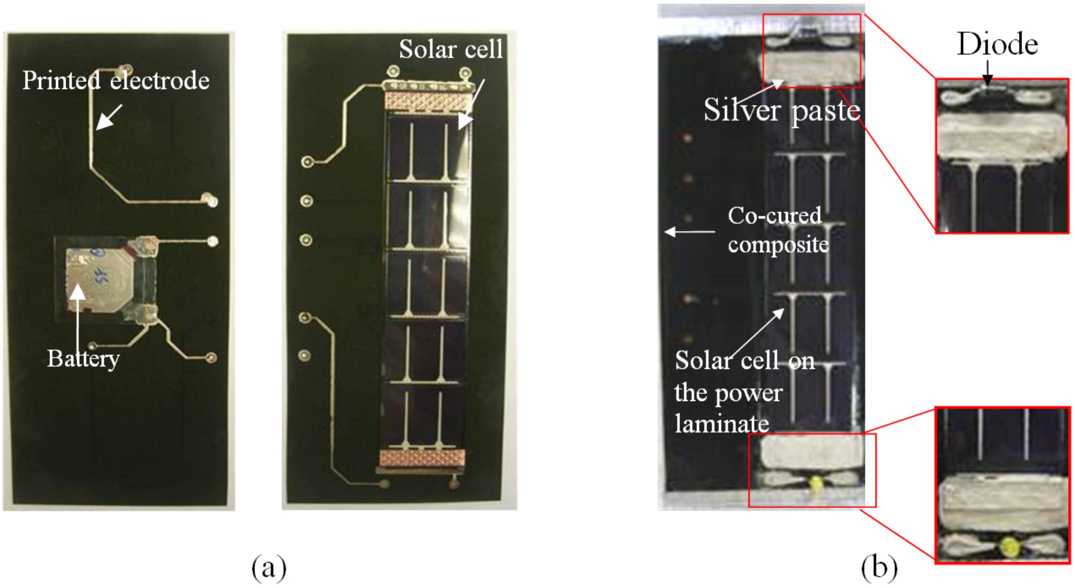

Figure 4.7: Fabrication procedure of the power laminate: (a) printed electrode pattern attached with thin-film solar cell and battery by adhesive; (b) co-cured BT core on the carbon/epoxy composite with electrical connection with diode using the silver paste.

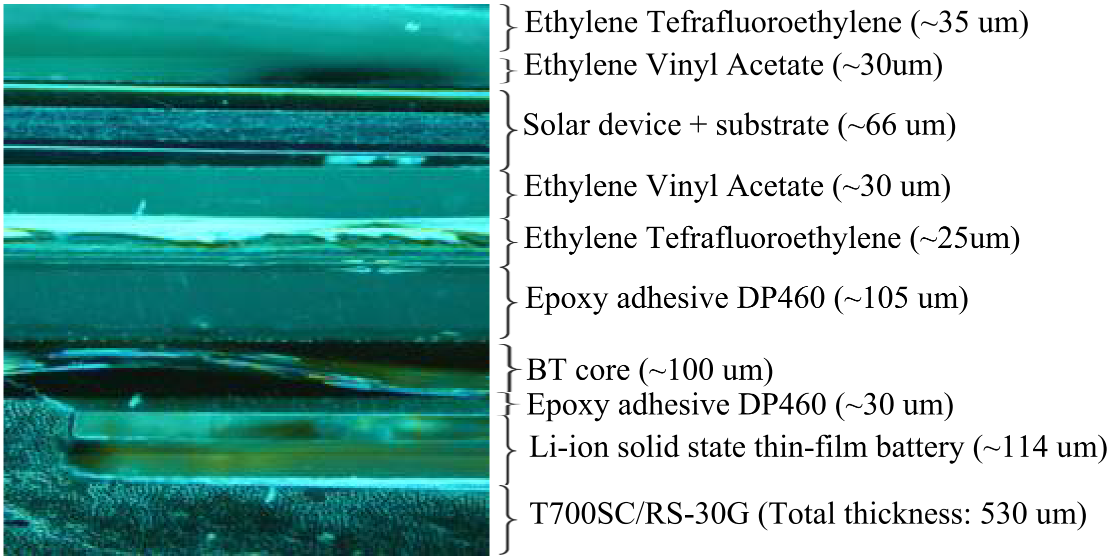

Figure 4.8: Cross section view of the power laminate co-cured composite laminate.

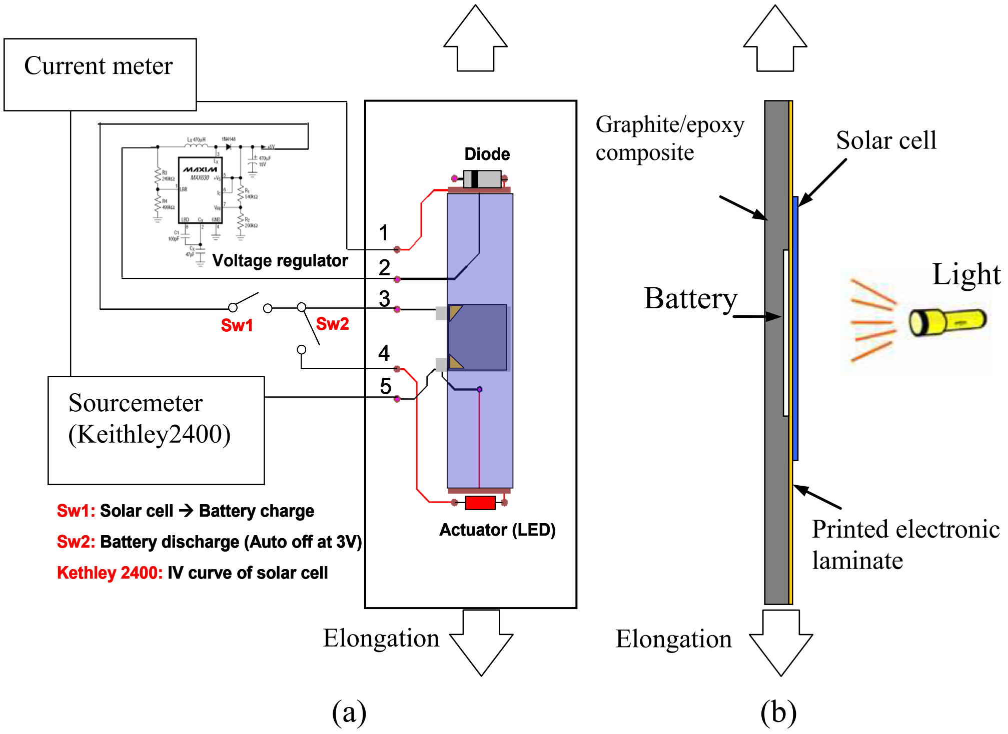

Figure 4.9: Experimental setup of the integrated power laminate: (a) schematic diagram; (b) sectional view of the power laminate.

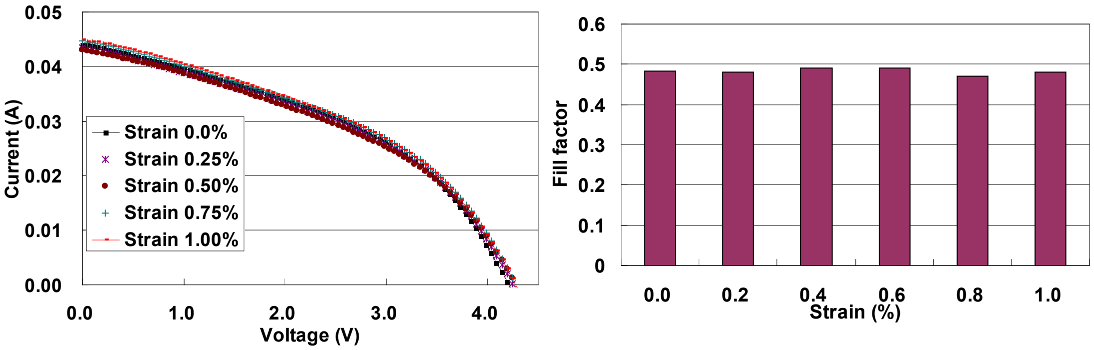

(a) (b)

Figure 4.10: Performance of the solar cell in the power laminate under mechanical loading: (a) I-V curve of the solar cell with respect to static strain; (b) fill factor of solar cell.

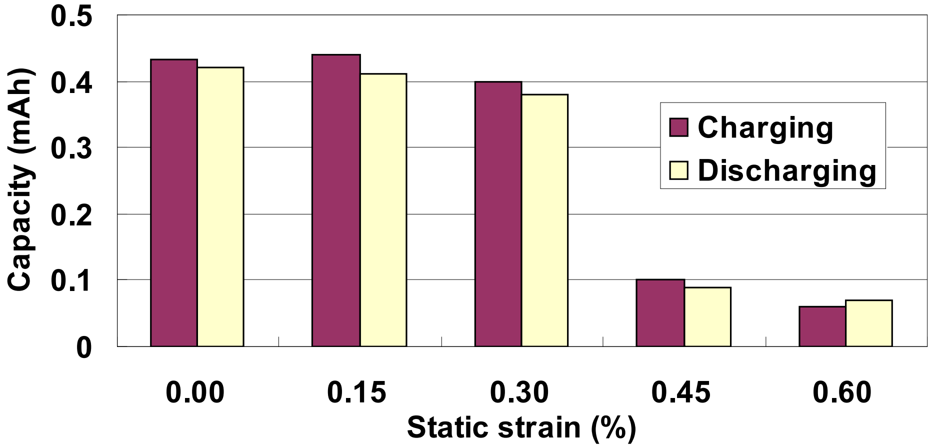

Figure 4.11: The battery characteristics under mechanical static loading: charge/discharge capacity with respect to strain.

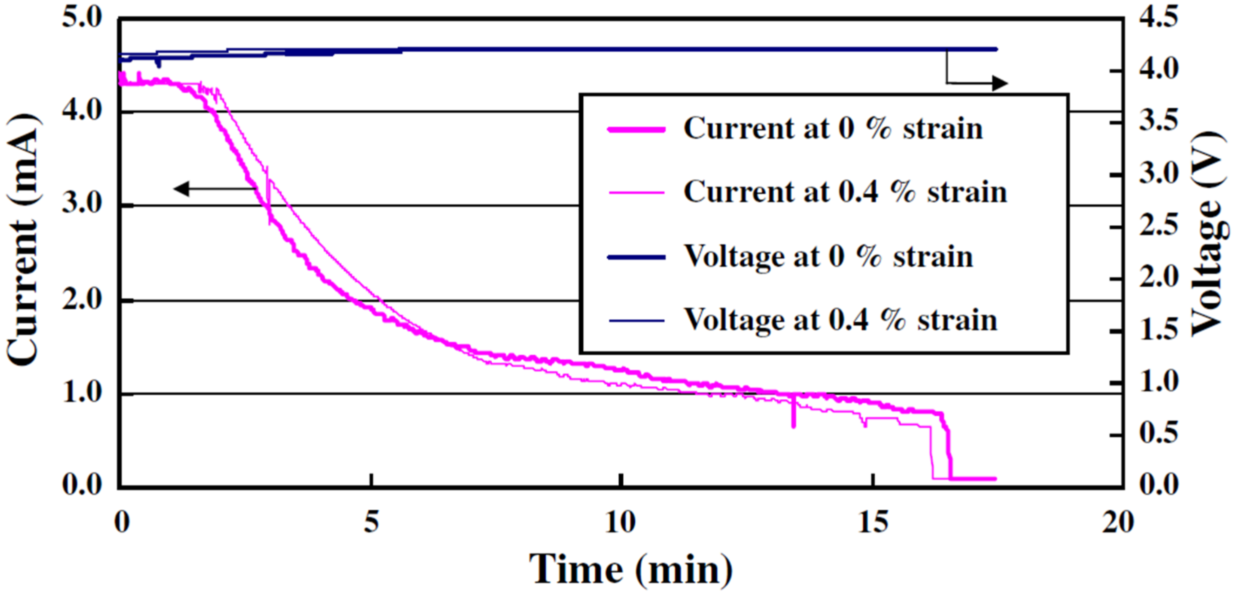

Figure 4.12: Charging characteristics of the battery from the solar cell in the power laminate at no strain and 0.4 % of static strain.

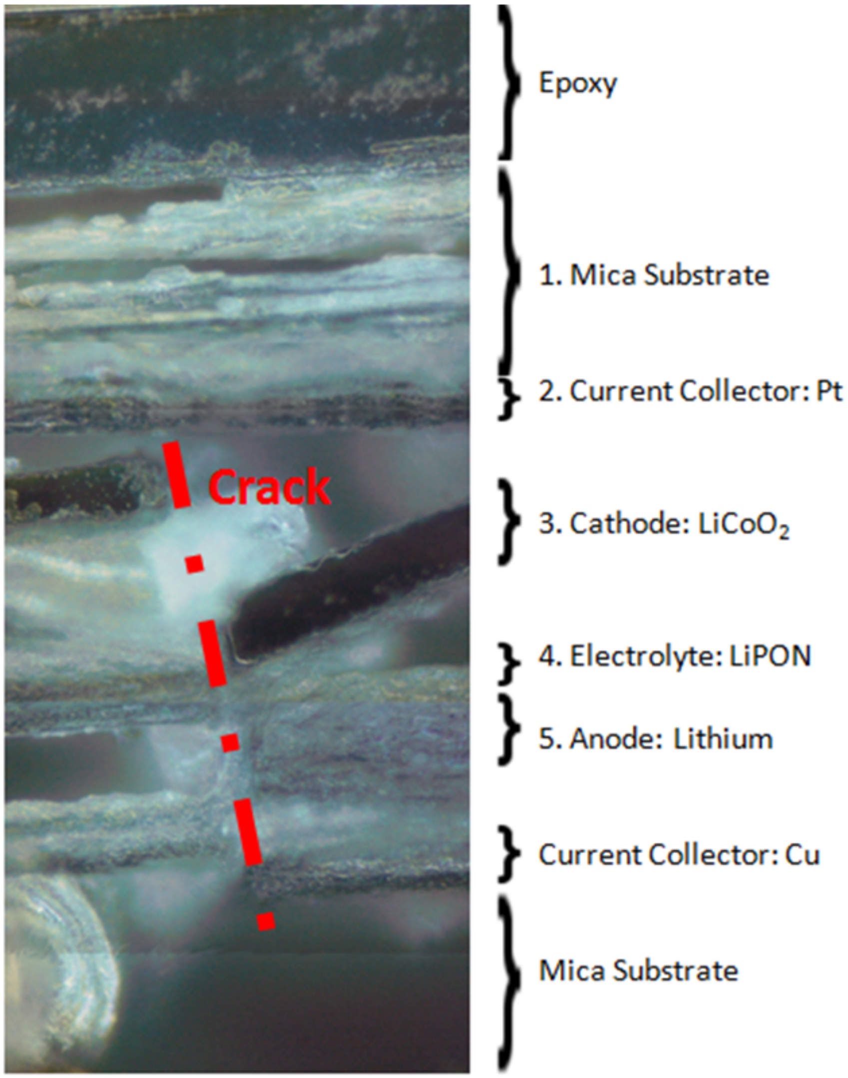

Figure 4.13: The crack propagation through the active materials of the thin-film solid state battery.

CHAPTER FIVE

Performance of Lithium-Ion Polymer Battery

5.1. Introduction

As stated in Chapter 1, reducing the weight by utilizing multifunctional structure is 50% more effective than improving the specific energy of the battery in increasing the flight time endurance of UAVs[1,2]. To help mitigate the potential weight added by such energy devices, multifunctional hybrid composite structures have been developed with load-bearing thin-film batteries[3-5], thin-film solar cells[6,7], and thermoelectric devices[8,9] integrated in the composite laminate structure.

Pereira et al.[3,4] have used thin-film solid-state batteries. These batteries are very thin, 0.14 mm, but the specific energy is only about 7.2 Wh/kg, including the packaging mass. Since most of battery constituents are made of ceramics, they are very brittle. Under bending these batteries start to degrade at 0.06% strain. This solid-state battery works at 0.37% strain but the charge and discharge capacity is less than half of the original capacity. Similarly, the thin-film solid-state battery failure occurred when a tensile stain is above 0.4% in Chapter 4. Under bending the solid-state battery performances were degrading because of packaging failure, which leads to oxidation of battery constituents. Under tensile loading the battery constituents were damaged as shown in Figure 4.13.

Unlike the thin-film solid-state batteries, the lithium-sulfur (LiS) batteries have much higher initial specific energy, reaching 250 to 350 Wh/kg[10]. However, the charge efficiency is 85% and the capacity decreases due to side reactions during charge/discharge cycle between sulfur and liquid electrolyte. Also, these batteries may self-combust and catch fire due to the growth of the lithium electrode into a branchlike structures that increases the impedance and temperature of the battery[11]. A promising alternative to solid-state and LiS batteries is the lithium-ion (Li-ion) polymer battery, which has a higher charging efficiency, 95 to 99%, than LiS batteries. Also, the Li-ion polymer battery is very stable and widely used[12].

In this research, we have studied the performance of Li-ion polymer batteries from Dow Kokam under structural and environmental loadings including compression, tensile and fatigue loadings, and temperature. The Li-ion polymer batteries were integrated into the carbon fiber reinforced polymer (CFRP) composite laminate using an out-of-autoclave co-curing method inside a thermal chamber to test the performance of the battery under fatigue loading. Mechanical loadings were applied using an Instron machine, and the temperature was varied using a furnace and a refrigerator. These batteries were charged and discharged with a source meter, and data were obtained using the same source meter as well.

5.2. Experimental Details

5.2.1. Specimen Specifications

All the batteries for this study were purchased from Dow Kokam (Midland, Miami). These were thin-film Li-ion polymer batteries. Dimensions of these batteries are 3.1 ± 0.1, 47 ± 1, and 30 ± 1 mm for thickness, length, and width, respectively. The average mass of these batteries were 9.38 ± 0.3 g. The operating voltage of these batteries was 3.7 V, and the end of discharge voltage cutoff was 2.8 V. The manufacturer specification claims the energy density of 143 mAh/g for these cells.

The battery is basically multilayer composite both functionally and structurally. For casing, cast polypropylene/ aluminum/ nylon composite 0.155 ± 0.002 mm thick is used. For energy storage, the battery has 12 cathodes and 11 anodes arranged in alternation. The cathode consists of a 0.026 ± 0.002 mm thick layer of lithium cobalt oxide ($LiCoO_2$) and lithium cobalt manganese nickel oxide ($LiMnNiCoO_2$) blend coated on a 0.031 ± 0.002 mm thick aluminum current collector. The anode, on the other hand, has a 0.029 ± 0.002 mm thick layer of graphite coated on a 0.062 ± 0.002 mm thick copper current collector. A polyvinylidene fluoride (PVDF) separator of 0.014 ± 0.002 mm thickness is used for this battery. The packaged battery is shown in Fig. 5.1.

5.2.2. Experimental Setup and Procedure

In order to establish a reference capacity, five batteries were subjected to three consecutive charge/discharge cycles between 2.8 and 4.2 V at 0.05C (17.5 mA) and five more at 2.5C (875 mA) using a source meter (Keithley 2400, Keithley, USA). The resulting current and voltage were recorded at every second, and the charge/discharge capacity was calculated by:

$$C = \int_0^{\tau} i \cdot dt \qquad \text{Eq. 5-1}$$

The battery was loaded on a tabletop mechanical tester (Instron 4411, Instron, USA) up to 1.7% strain because typically, the maximum tensile strain of CFRP composite laminates is 1.5% strain. Strain and load were recorded using a strain gage amplifier (Omega 941, Omega, USA), and a load cell amplifier (Omega 916, Omega, USA), respectively. A precision strain gage (EA-6-062AP-120, Micro-Measurements Division, USA) was attached on the middle of the battery, and aluminum tabs were attached on both ends of the battery using a two-part epoxy adhesive (Scotch-Weld DP-420, 3M, USA). The battery was then subjected to charge and discharge cycles at different strain levels.

Also, the battery was tested in compression in the thickness direction using the custom-made fixture shown in Fig. 5.2. A table-top mechanical tester was used for a pressure up to 3 MPa, and a servo-hydraulic mechanical tester (Instron 8516, Instron, USA) was used for pressure higher than 3 MPa.

Effect of temperature on the performance of the battery was studied using a furnace (Type 1400 Furnace, Barnstead Thermolyne, USA) for temperatures higher than 25°C (50, 60, 70 and 80°C), a mini- refrigerator (Chefmate, USA), for -3°C, and a chest freezer (GE, USA), for -27°C. The temperature of the battery was monitored using a thermocouple (HH 501, Omega, USA). At high temperatures, the batteries were charged and discharged at 2.5 C-rate. At low temperatures, the batteries were discharged at 1/12 C-rates, respectively. Between each cycle, soaking time was two hours.

The battery was co-cured inside a carbon/epoxy composite laminate using an out of autoclave co-curing method at 80°C inside a thermal chamber (Gravity Oven, Linberg/BlueM, USA). (Figure 5.3a) Six layers of carbon fiber reinforced polymer prepregs (CYCOM 754, Cytec Industries, USA) were used with a lay-up sequence of $[0]_6$; the battery was located in the middle of the lay-up. Before co-curing the Li-ion polymer battery and the pre-pregs together, a flat flexible cable coated with polyester (Shielded FFC Cable, Nicomatic, USA), 240 μm thick and 5 mm wide, was connected to positive and negative steel connectors by wrapping with a carbon tapes (Carbon conductive tabs, Ted Pella, USA). (A flat flexible cable was used instead of an inkjet printed circuit because an alligator clip has to be attached to monitor a current and voltage of the Li-ion polymer battery.) Then, a silver paint (Colloidal Silver, Ted Pella, USA) was used to ensure conductive paths. These connections were dried inside a thermal chamber at 60°C for four hours. After the extended connections were completely attached, an epoxy adhesive (5 Minute Epoxy, Devcon, USA) was used to insulate connectors from carbon fibers. (Figure 5.3b) These laminates were tested under tension-compression and tension-tension fatigue loadings using a servo-hydraulic mechanical tester while the embedded batteries underwent charge and discharge cycles at 2.5 C rate.

5.3. Results and Discussion

To obtain the baseline performance, the Li-ion polymer batteries were charged and discharged at 0.05 and 2.5 C-rates. As Figs. 5.4a and 5.4b shows, average charge and discharge capacities are 349.8 ± 0.3 and 348.5 ± 0.2 mAh, respectively at 0.05 C-rate. The batteries were fully charged and discharged meeting their specifications given by Dow Kokam. However, as the C-rate was increased to 2.5, the charge and discharge capacities decreased to 290.7 ± 0.6 and 289.9 ± 0.5 mAh, respectively, which is only 82.9% of their full capacity due to larger transition resistance of Li-ions between the electrodes and the electrolyte. (Figure 5.5) The capacity of Li-ion polymer batteries is known to decrease as the C-rate increases[12,13].

The specimen and the experimental setup to characterize the Li-ion polymer battery under various mechanical and environmental conditions are shown in Fig. 5.6. This test was performed to ensure that the battery is elastic enough to endure tensile loadings while it is embedded inside CFRP composite laminates. Due to lithiation during charging and de-lithiation during discharging, a tensile strain on the Li-ion polymer battery was changing during charge and discharge cycle. Fig. 5.7 shows change in a tensile strain. When the Li-ion polymer battery was charged at 0.191% strain, the tensile strain measured by the strain gage decreased to 0.136%. However, the tensile strain increased back to 0.195% when the battery was discharged. The change in strain is due to the change in thickness of the anode, which is made of graphite, during lithiation and de-lithiation. The volume of the graphite increases as Li diffuses into the lattice during charging, and vice versa[14]. These phenomena were observed through measuring the change of thickness of the Li-ion polymer battery as well. When the Li-ion polymer battery was charged, the thickness of the Li-ion polymer battery was increased by 48 ± 5 μm on average, compared to the thickness of the completely discharged Li-ion polymer battery. In contrast, when the Li-ion polymer battery was discharged, the thickness of the Li-ion polymer battery decreased by 46 ± 5 μm on average, compared to the thickness of the completely charged Li-ion polymer battery. The average charge and discharge capacities of these batteries were 326.6 ± 0.5 and 324.0 ± 0.4 mAh, respectively. As Fig. 5.8 shows, the battery works even when it is strained up to 1.655% strain. Therefore, the battery will not fail unless its CFRP substrate breaks.

Secondly, these batteries were subjected to compression to find the strength of packaging and the performance of the battery under compression. A fixture was custom-made using Poly(methyl methacrylate) (PMMA or Plexiglass) so that the Li-ion polymer battery could be charged or discharged while it is under compression. Up to 8.14 MPa, the Li-ion polymer batteries were charged and discharged at 2.5 C-rate. As Fig. 5.9 shows, there was no noticeable change in the capacities of batteries. This pressure is much higher than 0.55 MPa, the typical pressure required for the CFRP composite laminate curing. The compression on the battery was increased even further to find the strength of packaging. On average, the packaging of these batteries were able to withstand up to 22.8 ± 0.6 MPa. Above this pressure, the packaging was ruptured, and a liquid electrolyte was leaking out. Fig. 5.10 shows the Li-ion batteries after their packaging were ruptured. However, the Li-ion polymer batteries were working at 2.5 C-rate even after packaging vacuum was broken. Due to oxidation of battery constituents and leakage of a liquid electrolyte, the capacities were decreasing gradually after the packaging was ruptured. The thicknesses of the batteries decreased to 2.8 ± 0.1 mm after compression.

The effects of high temperatures on the performances of the Li-ion polymer batteries are important because the integration of those batteries inside CFRP composite laminate requires high curing temperature. Since CYCOM 754 pre-pregs from Cytec Industries can be cured at temperatures of 70 and 80°C, the performances of the Li-ion polymer batteries were analyzed at 50, 60, 70 and 80°C. On the average, there were 7.9% increases in the capacities due to decrease in the internal resistances at higher temperatures. (Figure 5.11) The temperatures above 80°C were not considered because the boiling point of ethylene carbonate is 90°C. (It is one of the solvents in the liquid electrolyte.) Moreover, the effects of low temperatures on the performances of the Li-ion polymer batteries are important because many UAVs are operating at high altitude where temperatures are below 0°C[15,16]. Therefore, the batteries were charged and discharged at the low temperatures of -3 and -27°C. Since these batteries on UAVs will be discharged overnight, the fully charged batteries were discharged at 1/12 C-rate. At this rate, the batteries were able to reach 100% depth of discharge. (Figure 5.12)

Since the Li-ion polymer battery was not damaged at 80°C, the battery was integrated inside the CFRP composite laminate to analyze the performance of the battery under fatigue loadings. The Li-ion polymer battery was placed in the middle of the CFRP composite laminate with $[0]_6$ lay-up sequence by co-curing at 80°C. The thickness, width and length of the Li-ion polymer battery and CFRP composite laminate were 4.6 ± 0.1, 56 ± 1 and 221 ± 3 mm, respectively. The performance of the Li-ion polymer battery was characterized under two different fatigue cycles: tension-compression and tension-tension. Fig. 5.13a shows the experimental setup for the composite laminate with the battery under tensile and fatigue loading. For the tension-compression cycles, the tensile strain was 0.11% and compressive strain was -0.17%. However, since the span length of the composite laminate was very long compared to its thickness, the composite laminate was buckling under compressive loading. For the tension-tension cycle, the minimum tensile strain was 0.035%, and the maximum tensile strain was 0.38%. For the both cycles, the frequency of each cycle was kept at 0.2 Hz, and the charge and discharge were done at 2.5 C-rate. Fig. 5.13b and 5.13c shows loads and strains for each cycles. Also, the strain range for both types of fatigue loadings were about 0.3% strain because for the most aircrafts, the fatigue strains are well kept below 0.3% strain[17].

As shown in Fig. 5.14, the discharging voltage value oscillates as fatigue loading was applied. The sudden drops in voltage are due to the separation of active layers of the Li-ion polymer battery. During each cycle, the maximum tensile loading compresses the battery, resulting in decreasing of distances between each layers and increasing of contact areas. (Figure 5.15) When the composite laminate was under compression, it underwent buckling because the composite laminate was long compared to its thickness. Since the Li-ion polymer battery was in the tensile side, the Li-ion polymer battery was compressed, experiencing the same effect as if the Li-ion polymer battery was under the maximum tensile loading. Fig. 5.16a,b shows changes in discharging voltages of the Li-ion polymer batteries during fatigue cycles. As a result, the capacities of the Li-ion polymer batteries dropped by 18.8% for the tensile-compression cycle and 32.9% for the tensile-tensile cycle. (Figure 5.17) The capacities of the Li-ion polymer batteries for the tensile-tensile fatigue cycle dropped more because in the tension-compression cycle, the Li-ion polymer batteries are compressed at both extremes. On the other hand, the tension-tension cycle compresses the Li-ion polymer battery at the maximum tension only.

5.4. Conclusions

The Li-ion polymer battery by Dow Kokam was characterized for an energy harvest and storage laminate application. This battery was able to achieve 100% depth of discharge at a low temperature of -27°C under 1/12 C-rate. Not only at low temperature, but also, this battery was working without any decrease in the capacity at high temperatures up to 80°C, having average capacity of 306.4 ± 0.3 mAh at 2.5 C-rate. Under compression, the packaging of the battery was able to withstand 22.8 MPa, and under tension, these batteries were able to endure 1.655% strain without decrease in its capacity. Since the Li-ion polymer battery is tolerance to various temperatures and mechanical loadings, these batteries can be used for an UAV operating at a high altitude for communications, surveillances, and disaster relief. However, the Li-ion polymer battery should not be embedded by co-curing method inside a CFRP composite laminate because its capacity decreased under fatigue loadings. Future work on integration methods that keeps a battery away from mechanical loadings would lead to improvement in the capacity of a battery for UAVs.

5.5. References

[1] Thomas J. P., Qidwai M. A., Matic P., Everett R. K., Gozdz A. S., Keenon M. T., and Grasmeyer J. M., “Multifunctional structure-plus-power concepts,” Proceedings of 43rd AIAA/ASME/ASCE/AHS/ASC structures, structural dynamics, and materials conference, 2002, AIAA2002-1239.

[2] Thomas., J. P., Qidwai., M. A., “Mechanical design and performance of composite multifunctional materials,” Acta materialia, 2004, 52:2155-2164

[3] T. Pereira, R. Scaffaro, S. Nieh, J. Arias, Z. Guo, and H.T. Hahn, “The performance of thin-film Li-ion batteries under flexural deflection,” Journal of Micromechanics and Microengineering, vol. 16, 2006, p. 2714.

[4] T. Pereira, R. Scaffaro, Z. Guo, S. Nieh, J. Arias, and H.T. Hahn, “Performance of thin-film lithium energy cells under uniaxial pressure,” Advanced Engineering Materials, vol. 10, 2008, pp. 393–399.

[5] H.S. Kim, J.S. Kang, J.S. Park, H.T. Hahn, H.C. Jung, and J.W. Joung, “Inkjet printed electronics for multifunctional composite structure,” Composites Science and Technology, vol. 69, 2009, pp. 1256–1264.

[6] Sugar, J. G., Scaffaro , R. Guo, Z. Maung, J. K., Ju, Y. S., and Hahn, H. T., "Photovoltaic Performance of Amorphous Silicon Flexible Solar Modules under Mechanical Loading," Proceedings of the 6th International Workshop on Structural Health Monitoring, Stanford, CA, September 11-13, 2007.

[7] K. Jason Maung, H.T. Hahn, and Y.S. Ju, “Multifunctional integration of thin-film silicon solar cells on carbon-fiber-reinforced epoxy composites,” Solar Energy, vol. 84, 2010, pp. 450–458.

[8] J.W. Stevens, “Heat transfer and thermoelectric design considerations for a ground-source thermo generator,” Thermoelectrics, 1999. Eighteenth International Conference on, 1999, pp. 68–71.

[9] E.E. Lawrence and G.J. Snyder, “A study of heat sink performance in air and soil for use in a thermoelectric energy harvesting device,” Thermoelectrics, 2002. Proceedings ICT'02. Twenty-First International Conference on, 2002, pp. 446–449.

[10] J.R. Akridge and Y. Mikhaylik, "Lithium-Sulfur Secondary Battery: Chemistry and Practical System Performance," 2005 International Conference on Polymer Batteries and Fuel Cells, Las Vegas, Nevada, June 12-17, 2005.

[11] A. Rapinett, “Zephyr: A High Altitude Long Endurance Unmanned Air Vehicle,” University of Surrey, 2009.

[12] H.H. Sumathipala, J. Hassoun, S. Panero, and B. Scrosati, “Li-LiFePO 4 rechargeable polymer battery using dual composite polymer electrolytes,” Journal of Applied Electrochemistry, vol. 38, 2008, pp. 39–42.

[13] N. Li and C.R. Martin, “A high-rate, high-capacity, nanostructured Sn-based anode prepared using sol-gel template synthesis,” Journal of the Electrochemical Society, vol. 148, 2001, p. A164.

[14] Y. Qi and S.J. Harris, “In Situ Observation of Strains during Lithiation of a Graphite Electrode,” Journal of The Electrochemical Society, vol. 157, 2010, p. A741.

[15] R. J. Havens, R. T. Koll, and H. E. LaGow, “The pressure, density, and temperature of the earth's atmosphere to 160 kilometers,” Journal of Geophysical Research, vol. 57, no. 1, pp. 59–72, 1952.

[16] H. Eisenbeiss, “A mini unmanned aerial vehicle (UAV): system overview and image acquisition,” International Archives of Photogrammetry. Remote Sensing and Spatial Information Sciences, vol. 36, no. 5, 2004.

[17] R.J. Diefendorf and E. Tokarsky, “High-performance carbon fibers,” Polymer Engineering & Science, vol. 15, 1975, pp. 150–159.

Figure 5.1: The Li-ion polymer battery from Dow-Kokam.

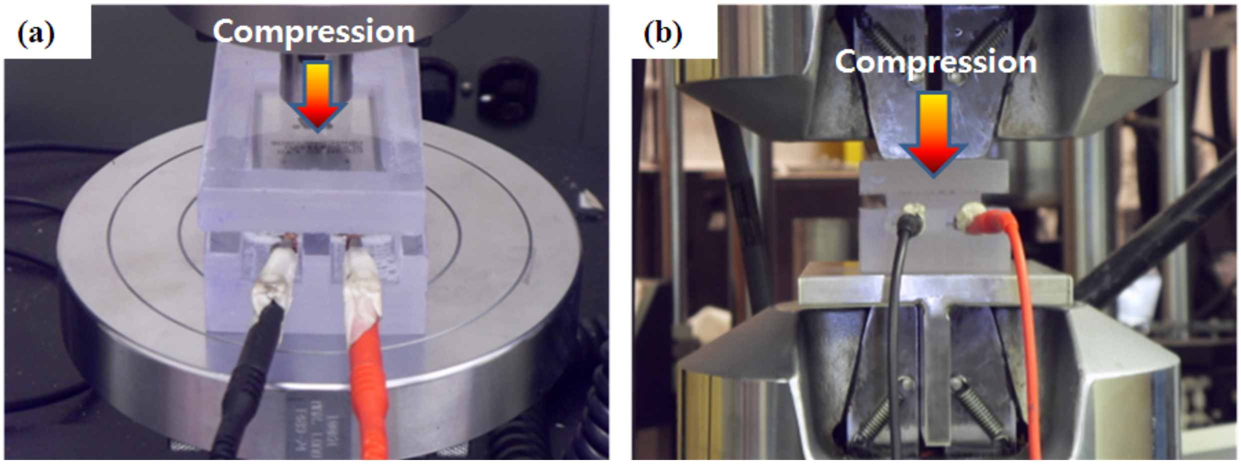

Figure 5.2: The experimental setup for the Li-ion polymer battery under uni-axial pressure: (a) below and (b) above 3 MPa.

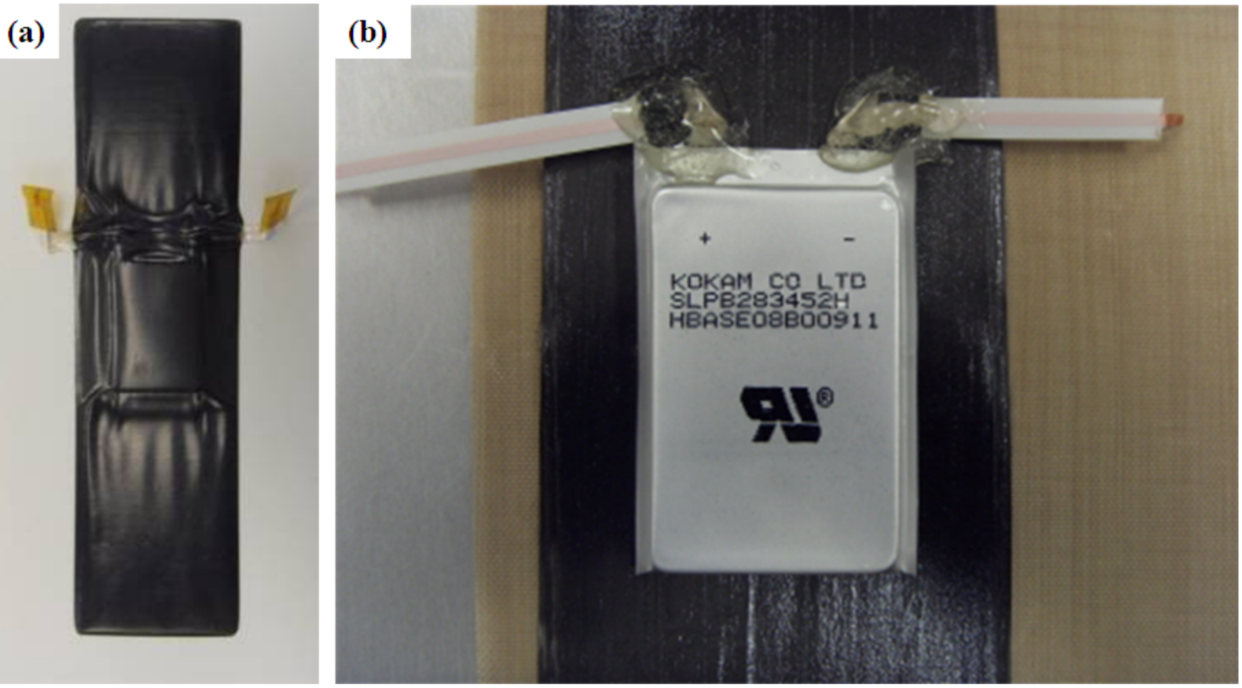

Figure 5.3: (a) CFRP composite laminate with embedded Li-ion polymer battery. (b) The insulated Li-ion polymer battery on CFRP composite laminate.

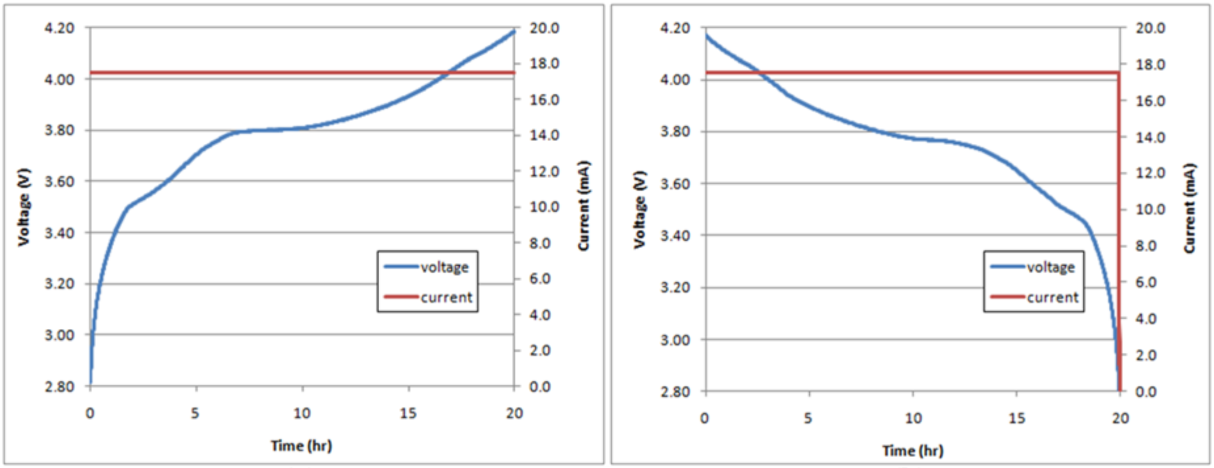

(a) **(b)**

Figure 5.4: (a) Charging and (b) discharging curves of the Li-ion polymer battery at 0.05 C-rate.

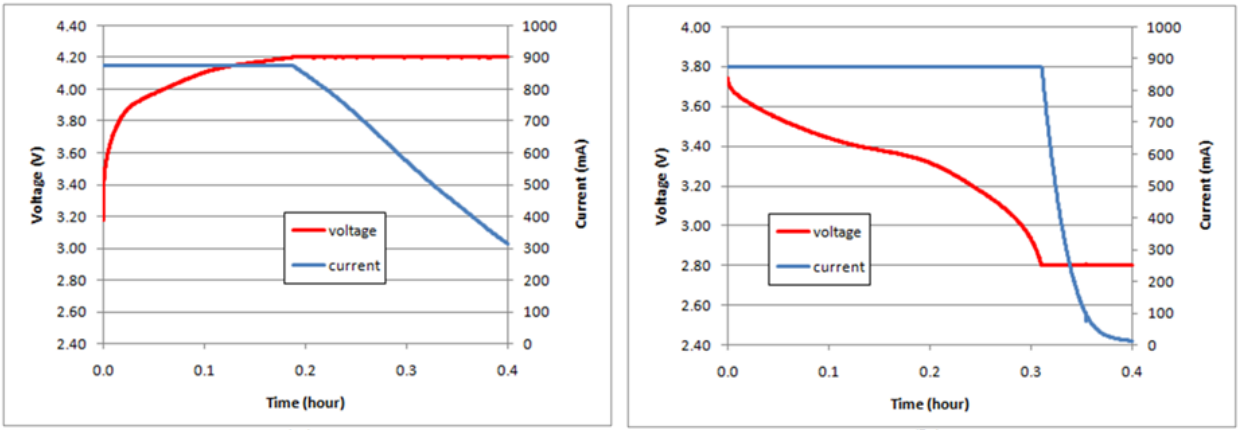

(a) **(b)**

Figure 5.5: (a) Charging and (b) discharging curves of the Li-ion polymer battery at 2.5 C-rate.

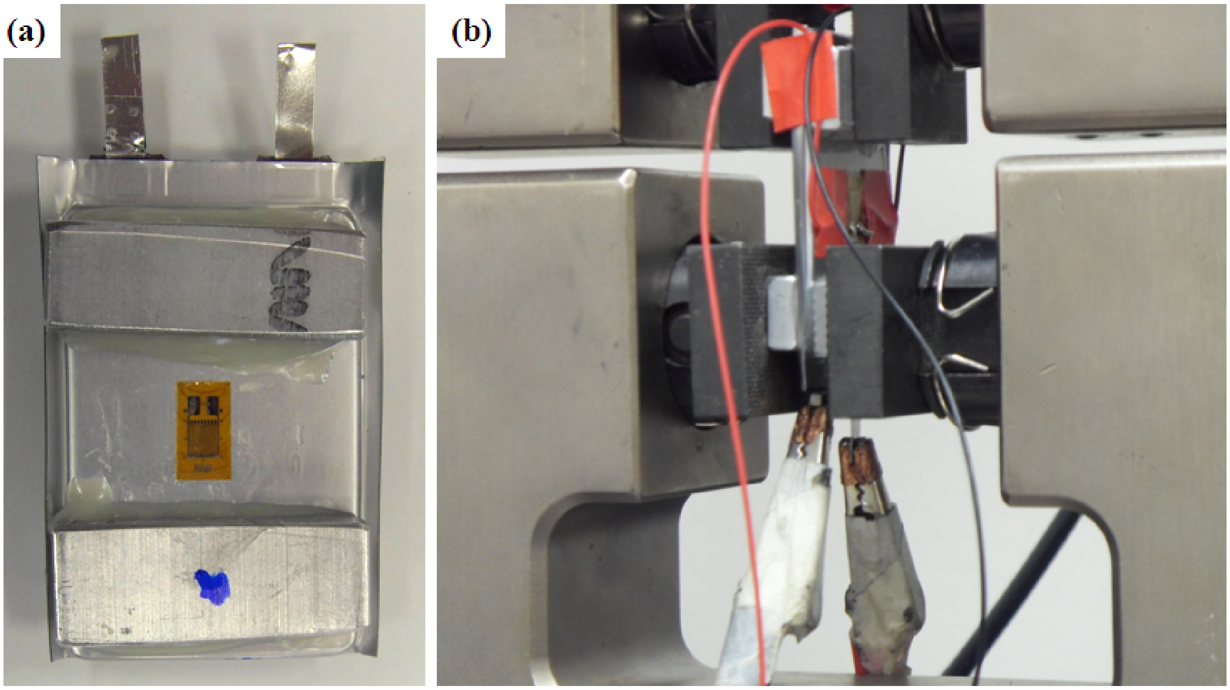

Figure 5.6: The experimental setup for the Li-ion polymer battery under tensile loading.

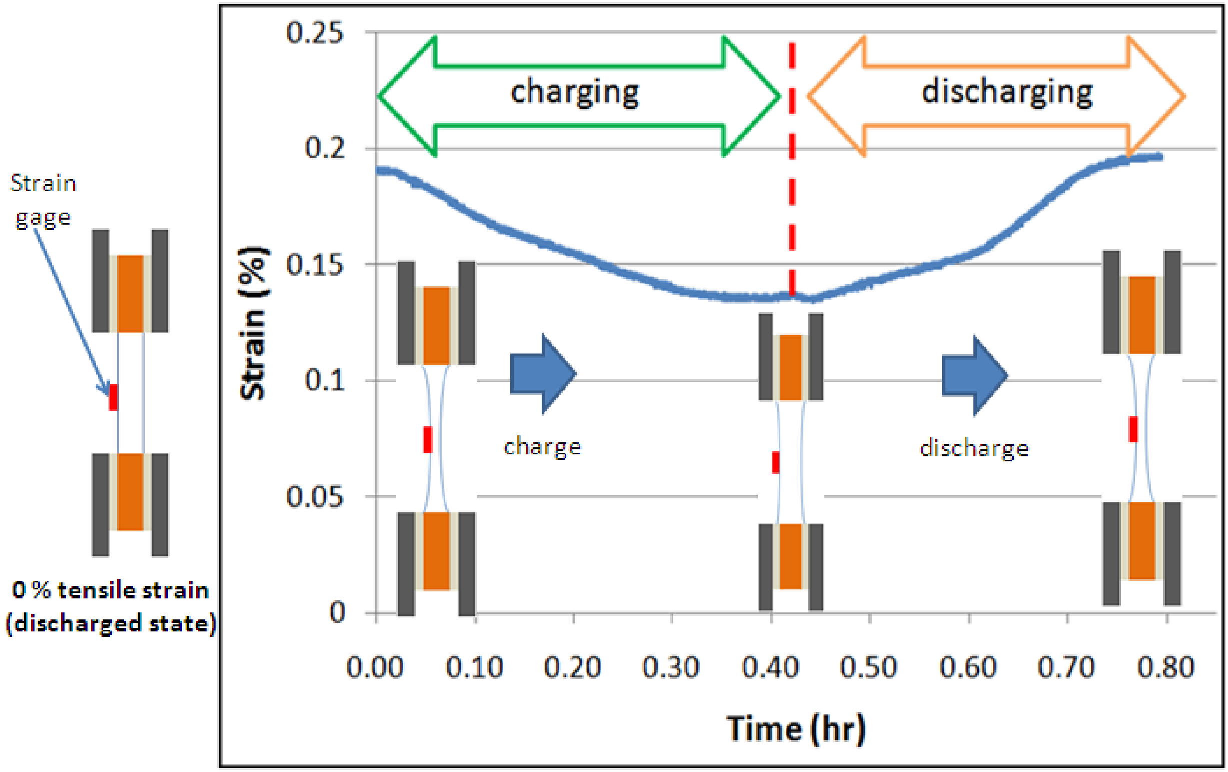

Figure 5.7: Change in tensile strain during charge and discharge.

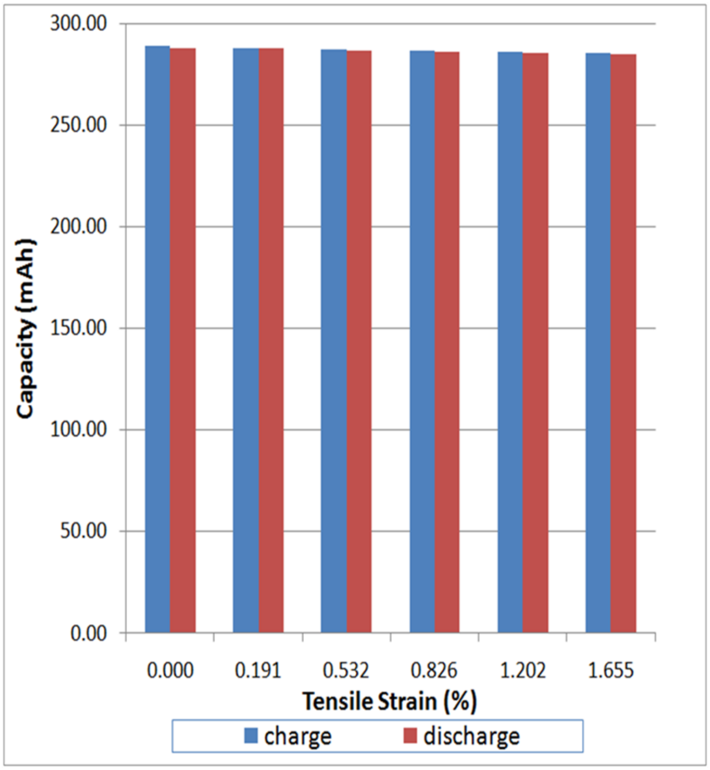

Figure 5.8: The performance of the Li-ion battery under tensile loading.

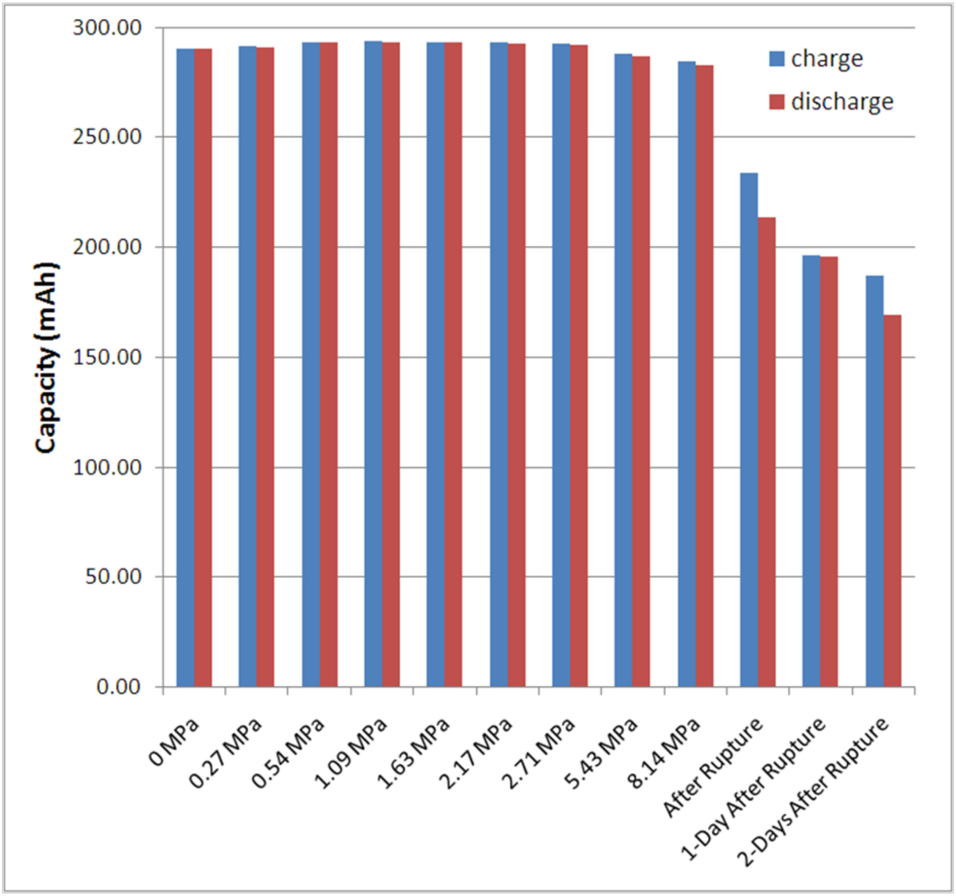

Figure 5.9: The performance of the Li-ion battery under uni-axial pressure.

Figure 5.10: The Li-ion polymer battery after uni-axial pressure test.

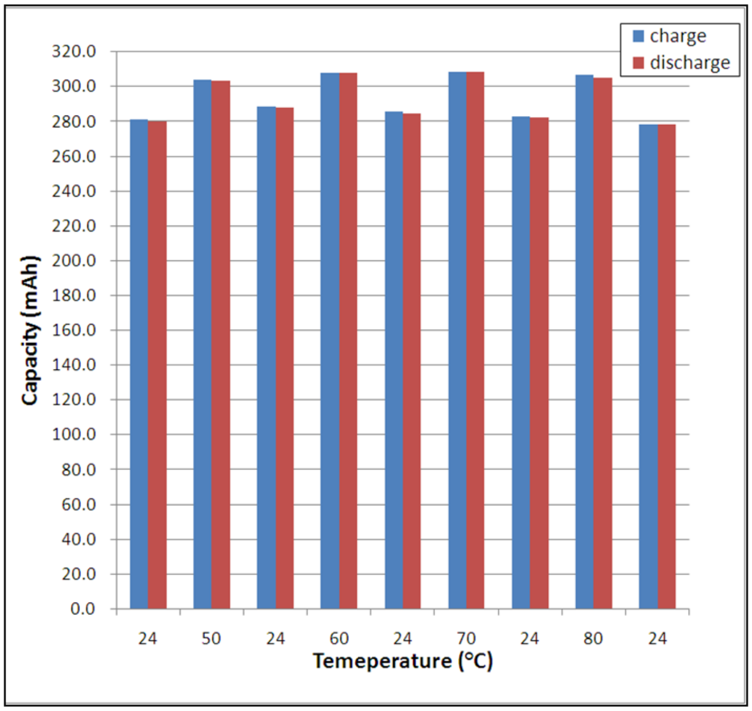

Figure 5.11: The performance of the Li-ion battery at high temperatures of 50, 60, 70 and 80 °C.

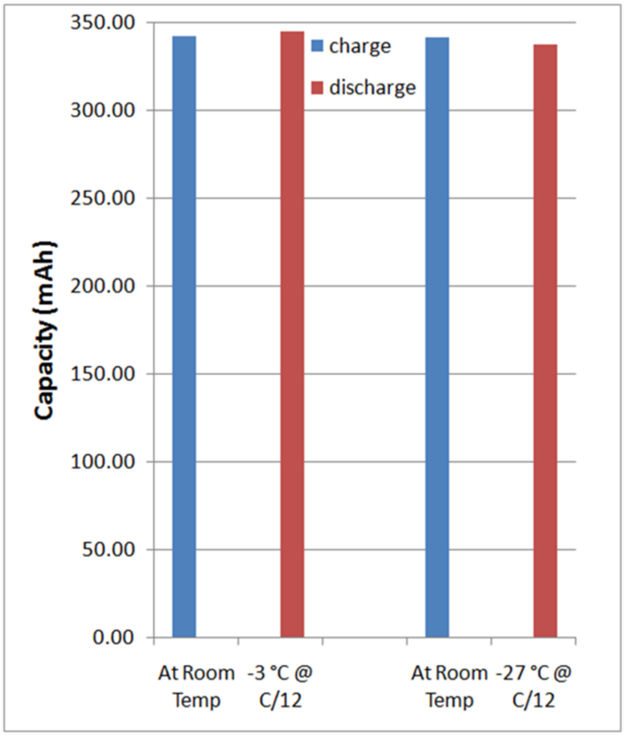

Figure 5.12: The performance of the Li-ion battery at low temperatures of -3 and -27 °C.

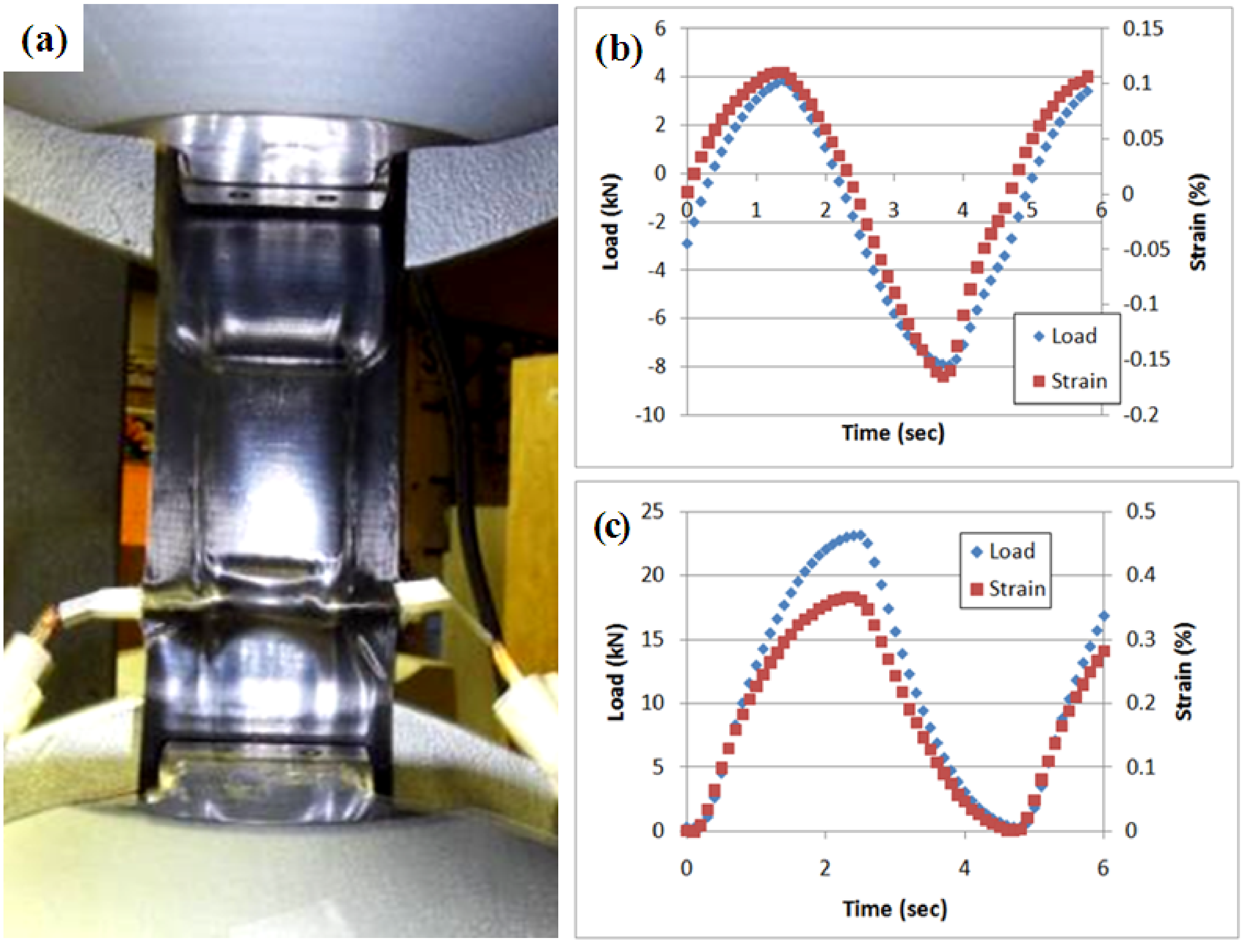

Figure 5.13: (a) The experimental setup for the multi-functional composite laminate under fatigue loading. Loads and strains for (b) tension-compression and (c) tension-tension fatigue testing.

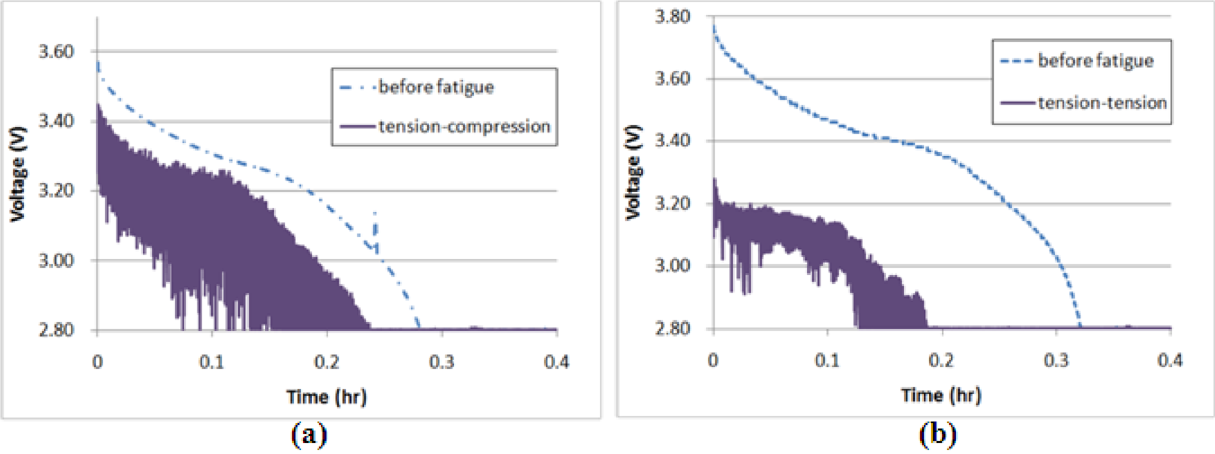

Figure 5.14: Discharging of the Li-ion polymer battery under fatigue loading: (a) tension-compression and (b) tension-tension.

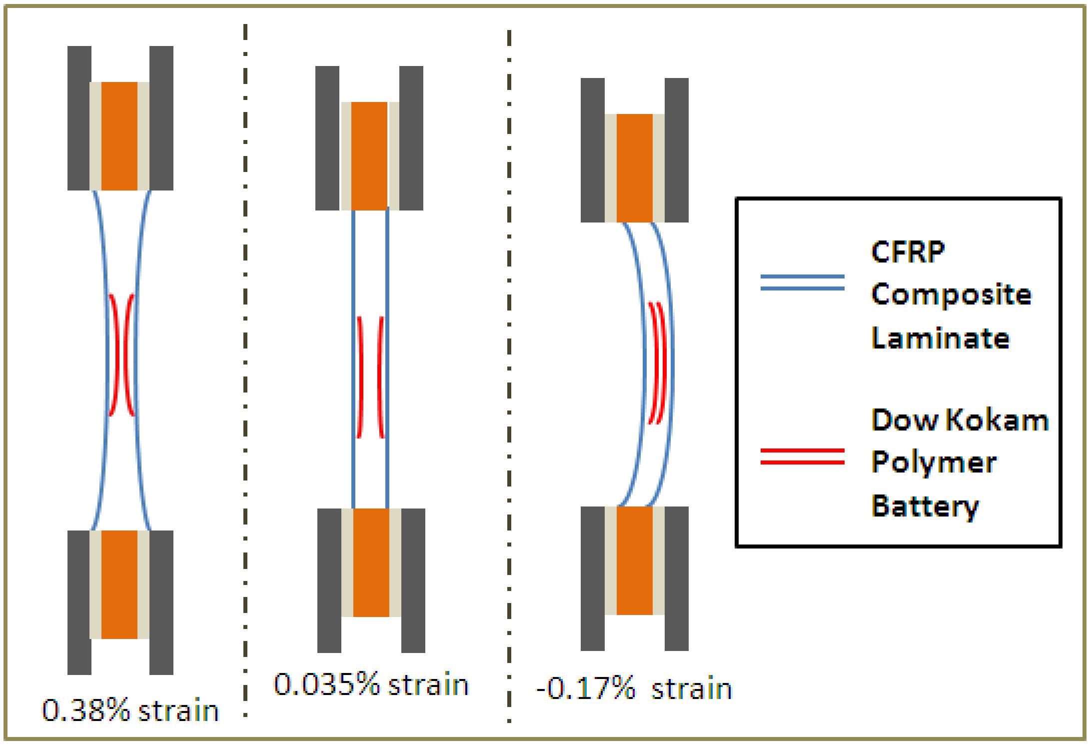

Figure 5.15: Changes in distances between each active layers during fatigue cycles.

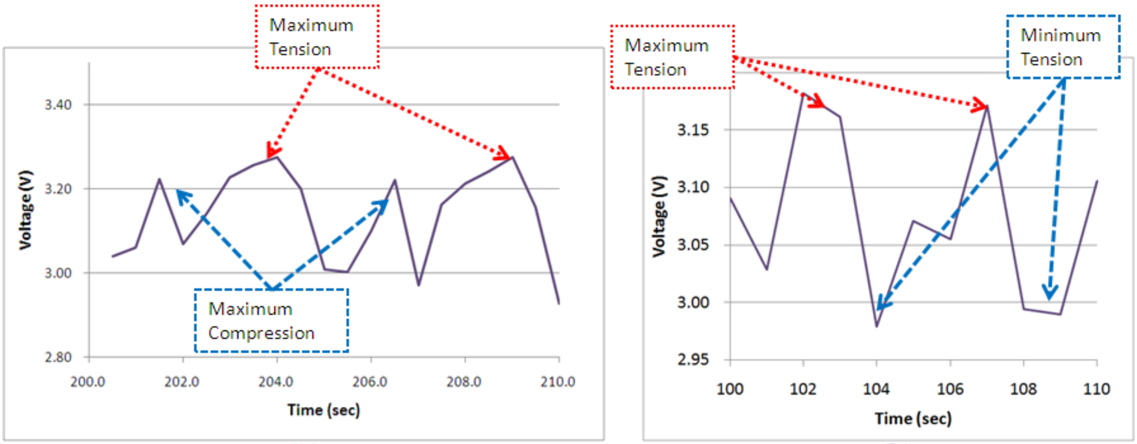

(a) (b)

Figure 5.16: The changes in discharging voltages of Li-ion polymer batteries under fatigue loading: (a) tension-compression and (b) tension-tension.

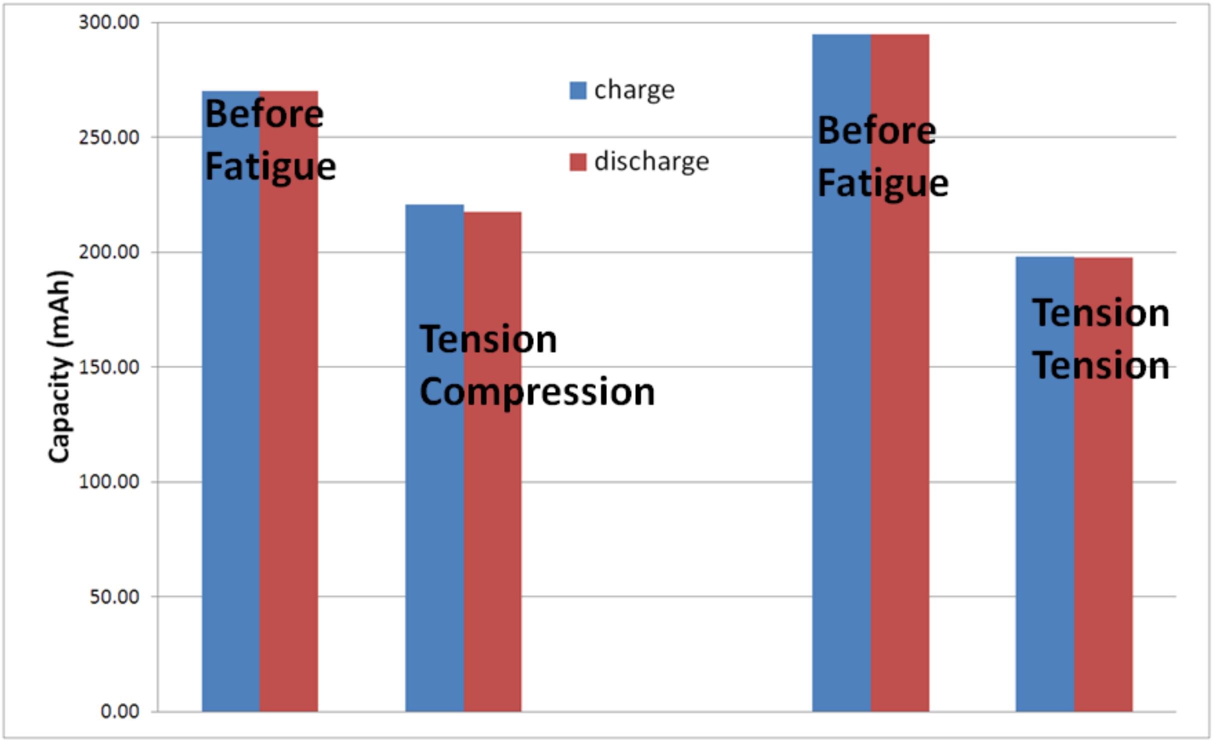

Figure 5.17: The performance of the Li-ion battery under fatigue loadings.

CHAPTER SIX

Sintering of Inkjet Printed Silver Nanoparticles at Room Temperature Using Intense Pulsed Light

6.1. Introduction

In Chapter 2, it was shown that an inkjet printed electrodes can be thermally sintered at 200°C for 30 min. However, this method required long cycle times and a vacuum thermal chamber. To reduce sintering time, Ko et al.[1] demonstrated use of a 520 nm laser to sinter conductive patterns. However, the laser system requires a complicated three-dimensional (3D) gantry system, and can be applied only onto a small area at a time. A promising alternative to laser sintering is a flash lamp annealing, which was developed to sinter thin gate oxides on a large portion of a silicon wafer within milliseconds[2]. This method uses a xenon lamp to apply broad-wavelength light at a high energy density.

In addition, a low-temperature sintering of conductive patterns is necessary to prevent degradation of a polymeric substrate such as the glass-fiber-reinforced polymer composite (GFRPC) substrate[3]. A well-dispersed silver nanoparticles were fabricated using common, generic chemicals by Samsung Electro-Mechanics[4]. The diameter of these silver nanoparticles is less than 50 nm, which is adequate for IPL sintering because they can be sintered at temperatures lower than 200°C[5].

In this research, we have studied the sintering of silver nanoink patterns using IPL technology at various energy densities and pulse numbers without damaging a GFRPC laminate. The silver nanoink patterns were printed onto two different substrates, a GFRPC laminate and polyimide film, using a 3D inkjet printing system. They were chosen as substrates because they are the most popular materials used in printed circuit boards[6]. Thermal analysis for the silver nanoink was performed using differential scanning calorimetry (DSC). The resistivities of sintered patterns were calculated from a resistance measured with a source meter and a thickness measured with a profilometer. The resistivity of IPL sintered patterns was compared with that of thermally sintered patterns. The grain sizes and surface morphologies were characterized using X-ray diffraction (XRD) and scanning electron microscopy (SEM), respectively. Furthermore, absorbance of the silver nanoink was obtained using ultraviolet-visible spectroscopy. Finally, the IPL sintering mechanism for silver nanoink was analyzed using a lumped capacitance thermal analysis.

6.2. Experimental Details

6.2.1. Specimen Specifications

The conductive silver nanoink for this study was prepared by the Imaging Electronics Team in Samsung Electro-Mechanics. Silver nitrate ($AgNO_3$) was used as a silver precursor, n-butylamine was used as a solvent, and sodium borohydride ($NaBH_4$) was used as a reducing agent. For the dispersion medium of the silver nanoink, diethylene glycol (DEG) and water were used. Silver nanoparticles of 20 to 40 nm in diameter were dispersed in solvents at 50 wt%. A drop-on-demand piezoelectric inkjet printer (SemJet, Samsung Electro-Mechanics, Korea) with 128 nozzles was used to print the pattern shown in Fig. 6.1. The droplet size of this printer was 30 pL. The silver nanoink patterns used to calculate resistivity consisted of two square pads with 2.2 mm sides, and a line 0.4 mm wide and 8.8 mm long. The patterns were printed on a 100 μm thick GFRPC laminate; bismaleimide triazine (BT) was used as the polymer matrix. During inkjet printing, the substrate was kept at 85°C to facilitate drying of the solvent in the nanoink.

To look at the surface morphology and study the lattice structure, 5 μL of silver nanoink was dropped using a microdispenser (Research Pro, Eppendorf, Germany), and spread uniformly over a 10 mm by 10 mm square on a polyimide film (Kapton, Dupont, USA). The silver nanoink was heated in an oven (Gravity oven, Lindberg/Blue M, USA) at 85°C for 5 min to dry the solvent. Figure 6.2 depicts the silver pattern before and after it had been dried. The masking tape was removed after the silver pattern had been dried. In addition, 5 μL of silver nanoink was dropped using a microdispenser onto GFRPC laminate to study the effect of thermal sintering on the substrate.

6.2.2. IPL System Setup and Sintering Conditions

The IPL sintering system has the following components: a xenon flash lamp (QXA, PerkinElmer, UK), an aluminum reflector, an ultraviolet (UV) filter, a power supply, four supercapacitors, and a simmer triggering pulse controller. The schematic of this system is shown in Fig. 6.3. The intense pulsed light is produced by arc plasma between the electrodes after the gas is ionized by a voltage bias of 16 kV[7]. When the lamp is triggered using a pulse controller, approximately 1000 A of electrical current is delivered within milliseconds from the supercapacitor (40,000 μF). The optical spectrum of light from our xenon lamp covers a range of wavelengths from 160 nm to 2.5 um[7]. The UV light degrades polymer substrates; therefore, a UV filter was used to eliminate wavelengths under 380 nm[8]. The spectral distribution of the xenon flash lamp from 380 and 1000 nm for 50 J/cm^2 irradiation is shown in Fig. 6.4.

Using the simmer triggering pulse controller, the energy density of the IPL can be set between 20 and 50 J/cm^2 by varying the capacitor charge. The energy density range was measured and verified by the manufacturer of the xenon lamp when the specimen was 14 mm away from the lamp[9]. The number of consecutive pulses can be varied between one and three. For this experiment, IPL energy was applied at 20, 30, 40, and 50 J/cm^2. For a single pulse, the on-time of each pulse was fixed at 4 ms. For the two consecutive pulses, on-times were fixed at 4 ms and 6 ms, consecutively, and for the three consecutive pulse types, on-times were fixed at 4, 6, and 6 ms, consecutively. The time gap between pulses was kept at 5 ms. As the on-time decreased, the power of the IPL light increased. For instance, at 50 J/cm^2, the single-pulse mode irradiated at 12,500 W/cm^2 for 4 ms, whereas the three consecutive pulse mode irradiated at 3125 W/cm^2 for 14 ms. The schematics of each pulse type are shown in Fig. 6.5. For comparison, the printed pattern was thermally sintered for 30 min at 200°C inside a furnace (Type 1400 Furnace, Barnstead Thermolyne, USA).

6.2.3. Characterization

The light absorption spectrum of silver nanoink was obtained using ultraviolet-visible spectroscopy (UV-3101 PC, Shimadzu, Japan) from 380 nm to 1000 nm. The specimen was prepared by uniformly coating a soda-lime glass slide with the silver nanoink. The surface morphologies of the IPL sintered silver electrodes were analyzed using SEM (JSM-6700F, JEOL, Japan). The crystal phase was analyzed by XRD (X'Pert Pro, PANalytical, USA). Also, grain sizes of printed patterns were calculated using the Scherrer equation shown below[10]:

$$D = \frac{0.9\lambda}{\delta \cos\theta} \qquad \text{Eq. 6-1}$$

where λ is wavelength, 0.1541 nm, δ is the full-width at half-maximum (FWHM) in radians, and θ is the diffraction angle. In the grain size calculation, 0.010° was subtracted from a full-width at half-maximum due to the instrumental broadening. The melting temperature of the silver nanoink was determined using DSC (Pyris Diamond DSC, Perkin Elmer, USA) in dynamic scanning mode at a rate of 10°C/min from 50 to 400°C.

The four-point probes method, described in Chapter 2, was used to measure the resistance of each pattern using a source meter (Keithley 2400, Keithley, USA) on a probe station (MP-0900, Wentworth Laboratories, USA) with probe needles (SE-T, Signatone, USA). The probe needles were made of tungsten, and the diameter of the tip of the needle was 5.0 μm. The distance between the midpoints of two pairs of current and voltage probe needles was 10.0 mm. (For each pair of needles, the current probe and voltage probe needles were placed 0.30 mm apart.) The thickness and width of each pattern was measured using a profilometer (Tencor P-10 Surface Profilometer, KLA-Tencor, USA). This profilometer has resolution of 10 nm. The electrical resistivity, ρ, was calculated using the Eq. 2-1. The width, thickness, and length of the silver pattern are shown in Fig. 6.1.

6.3. Results and Discussion

To determine a suitable energy density for IPL sintering, energies of 20, 30, 40, and 50 J/cm^2 were tested by irradiating onto inkjet printed silver nanoink pattern using single pulse mode. Figures 6.6b to 6.6e show SEM images of the resulting surfaces. As Figs. 6.6b and 6.6c show, there was not much difference in the particle size for 20 and 30 J/cm^2, compared to the silver pattern before IPL was applied, Fig. 6.6a. As the energy density was increased to 40 J/cm^2, the silver nanoparticles began to agglomerate, but the sizes of agglomerated particles were not large enough to form a conductive path, Fig. 6.6d. Only when 50 J/cm^2 was applied, the sintered pattern became conductive; the particles agglomerated to create a conductive path, as shown in Fig. 6.6e. However, the resistivity of the conductive pattern sintered at 50 J/cm^2 was too high, 186 ± 25 nΩ·m. The high resistance of the sintered silver nanoink pattern produced by single pulse IPL irradiation might be the result of incomplete sintering of the silver nanoink pattern through the thickness.

Although the power intensity decreased, the sintering quality of the silver nanoink pattern improved as the number of consecutive pulses was varied from one to two to three consecutive pulses, keeping the total energy density constant at 50 J/cm^2. The silver nanoparticles were agglomerated further as two and three consecutive pulses were applied, as shown in Figs. 6.7a and 6.7b, respectively. The average resistivity of the sintered conductive pattern using two consecutive pulses at 50 J/cm^2 was 80 ± 10 nΩ·m, which is about five times higher than that of bulk silver, 15.87 nΩ·m, and two times higher than that of the thermally sintered silver pattern, 39 ± 2 nΩm, shown in Fig. 6.7c. The average resistivity of the IPL sintered pattern with three consecutive pulses was 49 ± 3 nΩ·m, which is almost the same as in previous work by Kim et al.[9] on printed copper pattern, 50 nΩ·m. The thermally sintered pattern had better resistivity because the grain boundaries of silver nanoparticles grew and the pattern became denser. The average thickness of the sintered patterns was 9.83 ± 2.00 μm). Representative values of resistances, widths, lengths, thicknesses and resistivities of sintered patterns are presented in Table 6.1, and resistivities are summarized in Fig. 6.8. Based on these results, it was concluded that the silver nanoink patterns on polyimide films were fully sintered with three consecutive pulses at 50 J/cm^2; applying high energy for longer period of time was more effective in sintering silver nanoink.

Moreover, XRD was used to show increasing grain size, as in Fig. 6.9. Three samples were used for the comparison: before IPL sintering, after IPL sintering with three consecutive pulses at 50 J/cm^2 and thermally sintered samples. Before IPL was applied, XRD showed broad and low-intensity peaks, which means that the silver nanoink pattern is in an amorphous phase. However, after IPL was applied, XRD showed very sharp and high-intensity peaks. These sharp peaks show that the silver nanoink pattern was sintered completely, becoming a crystalline solid[11]. Figure 6.9 shows five characteristic peaks at 38.3°¸ 44.5°, 64.6°, 77.7°, and 81.6° for the planar reflections of (111), (200), (220), (310), and (222), respectively. These characteristic peaks confirmed that face-centered cubic silver had been obtained using IPL [12] Using Eq. 6-1, the grain size of the printed silver nanoparticles was calculated to be 28.0 ± 8.1 nm, which is within the range of silver nanoparticle size, 20 to 40 nm in diameter. After the three consecutive IPL pulses, the grain size increased to 86.3 ± 7.2 nm. This increase in grain size shows that the silver nanoparticles were melted during the application of IPL, and they were solidified after the application of IPL. Also, the thermally sintered pattern had a larger grain size of 102.8 ± 5.2 nm, as expected from the SEM images. FWHM and diffraction angles for these calculations are presented in Table 6.2.

Adhesion between the electrode pattern and the substrate is important in printed electronics. Therefore, peel testing using adhesive tape (Tape 810, 3M, US) was performed on the silver patterns. The adhesive tape was firmly pressed onto the IPL sintered conductive patterns, and was slowly peeled off from the patterns by hand at 150° to 160°. The silver patterns that were applied with IPL for single and two consecutive pulses were easily peeled off with the adhesive tape, as shown in Figs. 6.10a and 6.10b, respectively. However, the silver pattern on which the three consecutive IPL pulses were applied was not peeled off, shown in Fig. 6.10c. Therefore, it was concluded that the IPL sintered electrode pattern with three consecutive pulses had a reliable bond to the substrate.

The sintering mechanism can be analyzed using a lumped capacitance model. The Biot number for IPL sintering of silver nanoparticles can be calculated from the following equation:

$$Bi = \frac{hr}{3k} \qquad \text{Eq. 6-3}$$

where h is the convective heat transfer coefficient of air, 15 $\mathrm{W/m^2 \cdot K}$, r is the radius of the silver nanoparticle, 30 nm, and k is the thermal conductivity of silver, 429 $\mathrm{W/m \cdot K}$. As the Biot number is much less than 0.1, the temperature increase in the silver nanoink pattern during the application of IPL can be estimated using a lumped capacitance method as follows:

$$\Delta T = \frac{E}{d_{\mathrm{m}} C_{\mathrm{p}} A t} = \frac{\varepsilon_{\mathrm{total}}}{d_{\mathrm{m}} C_{\mathrm{p}} t} \qquad \text{Eq. 6-4}$$

where $\varepsilon_{\text{total}}$ is the total net absorbed energy density, d_m is the density of the nanoink, C_p is the heat capacity of the nanoink, and t is the conductive pattern thickness. To calculate the absorbed energy density, the applied energy density of IPL, 50 J/cm^2, was broken down to specific energy densities at different wavelengths, according to the graph shown in Fig. 6.4. Since the absorption of silver is dependent on wavelength, ultraviolet-visible spectroscopy was used to determine the absorbance of light at different wavelengths. In addition to the absorbance, the reflectance of the silver nanoparticles is also an important factor to calculate the net absorbed energy. The absorption peak of silver nanoink around 558 ± 4 nm is shown in Fig. 6.11. From 558 to 1000 nm, the absorbance decreased to 0.611 from 0.962. Also, Fig. 6.11 shows that the reflectance increased from 0.80 to 0.95 as the wavelength increased from 380 to 1000 nm [13] Based on the absorbance and reflectance, the absorbed energy density at each wavelength, E_λ, was calculated using the following equation[14]:

$$E_\lambda = (1 - R_\lambda) I_\lambda \alpha_\lambda$$

Eq. 6-5

where R_λ is the reflectance, I_λ is the energy density, and α_λ is the absorbance of the silver pattern at different wavelengths, λ.

The light energy density of wavelengths greater than 1000 nm is very small compared with that of wavelengths less than 1000 nm. Therefore, the absorbed energy densities at different wavelengths were summed over 380 to 1000 nm to obtain the total absorbed energy density, $\varepsilon_{\text{total}}$, by applying IPL at 50 J/cm^2 using the following equation:

$$\varepsilon_{\text{total}} = \sum_{\lambda=380}^{1000} E_\lambda$$

Eq. 6-6

From the calculation above, the total energy absorbed by the silver nanoparticle layer was calculated to be 2.267 J/cm^2. In the calculation, all of the gradients in the dried silver nanoink such as 30% diethylene glycol (DEG) and 70% silver nanoparticles by weight were considered. Material properties used for this calculation are presented in Table 6.3. The heat capacity of the silver nanoink layer was calculated to be 0.591 J/gK using the mixture rule[15]:

Eq.6-7

$$C_{\text{p}} = w_{\text{D}} C_{\text{D}} + w_{\text{Ag}} C_{\text{Ag}}$$

where C is the heat capacity and w is the weight percent. The subscripts D and Ag denote DEG and silver nanoink, respectively.

Based on the calculated total absorbed energy and total heat capacity, the increase in temperature of the silver nanoink pattern at 10 μm thickness was calculated to be 500°C during the irradiation by IPL. This temperature increase was high enough to cause coalescence and sintering of silver nanoparticles because as the size of a metallic particle decreases the melting temperature decreases. As shown in Eq.2-2, the melting temperature can be decreased dramatically by decreasing the size of the particles in the nano range. Through the differential scanning calorimetry (DSC) shown in Fig. 6.12, the melting temperature of the silver nanoink was found to be 194.1 ± 4.5°C which is defined as the onset temperature of the endothermic peak[16]. This temperature is much lower than the temperature of printed pattern reached by IPL irradiation, 525°C, obtained by summing the room temperature of 25°C and the increase in temperature (500°C) by IPL irradiation at 50 J/cm^2, calculated using Eq. 6-6. In addition, according to Mackenzie and Shuttleworth,[17] the sintering temperature of a metal particle is about 20% lower than its melting temperature at which the small particles agglomerate together due to surface diffusion. Also, the average latent heat of fusion of the silver nanoparticles was obtained as 12.8 ± 2.1 kJ/kg from three samples of silver nanoink. According to Zhao et al., [18] the latent heat of fusion of silver nanoparticles can be as low as 10.29 kJ/kg, which is one-ninth of the latent heat of fusion of the bulk silver, 88.0 kJ/kg. Therefore, silver nanoparticles were adequately sintered by IPL irradiation to make a low-resistance conductive path, showing clearly adhered junctions among the particles and grainy structure. (Figure 6.7b)

Moreover, according to Hong and Yeh [19] bismaleimide triazine resins are thermally degraded by heating above 190°C. This temperature is lower than the melting temperature of our silver nanoparticles. As expected, when the silver pattern on the GFRPC laminate was sintered at 200°C for 30 min, thermal degradation of GFRPC laminate was observed based on the color of the GFRPC laminate, Fig. 6.13b. Compared with the original GFRPC laminate, Fig. 6.13a, the GFRPC laminate with the silver nanoink pattern that was sintered at 200°C was blackened due to thermal degradation. However, as Fig. 6.13c shows, the GFRPC laminate with the silver nanoink pattern that was sintered by IPL at room temperature was degraded less than that of the thermal sintered case, which is one of the strengths of IPL sintering. According to Kim et al., [9] the GFRPC substrate was saved because it has much higher thermal capacity and mass than that of the metal particle layer, and the IPL irradiation duration is less than 30 ms. Therefore, it could be concluded that the IPL sintering technique can protect the substrate better than the conventional thermal sintering process.

6.4. Conclusions

A silver conductive pattern made by inkjet printing was sintered at room temperature using IPL. Using lumped capacitance method, it was found that IPL irradiation of 50 J/cm^2 increases the temperature of the printed silver nanoink pattern by 500°C. To fully sinter the conductive silver pattern with reliable bonding strength, energy density of 50 J/cm^2 should be used for three consecutive pulses with a 5 ms interval between each pulse. The average resistivity of the fully sintered silver pattern was 49 ± 3 nΩ·m, which is the adequate resistivity value to be used as a conductive circuit[20]. The grain size of the IPL sintered silver nanoparticles was 86.3 ± 7.2 nm; this value is three times higher than that of unsintered silver nanoparticles. Moreover, IPL sintering is more appropriate for protecting the substrate rather than a thermal sintering process. It is expected that the IPL sintering technique can be used in a variety of printed electronics applications.

6.5. References

[1] S.H. Ko, H. Pan, C.P. Grigoropoulos, C.K. Luscombe, J.M.J. Frechet, and D. Poulikakos, "Air stable high resolution organic transistors by selective laser sintering of ink-jet printed metal nanoparticles," Applied Physics Letters, 2007.

[2] S. Kamiyama, T. Miura, and Y. Nara, "Ultrathin HfO[sub 2] Films Treated by Xenon Flash Lamp Annealing for Use as Transistor Gate Dielectric Replacements," Electrochemical and Solid-State Letters, vol. 8, Dec. 2005, pp. G367-G370.

[3] P. Lv, Z. Wang, K. Hu, and W. Fan, "Flammability and thermal degradation of flame retarded polypropylene composites containing melamine phosphate and pentaerythritol derivatives," Polymer degradation and stability, vol. 90, 2005, pp. 523–534.

[4] K.J. Lee, B.H. Jun, T.H. Kim, and J. Joung, "Direct synthesis and inkjetting of silver nanocrystals toward printed electronics," Nanotechnology, vol. 17, 2006, pp. 2424-2428.

[5] P. Buffat and J. Borel, “Size effect on the melting temperature of gold particles,” Physical Review A, vol. 13, Jun. 1976, pp. 2287-2298.

[6] M.K. Ghosh and K.L. Mittal, Polyimides: fundamentals and applications, CRC, 1996.

[7] PerkinElmer Optoelectronics 2009 High Performance Flash and Arc Lamps (Waltham, MA: Perkinelmer)

[8] D.J.T. Hill, F.A. Rasoul, J.S. Forsythe, J.H. O'Donnell, P.J. Pomery, G.A. George, P.R. Young, and J.W. Connell, “Effect of simulated low earth orbit radiation on polyimides (UV degradation study),” Journal of Applied Polymer Science, vol. 58, 1995, pp. 1847-1856.

[9] H. Kim, S.R. Dhage, D. Shim, and H.T. Hahn, “Intense pulsed light sintering of copper nanoink for printed electronics,” Applied Physics A, vol. 97, 2009, pp. 791-798.

[10] H.G. Jiang, M. Rühle, and E.J. Lavernia, “On the Applicability of the X-Ray Diffraction Line Profile Analysis in Extracting Grain Size and Microstrain in Nanocrystalline Materials,” Journal of Materials Research, vol. 14, 1999, pp. 549-559.

[11] B.E. Warren, X-ray Diffraction, Dover Pubns, 1990.

[12] E.A. Owen and G.I. Williams, “A low-temperature X-ray camera,” Journal of Scientific Instruments, vol. 31, 1954, pp. 49-54.

[13] M. Bass, Handbook of optics, McGraw-Hill, 2001.

[14] M.A. Al-Nimr and V.S. Arpaci, “Picosecond thermal pulses in thin metal films,” Journal of Applied Physics, vol. 85, 1999, p. 2517.

[15] W. Dimoplon, “Estimating specific-heat of liquid mixtures,” Chem. Eng, vol. 79, 1972, pp. 64–66.

[16] B.B. Sauer, W.G. Kampert, E. Neal Blanchard, S.A. Threefoot, and B.S. Hsiao, “Temperature modulated DSC studies of melting and recrystallization in polymers exhibiting multiple endotherms,” Polymer, vol. 41, 2000, pp. 1099–1108.

[17] J.K. Mackenzie and R. Shuttleworth, “A Phenomenological Theory of Sintering,” Proceedings of the Physical Society. Section B, vol. 62, 1949, pp. 833-852.

[18] S.J. Zhao, S.Q. Wang, D.Y. Cheng, and H.Q. Ye, “Three Distinctive Melting Mechanisms in Isolated Nanoparticles,” J. Phys. Chem. B, vol. 105, Dec. 2011, pp. 12857-12860.

[19] S.G. Hong and C.S. Yeh, “The effects of copper oxides on the thermal degradation of bismaleimide triazine prepreg,” Polymer degradation and stability, vol. 83, 2004, pp. 529–537.

[20] V. Subramanian, P. Chang, D. Huang, J. Lee, S. Molesa, D. Redinger, S. Volkman, VLSI Design held jointly with 5th International Conference on Embedded Systems and Design., 19th International Conference on, 6 (2006)

Table 6.1: Resistivity of printed patterns.

	Resistance (Ω)	Width (μm)	Thickness (μm)	Length (μm)	Resistivity (nΩ·m)
Single pulse at 50 J/cm^2	0.469 ± 0.100	401 ± 20	10.87 ± 2.00	11000	186 ± 25
2 Consecutive pulses at 50 J/cm^2	0.250 ± 0.030	371 ± 20	10.55 ± 2.00	11000	89 ± 10
3 Consecutive pulses at 50 J/cm^2	0.154 ± 0.015	397 ± 20	8.40 ± 2.00	11000	47 ± 3
Thermally sintered at 200 °C	0.122 ± 0.010	368 ± 20	9.69 ± 2.00	11000	40 ± 2

Table 6.2: Grain sizes of printed patterns

	Position (°θ)	FWHM (rad)	Grain size (nm)
Before IPL	19.15 ± 0.02	0.005248 ± 0.002000	28.0 ± 8.1
After IPL	19.14 ± 0.02	0.001700 ± 0.000150	86.3 ± 7.2
Thermally Sintered	19.16 ± 0.02	0.001428 ± 0.000070	102.8 ± 5.2

Table 6.3: Material properties

Material	Density, $\rho\,(\frac{\text{g}}{\text{cm}^3})$	Heat Capacity, $C\,(\frac{\text{J}}{\text{gK}})$
Silver nanoparticle	10.5	0.24
Diethylene glycol	1.12	1.41

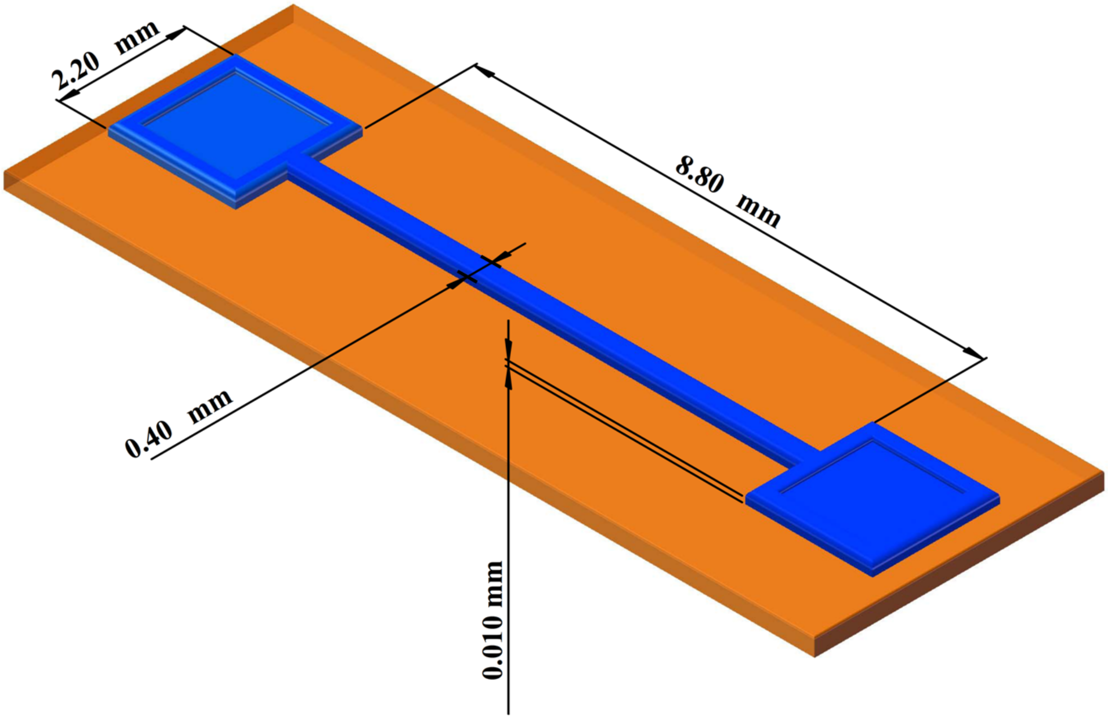

Figure 6.1: The geometry profile of the silver conductive pattern.

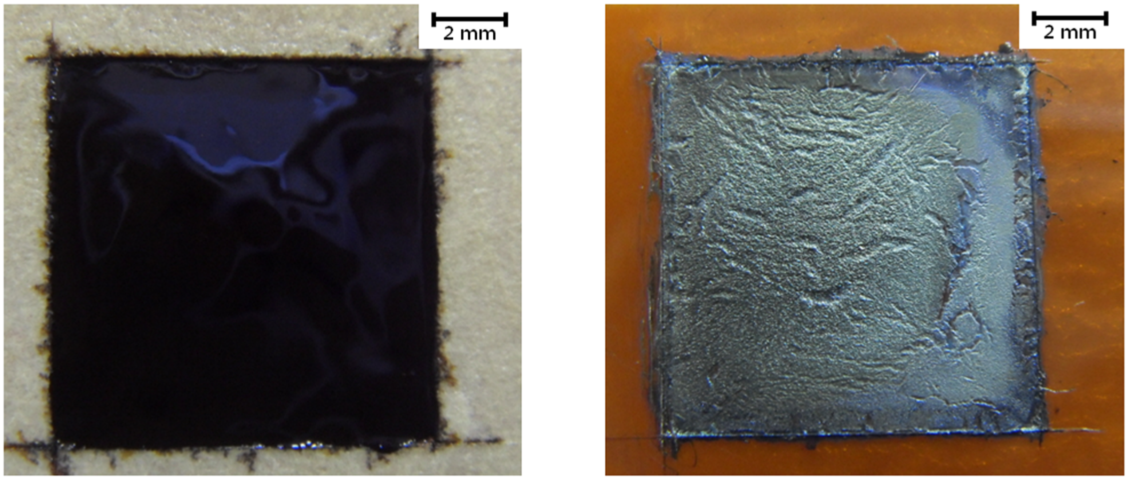

(a) (b)

Figure 6.2: The silver nanoink pattern used for sheet resistance measurement: (a) before and (b) after dried at 85 °C.

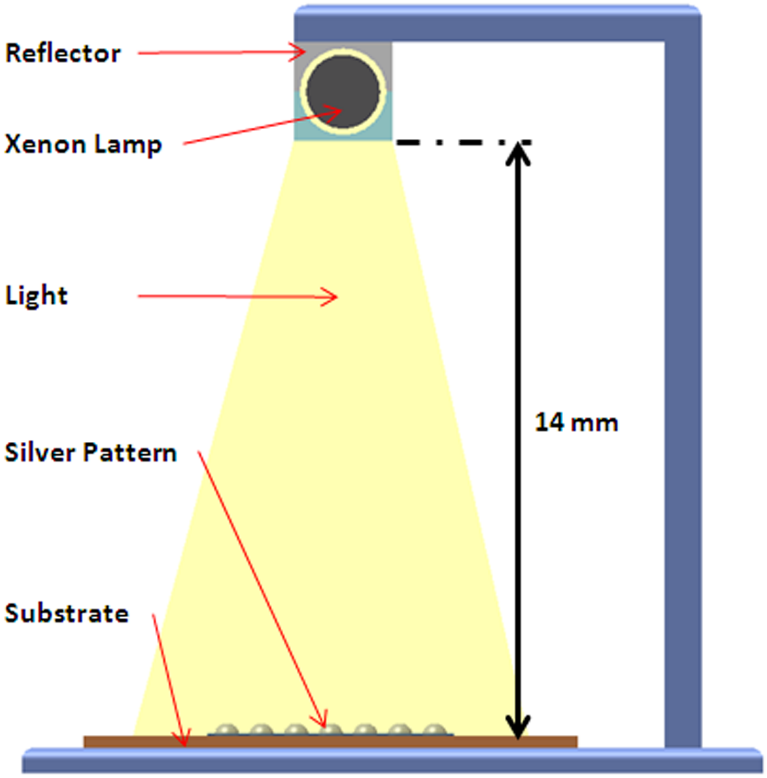

Figure 6.3: Schematic diagram of IPL system.

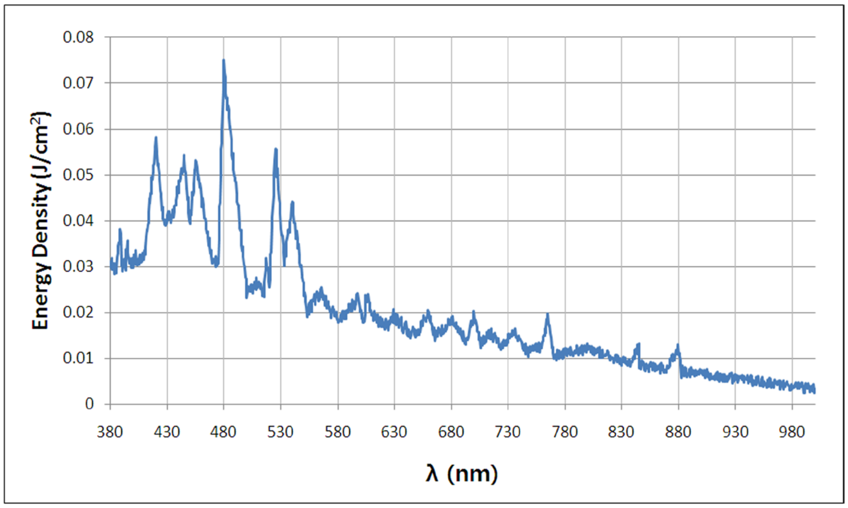

Figure 6.4: The spectral distribution of a xenon flash lamp between 380 nm and 1000 nm for 50 J/cm^2.

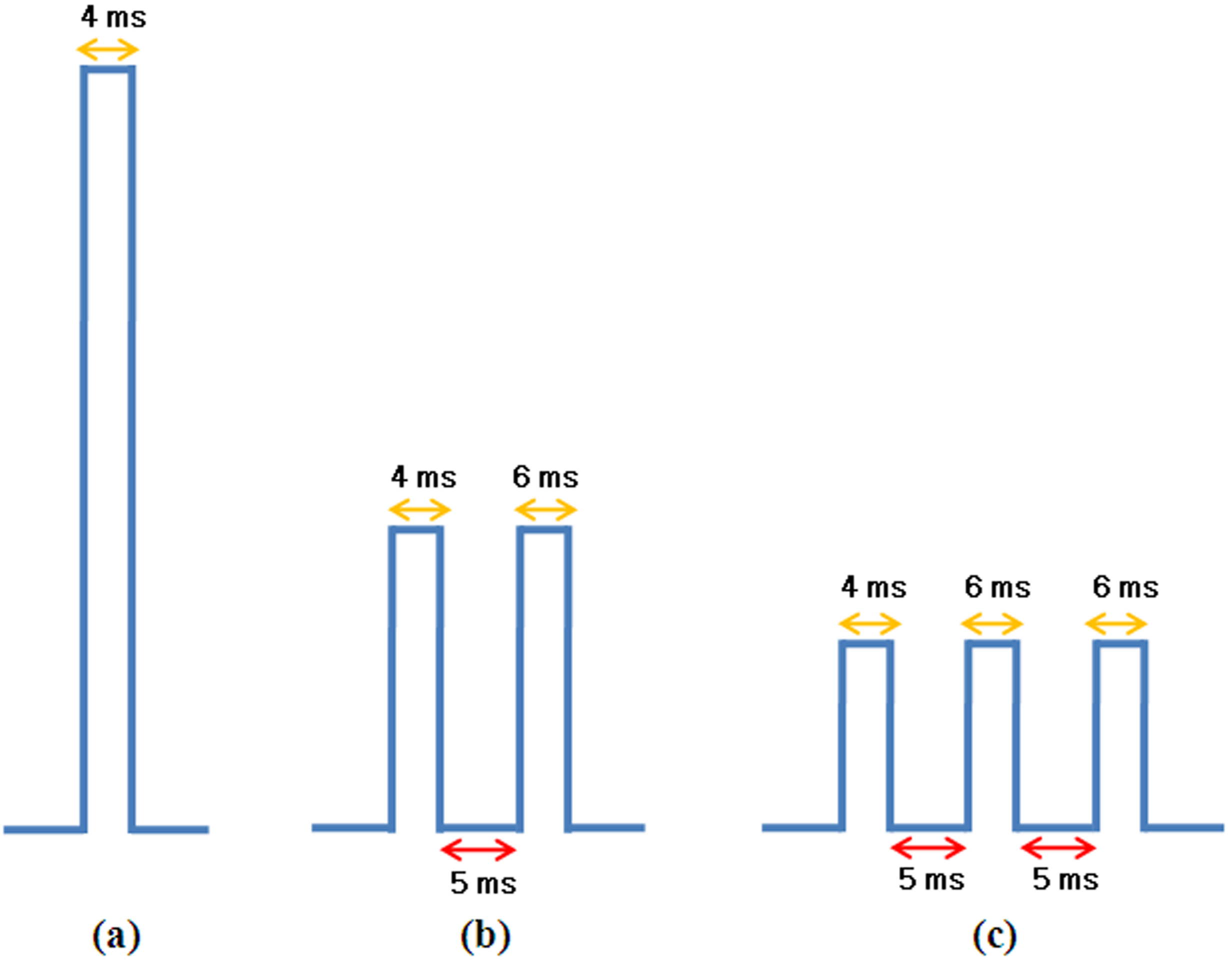

Figure 6.5: Schematic of consecutive IPL pulse types: (a) single, (b) two, and (c) three consecutive pulse modes.

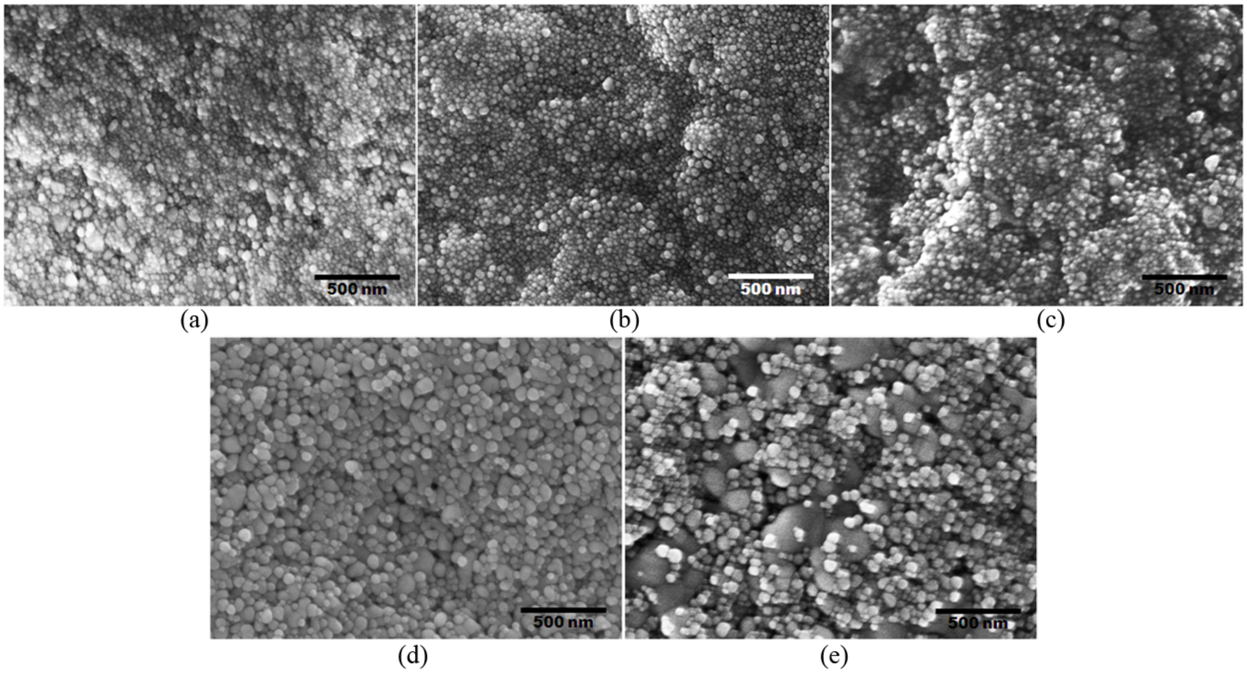

Figure 6.6: SEM images of the surfaces of the silver nanoink patterns: (a) before IPL was applied, and after IPL was applied with one pulse at (b) 20 J/cm^2, (c) 30 J/cm^2, (d) 40 J/cm^2, and (e) 50 J/cm^2.

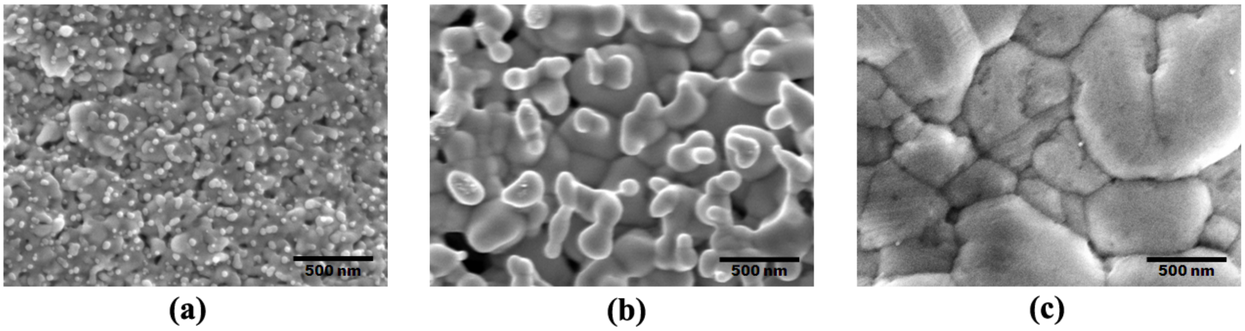

Figure 6.7: SEM images of the surfaces of the silver nanoink patterns: (a) two consecutive pulses and (b) three consecutive pulses at 50 J/cm^2, and (c) thermally sintered at 200 °C.

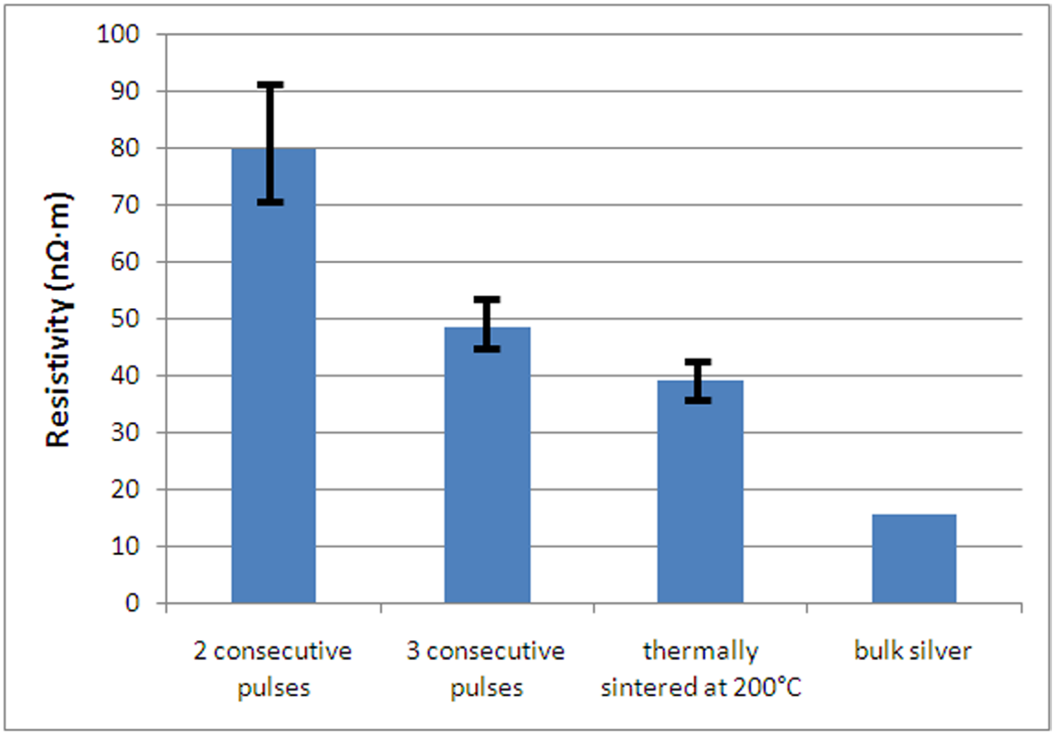

Figure 6.8: Resistivity of sintered patterns.

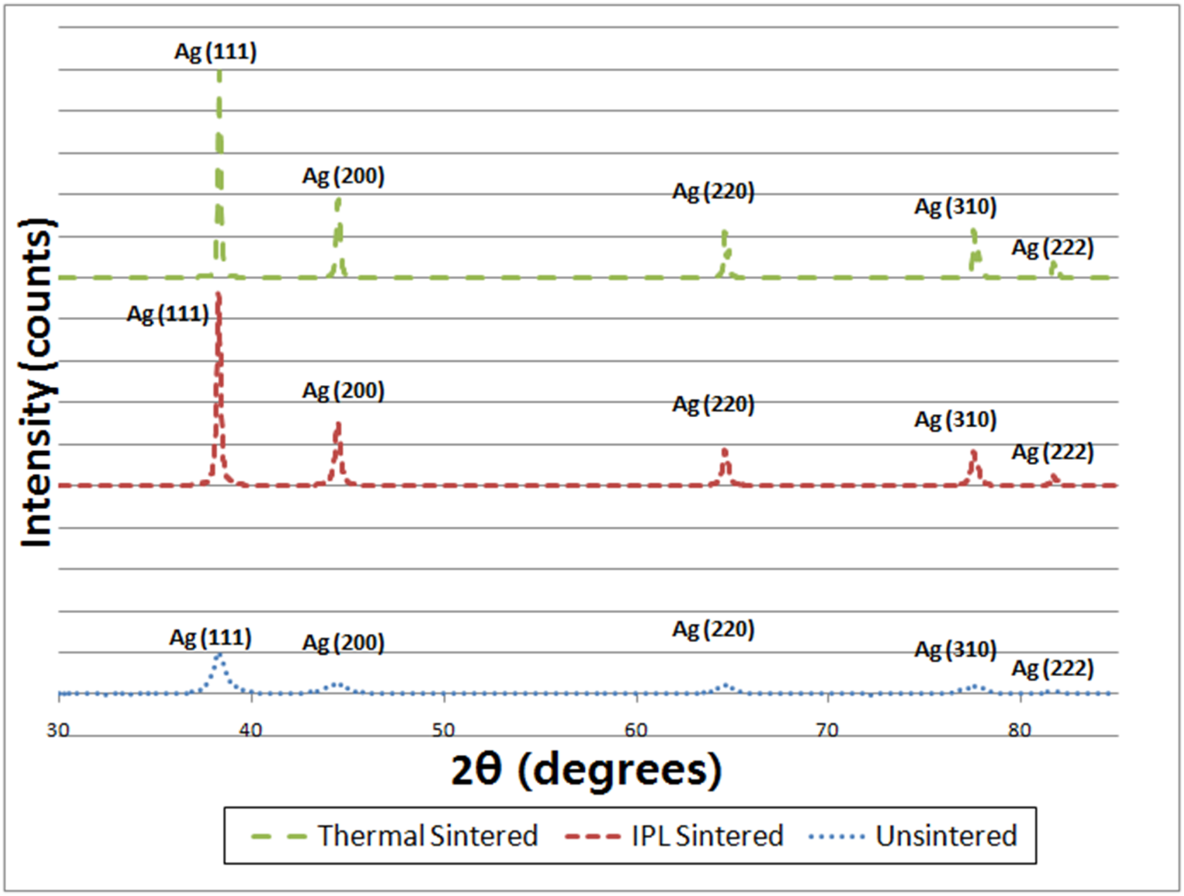

Figure 6.9: XRD of the silver nanoink pattern.

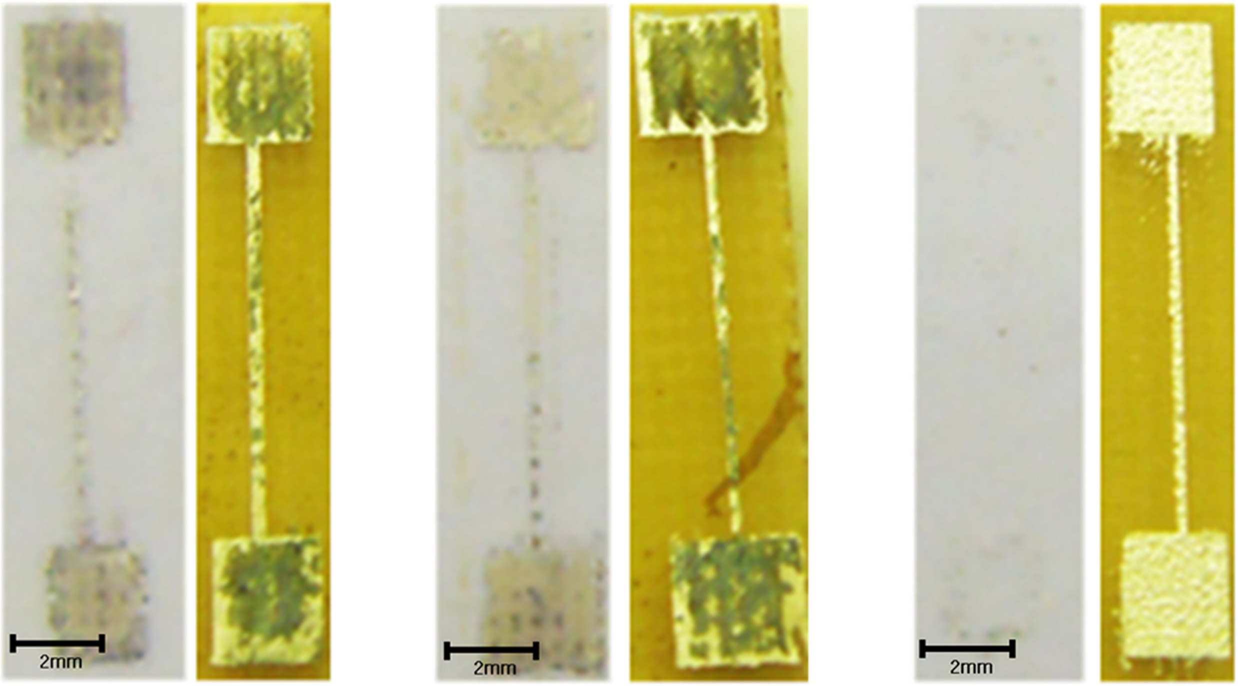

(a) (b) (c)

Figure 6.10: Adhesive tape test of the silver nanoink patterns after following types of IPL were applied: (a) one pulse, (b) two consecutive pulses, and (c) three consecutive pulses. To each pair, left ones are the peeled off scotch tape.

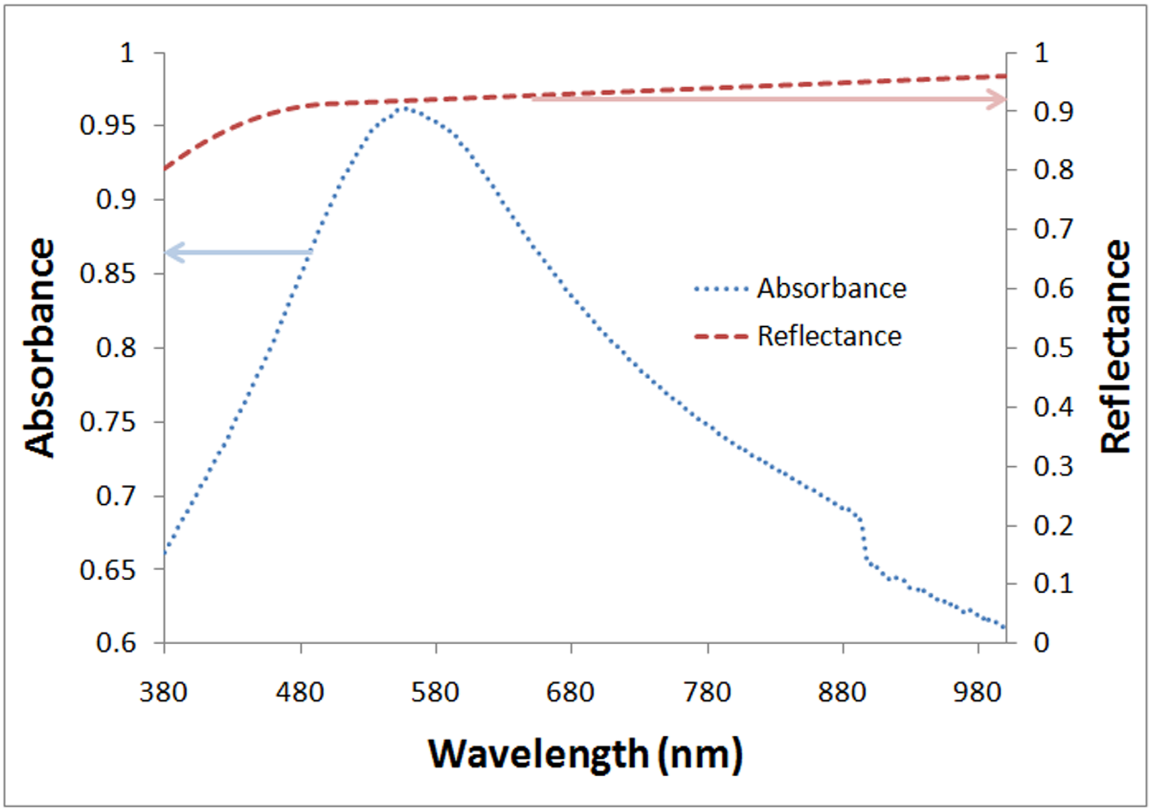

Figure 6.11: Absorbance and reflectance [18] of silver nanoink pattern.

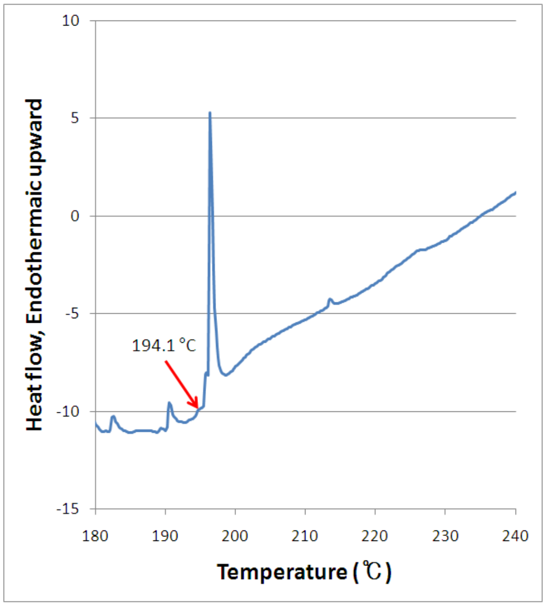

Figure 6.12: The differential scanning calorimetry result of the silver nanoink at 10 °C/min.

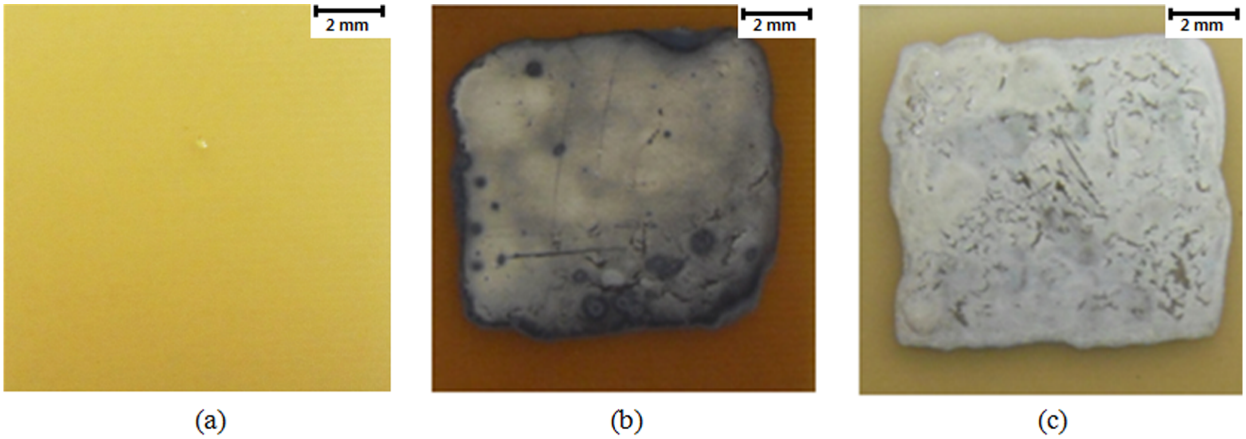

(a) (b) (c)

Figure 6.13: (a) original BT-core, (b) BT-core after thermal sintering at 200 °C and (c) BT-core after IPL sintering.

CHAPTER SEVEN

Concluding Remarks

7.1. Current Research Accomplishments

A multifunctional composite laminate which can harvest and store a solar energy was developed and investigated in this study. The integration of active components onto a carbon fiber reinforced polymer composite laminate was done by using printed electrodes. First, the optimal thickness for making reliable printed electrodes were studied. Then, different kinds of solar cells and batteries were studied under various mechanical and environmental conditions. Lastly, novel sintering process was developed and analyzed to facilitate a manufacturing process and to save a polymeric substrate. The specific findings, results and accomplishments are summarized as follows:

(1) Copper electrodes were printed on composite laminates by inkjet printing and thermal sintering. To reduce the amount of cracks, the range of particle size should be reduced as much as possible because the cracks on surface are mainly caused by having different sizes of particles.

(2) To have good quality of printed electrode, number of printing should not be large because when the thickness of a printed copper electrode become larger than 5.3 µm, cracks of printed electrodes grow. Low resistivity of 36.7 nΩ·m has been reached by printing 5-times.

(3) α-Si solar cells can endure various mechanical loadings including but not limit to the fully reversed flexural fatigue at 0.32% strain at least up to 100 cycles without degradation on their performance.

(4) c-Si solar cells are too brittle to be directly integrated onto a CFRP composite laminate using printed electronics because a tensile failure occurs below 0.2% tensile strain.

(5) The printed electrodes remained fully functional up to the maximum applied strain of 1% when they were 4 μm thick.

(6) A power laminate has been fabricated by first mounting a thin-film solar module and a thin-film battery on a BT core and then co-curing the resulting assembly with a graphite/epoxy composite laminate. A conducting circuit to connect the solar cell and the battery printed on a BT core.

(7) The Li-ion polymer battery was able to achieve 100% depth of discharge at a low temperature of -27 °C under 1/12 C-rate. Under tensile loadings, these batteries were able to endure tensile strain up to 1.7% without a degradation on its performance.

(8) A silver conductive pattern made by an inkjet printing was sintered at a room temperature using IPL in an ambient condition. Using the lumped capacitance method, it was found that IPL irradiation of 50 J/cm^2 in a three consecutive pulse mode increases the temperature of the printed silver nanoink pattern by 500°C.

(9) IPL sintering is more appropriate for protecting the polymeric substrate rather than a conventional thermal sintering process because polymer matrix degrades during thermal sintering. Average resistivity of the fully sintered silver pattern by IPL was 49 ± 3 nΩ·m.

7.2. Recommendations for Further Work

7.2.1. Free Standing Integration

The final goal in this research is to integrate energy harvest/storage components with load bearing structures. However, a battery can show better performance it is disassociated from a mechanical loading. Therefore, a new device packaging concept should be developed, which reduces stress distribution on a battery or solar cell by not attaching it to a composite itself, hence the name “free-standing”. A thin, transparent, flexible polymer film or adhesive is overlaid onto a battery or solar cell and attached to a composite substrate.

7.2.2. Synthesis of Carbon Nanotube using IPL

IPL can be used to apply an intense heat in any environment. There many different methods of making carbon nanotubes (CNTs), but using IPL will reduce a manufacturing time. Proposed methods are as follows: The environment should be an inert environment by flowing Argon at a fixed flow rate of 0.00000167 m^3/s. The source of a carbon is an activated carbon fiber (ACF) because it has very large surface area with many pores and has high adsorptivity. Before irradiating ACF surface with IPL, ACF should go through impregnation process of an iron or nickel, which acts as an catalyst. The impregnation can be done by immersing ACF in an aqueous solution of iron(III)chloride hexahydrate ($FeCl_3 \cdot 6H_2O$), then hydroxylamine hydrochloride ($NH_2OH \cdot HCl$) should be added to reduce iron. The impregnated ACF should be dried in an oven, and IPL can be applied after it is dried. In this process, a carbon nanotube could be produced by CO disproportionation (the Boudouard reaction)[1,2]. The successful growth of a carbon nanotube on ACF will lead to development of a fuel cell electrode material because an ACF with carbon nanotubes should be light, highly conductive, porous, and stable.

7.3. References

[1] Nikolaev, M.J. Bronikowski, R.K. Bradley, F. Rohmund, D.T. Colbert, K.A. Smith, and R.E. Smalley, "Gas-phase catalytic growth of single-walled carbon nanotubes from carbon monoxide," Chemical Physics Letters, vol. 313, 1999, pp. 91–97

[2] C.A. Fyfe, M.S. McKinnon, A. Rudin, and W.J. Tchir, "Investigation of the mechanism of the thermal decomposition of cured phenolic resins by high-resolution carbon-13 CP/MAS solid-state NMR spectroscopy," Macromolecules, vol. 16, 1983, pp. 1216–1219